Characterizing the molecular signatures induced by oncolytic measles virus along with conventional therapies in experimental glioma

Dissertation

zur Erlangung des Grades eines
Doktors der Naturwissenschaften

der Mathematisch-Naturwissenschaftlichen Fakultät
und
der Medizinischen Fakultät
der Eberhard-Karls-Universität Tübingen

vorgelegt
von

Srinath Rajaraman

aus Chennai, India

04 - 2018

Tag der mündlichen Prüfung: 18/12/2018

Dekan der Math.-Nat. Fakultät: Prof. Dr. W. Rosenstiel
Dekan der Medizinischen Fakultät: Prof. Dr. I. B. Autenrieth

1. Berichterstatter: Prof. Dr. Dr. Ghazaleh Tabatabai

2. Berichterstatter: Prof. Dr. Ulrich Lauer

Prüfungskommission: Prof. Dr. Dr. Ghazaleh Tabatabai

                                  Prof. Dr. Ulrich Lauer

                                  Prof. Dr. Ulrike Naumann

                                  PD Dr. Cécile Gouttefangeas

Erklärung / Declaration:

Ich erkläre, dass ich die zur Promotion eingereichte Arbeit mit dem Titel: „*Characterizing the molecular signatures induced by oncolytic measles virus along with conventional therapies in experimental glioma*" selbständig verfasst, nur die angegebenen Quellen und Hilfsmittel benutzt und wörtlich oder inhaltlich übernommene Stellen als solche gekennzeichnet habe. Ich versichere an Eides statt, dass diese Angaben wahr sind und dass ich nichts verschwiegen habe. Mir ist bekannt, dass die falsche Abgabe einer Versicherung an Eides statt mit Freiheitsstrafe bis zu drei Jahren oder mit Geldstrafe bestraft wird.

I hereby, declare that I have produced the work entitled: "Characterizing the molecular signatures induced by oncolytic measles virus along with conventional therapies in experimental glioma" submitted for the award of a doctorate, on my own (without external help), have used only the sources and aids indicated and have marked passages included from other works, whether verbatim or in content, as such. I swear upon oath that these statements are true and that I have not concealed anything. I am aware that making a false declaration under oath is punishable by a term of imprisonment of up to three years or by a fine.

Tübingen, den   27.04.2018

             Datum / Date   Unterschrift /Signature

Acknowledgements

Table of contents

Abbreviations

5-ALA	5-aminolevulinic acid
7-AAD	7-aminoactinomycin D
BATF2	basic leucine zipper transcriptional factor ATF-like 2
CCL5	C-C motif chemokine 5
CCNU	lomustine
CT	alkylating chemotherapy
CXCL10	C-X-C motif chemokine 10
DAMP	danger associated motif pattern
DAPI	4',6-diamidino-2-phenylindole
DDX58	ATP-dependent RNA helicase DDX58 (RIG-1)
DMSO	dimethyl sulfoxide
DsRed	Discosoma sp. red fluorescent protein
EC_{50}	half maximal effective concentration
EGF	epidermal growth factor
EGFR	epidermal growth factor receptor
ELISA	enzyme linked immunosorbent assay
FDA	Food and drug administration
FDR	false discovery rate
FGF	fibroblast growth factor
Flud	fludarabine
GBM	glioblastoma
GCV	ganciclovir
GFP	green fluorescent protein
GM-CSF	granulocyte-macrophage colony stimulating factor
HLA	human leukocyte antigen
HPC	hematopoietic progenitor cell
hpi	hours post infection
hpt	hours post treatment
hSCF	human stem cell factor
HSV-1	herpes simplex virus type 1
hTPO	human thrombopoietin
IFNAR	interferon α-β receptor
IFN-β	interferon beta
IFNγ	interferon gamma
IL3	interleukin-3

IRF1	interferon regulatory factor 1
ISG	interferon stimulated gene
ISGF3	interferon stimulated gene factor 3 complex
IU	infectious units
JAK	Janus kinases
LGG	low grade glioma
MeV	measles virus
MGMT	O^6-methylguanine dna methyltransferase
MHC	major histocompatibility complex
MOI	multiplicity of infection
NIS	sodium iodide symporter
PAMP	pathogen associated motif pattern
PDGFR	platelet derived growth factor receptor
PEI	polyethyleneimine
Pfu	plaque forming units
PLL	poly L-lysine
R-LN229	temozolomide-resistant LN229
RLR	RIG-1 like receptor
RNASeq	RNA sequencing
RT	radiotherapy
SAMD9	sterile alpha motif domain-containing protein 9
SAMD9L	sterile alpha motif domain-containing protein 9-like
SCD	super cytosine deaminase
SEM	standard error of the mean
SOC	standard of care
STAT	signal transducer and transcriptional activator
TAE	tris-acetate edta
TCID$_{50}$	50% tissue culture infectious dose
TGFBI	tumor growth factor beta induced
TK	thymidine kinase
TMZ	temozolomide
TRAIL	tumor necrosis factor- related apoptosis inducing ligand
Treg	regulatory t-cells
T-VEC	talimogene laherparepvec
VEGFR	vascular endothelial growth factor receptor
VT	oncolytic virotherapy

Introduction

1.1 Glioblastoma

Glioblastomas (GBM) are aggressive primary tumors arising from glia or their precursors within the central nervous system with very poor prognosis for affected patients. The median survival period remains to be in the range of 1.5 years even in selected clinical trial populations applying multimodal treatment regimen [1-4]. The genetic landscape of glioblastomas include amplifications and deleterious mutations in key protein signal transduction pathways including epidermal growth factor receptors pathway (EGFR), vascular endothelial growth factor receptor pathway (VEGFR), platelet derived growth factor receptor pathway (PDGFR) along with mutational signatures in key tumor suppressor genes such as *TP53, PTEN, RB1*, etc., affecting cell cycle arrest and promote tumorigenesis [5]. The intra-tumoral heterogeneity within patients with molecularly divergent subclones render it difficult to treat and patients with such multifocal GBMs have worse prognosis with poor overall survival than single focus GBMs [6,7]. The use of 5-aminolevulinic acid (5-ALA) has enhanced surgical removal of deep infiltrating tumor cells which fluoresce due to altered metabolism in cancerous tissue thereby improving progression free survival but complete surgical resection of glioblastoma remains elusive [8]. Surgical intervention for GBM has been mainstay to resect and reduce tumor volumes but is followed-up with other treatment procedures to improve patient outcomes.

1.2 Conventional treatment of glioblastoma

The current standard of care (SOC) for treatment of newly diagnosed glioblastoma involves radiotherapy with concomitant and adjuvant temozolomide [1,9]. The oral alkylating agent, temozolomide (TMZ) functions through methylation of DNA at the O^6 and N^7 positions of guanine and subsequent genotoxicity effected by futile mismatch repair cycles resulting in cytotoxic double strand breaks [10]. Despite the cytotoxic nature and ability of TMZ to cross the blood brain barrier the clinical benefit were mostly limited to patients with methylation of the O^6-methylguanine DNA methyltransferase gene (*MGMT*) [11]. Patients inevitably progress and treated with alternative oral alkylating agent, lomustine [12,13] often in combination with Bevacizumab [14,15]. Recent focus has been on identifying smart combinations of treatments to improve overall survival and progression-free survival of patients. The advent of tumor-treating fields in combination with maintenance TMZ showed significant progression-free survival and overall survival compared to TMZ alone in all patients who completed SOC concomitant radio-chemotherapy [16]. The genetic and morphological complexity of gliomas, intrinsic and acquired resistance to therapy, the inability of therapeutic molecules to intrude infiltrated tumor tissues in the brain parenchyma and an immunosuppressive milieu are just a few reasons that render it difficult to achieve complete recovery with conventional treatments resulting in subsequent

relapse soon after. Novel therapeutic strategies are therefore necessary with the potential to overcome progression, resistance and eventually achieve curative recovery.

1.3 Oncolytic virotherapy

Oncolytic virotherapy provides an exciting approach in this regard with its engineered ability to specifically infect, proliferate and lyse cancerous cells with release of virus particles capable of attacking neighbouring tumor cells thereby sustaining an oncolytic cascade. Genetic engineering approaches have allowed for modification of virulence factors and cloning of transgenes to produce 'armed' viruses with potential to cause tumor cell death, compromise tumor microenvironment or enhance immunogenicity. Early phase-I/II studies involving herpes simplex virus type 1 encoding thymidine kinase used in combination with prodrug ganciclovir (HSV-1 TK/GCV) showed increased overall survival in patients with recurrent glioblastoma [17]. Furthermore, combination of oncolytic HSV-1 TK/GCV with TMZ elicited synergy in U87MG glioblastoma cells *in vitro* and *in vivo* [18]. Similarly, ONYX-015, an E1B-attenuated adenovirus was tested for efficacy in a phase-I dose escalation study for treatment of recurrent malignant glioma [19]. The highest dose of oncolytic ONYX-015 was well tolerated with progression-free survival for 3/12 patients after a 19 month follow up period [19]. Contrary to underlying mechanism of action, increasing evidence of ONYX-015 viral proliferation in presence of p53 and dose-dependent killing of normal human cells warranted further studies and was hence less pursued [20,21]. Recent approval by the Food and Drug Administration (FDA) for use of Talimogene laherparepvec (T-VEC) in treatment of malignant melanoma [22] has revived enthusiasm in preclinical research and therapeutic application of oncolytic viruses. T-VEC is an attenuated, herpes simplex virus type 1 encoding granulocyte-monocyte colony stimulating factor (GM-CSF) designed to initiate an anti-tumor response through selective viral replication in tumor cells and stimulation of systemic anti-tumoral immunity through secretion of GM-CSF.

The existing practice of utilizing Measles virus (MeV) as vaccines provides a distinct edge for its therapeutic approval further supported with clinical evidence of complete remission in one patient treated with oncolytic measles virus in relapsing drug refractory myeloma [23,24]. Ongoing clinical trials employ engineered MeV expressing transgenes with multifarious potential such as MeV encoding human sodium iodide symporter (NIS) for radiovirotherapy by live imaging using radioactive iodine or chemovirotherapeutic approach of MeV expressing Super cytosine deaminase (SCD) by converting prodrugs to toxic metabolites with relative success [25,26].

1.4 Immuno-virotherapy and checkpoint blockade

Glioblastoma are highly immunosuppressive tumors with high levels of regulatory T cell (Tregs) infiltration as well as B7H1 upregulation in tumor associated macrophages thereby restricting

anti-tumoral cytotoxic T cell responses [27,28]. Despite an immunosuppressive milieu, preclinical studies testing efficacy of dendritic cell vaccines loaded with glioma associated antigens elicited a strong CD8$^+$ T cell response with lasting IL12 production leading to progression free survival for 12 months along with complete response in one GBM patient [29]. The oncolytic cascade resulting in lysis of tumor cells releasing virions and cellular debris encompassing highly immune-stimulatory danger and pathogen-associated motif patterns (DAMPs, PAMPs) [30-32] provide cues for induction of antiviral and anti-tumoral immune responses. Efforts are undergoing to combine such immune-virotherapeutic approaches with standard of care (SOC). Wheeler *et al* (2016) successfully combined SOC radiotherapy and temozolomide with an adenoviral vector encoding thymidine kinase functioning in tandem with its prodrug, valacyclovir. This regimen resulted in significant increase in median overall survival compared to SOC alone in patients with malignant glioma [33]. The survival benefit observed with such a combinatorial approach was a 1.5-fold increase over control group after 1 year up to a 5-fold increase observed post 3 years [33]. Further studies have explored provoking host-initiated immune response through combining oncolytic virus with checkpoint blockade to enhance viral stimulated anti-tumoral cytotoxicity with clear evidence of therapeutic synergy in appropriate animal models [31,34]. Combination of T-VEC with anti-PD-1 antibody, pembrolizumab showed increased CD8$^+$ T cells, elevated PD-L1 protein expression and IFN-γ gene expression resulting in a complete response rate of 33% per immune-related response criteria [35]. Similar ongoing trials are underway to assess the combinatorial efficacy of combining immune-stimulatory oncolytic viruses in combination with immune checkpoint blockade inhibitors in melanoma, metastatic head and neck cancer and malignant glioma [35-38].

Scientific Objectives

1. To determine the feasibility of oncolytic virotherapy using MeV in glioblastoma through characterization of glioma cell lines and primary glioblastoma cell cultures *in vitro*.

2. To identify a synergistic combination of MeV with SOC, radiotherapy and alkylating chemotherapy in glioma cell lines (LN229 and LNZ308), glioma stem-like cells (GS8) and temozolomide-resistant LN229 cells (R-LN229) *in vitro*.

3. To characterize and validate the molecular mechanisms of synergy in the combinatorial treatment regimen through transcriptome analysis using RNA sequencing.

4. To delineate the treatment-induced immunological profile of MeV-infected glioma cells established through presentation of antigens using HLA ligandome analysis.

2.1 Materials

Table enlisting all materials used during course of the project

Material	Manufacturer
Antibiotics	
Ampicillin	AppliChem GmbH, Darmstadt, DE
Geneticin (G418)	Thermo Fisher Scientific, Waltham, USA
Gentamycin	Thermo Fisher Scientific, Waltham, USA
Antibodies and dyes for flow cytometry	
7-Amino actinomycin D (7AAD)	eBioscience/Affymetrix, Santa Clara, USA
Anti-Human CD46-PE	eBioscience/Affymetrix, Santa Clara, USA
Anti-Human Nectin-4-APC	R & D systems, Minneapolis, USA
Mouse IgG2B-APC	R & D systems, Minneapolis, USA
Mouse IgGк1-PE	eBioscience/Affymetrix, Santa Clara, USA
Trypan blue	Thermo Fisher Scientific, Waltham, USA
Cell lines	
293-3-46	Kind gift by Prof. Dr. Stephen Russell, (Mayo Clinic) Rochester, USA
GL261, SMA560	Kind gift by Prof. Dr. Wolfgang Wick, (Universitätsklinikum Heidelberg) Heidelberg, DE
GS3, GS8	Kind gift by Prof. Dr. Katrin Lamszus, (Universitätsklinikum Hamburg-Eppendorf) Hamburg, DE
HT-29	Kind gift by Prof. Dr. Ulrich M. Lauer, (Universitätsklinikum Tübingen) Tübingen, DE
LN229, LNZ308, 293T	American Type Culture Collection (ATCC), Manassas, USA
Vero B4	Leibniz Institute DSMZ - German Collection of Microorganisms and Cell Cultures GmbH (DSMZ), Braunschweig, DE

Drugs and small molecule inhibitors	
BX-795	Invivogen, San Diego, USA
Fludarabine	Selleckchem, Houston, USA
Lomustine (CCNU)	Medac, Wedel, DE
Temozolomide (TMZ)	Medac, Wedel, DE
Electrical instruments and machines	
ApoTome, Axio Imager Z1 Microscope	Carl Zeiss AG, Oberkochen, DE
Autoclave V-150	Systec GmbH, Linden, DE
Bacterial incubator	Infors HT, Basel, CH
Centrifuge 5417 R	Eppendorf, Mississauga, CA
Centrifuge Heraeus Fresco 17	Thermo Fisher Scientific, Waltham, USA
Centrifuge Heraeus Multifuge S3R	Thermo Fisher Scientific, Waltham, USA
Centrifuge Heraeus Multifuge X3R	Thermo Fisher Scientific, Waltham, USA
Centrifuge Heraeus Pico	Thermo Fisher Scientific, Waltham, USA
Centrifuge MiniStar silverline	VWR, Darmstadt, DE
ChemiDoc MP gel documentation system	Bio-Rad Laboratories, Hercules, USA
CyAn ADP flow cytometry analyser	Dako, Glostrup, Denmark
Eclipse TS100 microscope	Nikon GmbH, Düsseldorf, DE
Electrophoresis chamber	Neolab, Heidelberg, DE
GammaCell 40 Exactor	Best Theratronics, Ottawa, CA
GloMax Explorer	Promega, Madison, USA
Heraeus HeraSafe clean bench	Thermo Fisher Scientific, Waltham, USA
Hypoxic Chamber Gasboy C40	Labotect Labor-Technik, Göttingen, DE
Kern ABJ balance	Kern, Balingen, DE
Kern EMB 600-2 balance	Kern, Balingen, DE
MACSQuant Analyzer 10	Miltenyi Biotech, Bergisch Gladbach, DE
Microwave	Ok, Ingolstadt, DE
Milli-Q integral water purification system	Merck, Darmstadt, DE
MJ Research PTC-200 Thermal cycler	GMI, Ramsey, USA
NanoDrop ND-1000 Spectrophotometer	Thermo Fisher Scientific, Waltham, USA
PowerEase 90W power supply	Thermo Fisher Scientific, Waltham, USA
Sanyo CO_2 Incubator	Panasonic, Kadoma, JP
Spectrophotometer	Eppendorf, Mississauga, CA
Thermomixer comfort heating block	Eppendorf, Mississauga, CA
Vacuum pump VacuSafe	INTEGRA Biosciences GmbH, Biebertal, DE

Vortex mixer	Heidolph Instruments, Schwabach, DE
Water bath 1083	GFL, Burgwedel, DE

Gel electrophoresis and bacterial work	
1 Kb plus DNA ladder	Thermo Fisher Scientific, Waltham, USA
Gel loading dye purple 6x	New England Biolabs, Ipswich, USA
GelRed nucleic acid gel stain	Biotium, Hayward, USA
Luria Bertani (LB) Agar, Vegitone	Sigma Aldrich, St. Louis, USA
Luria Bertani (LB) Broth, Vegitone	Sigma Aldrich, St. Louis, USA
S.O.C medium	Thermo Fisher Scientific, Waltham, USA
Tris acetate EDTA (TAE) Buffer (50x)	AppliChem GmbH, Darmstadt, DE

Immunoblot antibodies and accessories	
Anti-LC3A rabbit monoclonal antibody (4599s)	Cell Signaling Technology, Danvers, USA
Anti-STAT1 (phospho Y701) mouse monoclonal antibody (ab29045)	Abcam, Cambridge, USA
Anti-STAT1 alpha rabbit antibody (ab92506)	Abcam, Cambridge, USA
Bolt Welcome Pack	Thermo Fisher Scientific, Waltham, USA
Bolt 4-12% Bis-Tris plus gels, 10 well	Thermo Fisher Scientific, Waltham, USA
Human anti-IRF1 rabbit monoclonal antibody (ab186384)	Abcam, Cambridge, USA
Human anti-MGC20410 rabbit monoclonal antibody [BATF2] (ab157466)	Abcam, Cambridge, USA
Human Anti-SAMD9 rabbit monoclonal antibody (ab180575)	Abcam, Cambridge, USA
Human anti-TRAIL rabbit monoclonal antibody (3219s)	Cell Signaling Technology, Danvers, USA
Mouse IgG isotype control (ab37355)	Abcam, Cambridge, USA
Pierce Power blotter	Thermo Fisher Scientific, Waltham, USA
Purified anti-IRF1 mouse antibody (657602)	BioLegend, San Diego, USA
PVDF transfer membrane	Thermo Fisher Scientific, Waltham, USA
Rabbit IgG isotype control (AB-105-C)	R & D systems, Minneapolis, USA
Spectra Broad ranger ladder	Thermo Fisher Scientific, Waltham, USA
Western blotting filter paper 7 cm X 8.4 cm	Thermo Fisher Scientific, Waltham, USA
XCell II blot module	Thermo Fisher Scientific, Waltham, USA

β-tubulin rabbit monoclonal antibody (2128s)	Cell Signaling Technology, Danvers, USA

Kits	
Bradford protein assay	Bio-Rad Laboratories, Hercules, USA
Caspase-Glo 3/7 assay	Promega, Madison, USA
Cyto-ID Autophagy detection kit 2.0	Enzo Life Sciences, Lausen, CH
Duolink In situ red starter kit, Mouse/rabbit (Proximity ligation assay, PLA)	Sigma Aldrich, St. Louis, USA
DuoSet ELISA Ancillary reagent kit 2	R & D systems, Minneapolis, USA
High capacity RNA-to-cDNA kit	Thermo Fisher Scientific, Waltham, USA
Human CCL5/RANTES DuoSet ELISA kit	R & D systems, Minneapolis, USA
Human CD34 MicroBead Kit	Miltenyi Biotech, Bergisch Gladbach, DE
Human CXCL10/IP10 DuoSet ELISA kit	R & D systems, Minneapolis, USA
Human IFN-beta Duoset ELISA kit	R & D systems, Minneapolis, USA
ProFection Mammalian Transfection System	Promega, Madison, USA
PureYield Plasmid Midiprep System	Promega, Madison, USA
PureYield Plasmid Miniprep System	Promega, Madison, USA
RNeasy mini kit	Qiagen, Hilden, DE

Media, supplements and cell culture	
Accutase	Sigma Aldrich, St. Louis, USA
Ambion nuclease-free water	Thermo Fisher Scientific, Waltham, USA
B27 w/o vitamin A	Thermo Fisher Scientific, Waltham, USA
Cell titer blue (CTB)	Promega, Madison, USA
Collagenase/Dispase	Sigma Aldrich, St. Louis, USA
Crystal violet	Amresco LLC, Solon, USA
Dimethyl sulfoxide (DMSO)	AppliChem GmbH, Darmstadt, DE
Dulbecco's modified eagle medium (DMEM)	Thermo Fisher Scientific, Waltham, USA
Dulbecco's phosphate buffered saline (DPBS)	Thermo Fisher Scientific, Waltham, USA
Hanks balanced salt solution (HBSS)	Thermo Fisher Scientific, Waltham, USA
Heat inactivated fetal bovine serum (FBS)	Thermo Fisher Scientific, Waltham, USA
Human epidermal growth factor (EGF)	PeproTech, Rocky Hill, USA
Human fibroblast growth factor (FGF)	PeproTech, Rocky Hill, USA
Human Flt3	PeproTech, Rocky Hill, USA
Human stem cell factor (hSCF)	PeproTech, Rocky Hill, USA

Human thrombopoietin (hTPO)	PeproTech, Rocky Hill, USA
Incubator clean	AppliChem GmbH, Darmstadt, DE
Interleukin-3 (IL3)	PeproTech, Rocky Hill, USA
L-glutamine	Sigma Aldrich, St. Louis, USA
Neurobasal-A Medium	Thermo Fisher Scientific, Waltham, USA
Opti-MEM reduced serum medium (Optimem)	Thermo Fisher Scientific, Waltham, USA
Recovery cell culture freezing medium	Thermo Fisher Scientific, Waltham, USA
Red blood cell lysis buffer	Sigma Aldrich, St. Louis, USA
X-Vivo 20 medium	Lonza group, Basel, CH
Miscellaneous	
1.5 mL, 2 mL, 5 mL tubes	Sarstedt, Nümbrecht, DE
10 µL, 1000 µL filter tips	Nerbe plus GmBH, Winsen, DE
12-well, 24 -well plate	Sarstedt, Nümbrecht, DE
15 and 50 mL tubes	Cellstar, GBO GmbH, Kremsmünster, AU
2.5 µL, 100 µL, 200 µL filter tips	Sarstedt, Nümbrecht, DE
35mm petri dish	Corning Incorporated, Corning, USA
15cm petri dish	Techno Plastic Products AG, Trasadingen, CH
6-well, 96-well plate	Techno Plastic Products AG, Trasadingen, CH
8-well chamber slides	Sarstedt, Nümbrecht, DE
Amicon Ultra-15 Ultracel-3K centrifugal filters	Merck Millipore, Burlington, USA
BD falcon 2-well and 4-well chamber slides	BD Biosciences, Bedford, USA
Cell culture flasks (T25, T75, T175)	Cellstar, GBO GmbH, Kremsmünster, AU
Cell scraper	Corning Incorporated, Corning, USA
Costar stripettes	Corning Incorporated, Corning, USA
Cover slips 24x60 mm	R. Langenbrinck, Emmendingen, DE
Cryotubes 2 mL	GBO GmbH, Kremsmünster, AU
Culture tubes 14 ml	GBO GmbH, Kremsmünster, AU
Freezing container	Thermo Fisher Scientific, Waltham, USA
Laminin	Sigma Aldrich, St. Louis, USA
Micropipettes	Eppendorf, Mississauga, CA
OptiSeal ultracentrifuge tubes	Beckman Coulter, Brea, USA

Permanent mounting Medium	Vector laboratories Inc., Burlingame, USA
Poly-L lysine (PLL)	Sigma Aldrich, St. Louis, USA
Plasmids	
pEMC-La (L protein expression plasmid for production of MeV)	Kind gift by Prof. Dr. Stephen Russell, (Mayo Clinic) Rochester, USA
pMeV-eGFP (GFP expression plasmid for production of MeV)	Kind gift by Prof. Dr. Stephen Russell, (Mayo Clinic) Rochester, USA
pSc-N (Nucleocapsid expression plasmid for production of MeV)	Kind gift by Prof. Dr. Stephen Russell, (Mayo Clinic) Rochester, USA
pSIN_GFP (3rd generation lentiviral vector plasmid encoding GFP)	Kind gift by Prof. Dr. Manuel Grez, (Georg Speyer Haus) Frankfurt, DE
pMDL.g/p.RRE (3rd generation lentiviral packaging plasmid)	A kind gift from Didier Trono (Addgene plasmid # 12251)
pRSV.Rev (3rd generation lentiviral Rev expressing plasmid)	A kind gift from Didier Trono (Addgene plasmid # 12253)
pMD2.G (2nd and 3rd generation lentiviral envelope plasmid)	A kind gift from Didier Trono (Addgene plasmid # 12259)

2.2 Methods

2.2.1 Long-term glioma cell lines and adherent cell culture

The human long term glioma cell lines LN229, LNZ308, human embryonic kidney cells 293T, were obtained from American type culture collection (ATCC, Manassas, USA) and cultured in Dulbecco's Modified Eagle Medium (Thermo Fisher Scientific, Waltham, USA) supplemented with 10% fetal bovine serum and 50 µg/ml gentamycin (Thermo Fisher Scientific). African green monkey kidney cells Vero B4 cells were obtained from Leibniz Institute DSMZ - German Collection of Microorganisms and Cell Cultures GmbH (DSMZ, Braunschweig, Germany). The human colorectal adenocarcinoma cell line HT-29 was a kind gift by Prof. Ulrich M. Lauer (Universitätsklinikum Tübingen, Tübingen, Germany) and the measles virus producer cell line 293-3-46 was a kind gift by Prof. Stephen Russell (Mayo Clinic, Rochester, USA) [39]. The Vero B4 and HT-29 cells were cultured similar to long term glioma cell lines in DMEM supplemented with 10% FBS and 50 µg/ml gentamycin (Complete DMEM). The 293-3-46 cells were cultured in DMEM supplemented with 10% FBS and 1.2 mg/ml geneticin. All cell lines were cultured at 37°C with 5% CO_2.

2.2.2 Glioma stem-like cell cultures

The glioma stem-like (GS) cell lines GS3, GS8 were kindly provided by Katrin Lamszus [40] and cultured in Neurobasal medium (Thermo Fisher Scientific) supplemented with 20 ng/ml recombinant human fibroblast growth factor (Peprotech, New Jersey, USA), 20 ng/ml recombinant human epidermal growth factor (Peprotech), 2 mM L-glutamine (Thermo Fisher Scientific), 10% B-27 supplement (Thermo Fisher Scientific) and 50 µg/ml gentamycin (Thermo Fisher Scientific). All GS cells were cultured at 37°C with 5% CO_2.

2.2.3 Harvest and culturing of primary glioblastoma cells

The primary glioblastoma cell lines T81/16, T708/16, T1094/17 were harvested from fresh glioblastoma tissue obtained from patients undergoing surgery at the Department of Neurosurgery, University Hospital Tübingen (Ethical approval number: 456/2009B02). The glioblastoma tissue was cut into fine pieces using two sterile scalpels in a 35 mm petridish and transferred to a 50 ml falcon using 10 ml hanks balanced salt solution (HBSS, Thermo Fisher Scientific) with centrifugation at 250 g for 5 minutes (mins). The tissue pellet was washed thrice with HBSS and resuspended in 5 ml of Neurobasal medium with 10 µg/ml of collagenase / dispase solution (Sigma Aldrich). The medium containing collagenase/ dispase was incubated at 37°C in a water bath with continuous shaking for 30 mins. The pellet was washed thrice with Neurobasal medium and later filtered using a 70 µm filter (Thermo Fisher Scientific) to collect cell suspension. The cell suspension was centrifuged at 250 g for 5 mins and the pellet resuspended in 1 ml Red blood cell lysis buffer (Sigma Aldrich) and incubated for 7 mins at

room temperature. The cells are finally washed thrice with HBSS to remove all lysed red blood cells and cultured in Neurobasal medium (Thermo Fisher Scientific) supplemented with 20 ng/ml recombinant human fibroblast growth factor (FGF, Peprotech), 20 ng/ml recombinant human epidermal growth factor (EGF, Peprotech), 2 mM L-glutamine (Thermo Fisher Scientific), 10% B-27 supplement (Thermo Fisher Scientific) and 50 µg/ml gentamycin (Thermo Fisher Scientific) with addition of EGF/FGF every two days. All primary glioblastoma cells were cultured at 37°C with 5% CO_2.

2.2.4 Isolation and culturing of hematopoietic progenitor cells (HPCs)

Hematopoietic progenitor cells (HPCs/CD34$^+$) were isolated from human peripheral blood samples using CD34 microbead kit (Miltenyi Biotec, Bergisch Gladbach, Germany) according to manufacturer's instructions and cultured at a cell density of 10^6 cells per ml in X-vivo 20 medium (Lonza, Basel, Switzerland) supplemented with 100 ng/ml each of human stem cell factor (Peprotech), human thrombopoietin (Peprotech), human Flt3 (Peprotech) and 10 ng/ml of interleukin 3 (Peprotech).

2.2.5 Revival of bacterial colonies containing plasmid constructs

A loop full of bacterial glycerol stock containing plasmid construct were streaked onto LB agar plates containing 100 µg/ml Ampicillin (Sigma Aldrich, St. Louis, USA) and incubated at 37˚C overnight to allow colony formation. The colonies grown overnight on Luria Bertani (LB) agar plates were individually picked using a sterile loop and inoculated in 5 ml of LB broth containing Ampicillin for overnight incubation at 37˚C.

2.2.6 Small scale preparations of plasmid DNA ('Minipreps')

Plasmid DNA was extracted from 5 ml of bacterial culture grown overnight at 37˚C using PureYield plasmid miniprep system (Promega, Madison, USA) according to manufacturer's instructions.

2.2.7 Large scale preparations of plasmid DNA ('Maxipreps')

Plasmid DNA were extracted from 500 ml of bacterial culture grown overnight at 37˚C and eluted in 250 µl of nuclease-free water using Qiagen plasmid maxi kit (Qiagen, Hilden, Germany) according to manufacturer's instructions.

2.2.8 Determination of nucleic acid concentration

The concentration of DNA/RNA was measured using NanoDrop ND-1000 Spectrophotometer (Thermo Fisher Scientific) calibrated with the respective elution buffer at a mean wavelength of 260 nm to observe a clear peak indicating the purity of extracted DNA/RNA.

2.2.9 Restriction endonuclease digestion of plasmid DNA

1 µg of plasmid DNA was used as a template in a 20 µl reaction containing 1-2 µl of restriction enzyme with 2 µl of compatible buffer and 2 µl BSA for enhanced enzyme activity. The samples were briefly mixed and incubated at 37°C water bath for 2 h.

2.2.10 Agarose gel electrophoresis

2% agarose gel was prepared by dissolving required amount of agarose powder in 1X Tris-Acetate-EDTA (TAE; Applichem, Gatersleben, Germany) through heating in a microwave followed by addition of 10000X GelRed (Biotium, Hayward, USA) at lukewarm temperature. The gel was poured onto gel trays for solidification following which the comb was removed and gel placed in the tank containing 1X TAE. The DNA samples were mixed with gel loading buffer and loaded into the wells along with a standard 1 Kb plus DNA ladder (Thermo Fisher Scientific). Samples were allowed to electrophorese at 110 V for approximately 1 hour followed by image capture using the ChemiDoc MP system (Bio-Rad Laboratories, Hercules, USA).

2.2.11 Production of 3rd generation lentiviral vectors

Lentivirus pSIN_GFP was produced and titers determined as described previously [41]. Briefly, 1.5 x 10^7 293T cells were seeded in T-175 flasks and incubated at 37°C, 5% CO_2 the day before transfection for cells to achieve 80-90% confluency. Transfection mixture for each flask was prepared as described: 50 µg of vector plasmid (pSIN_GFP), 32.5 µg of packaging plasmid (pMDL.g/p.RRE), 12.5 µg of pRSV.Rev and 17.5 µg of VSV-G envelope plasmid (pMD2.G), were added to 5 ml of Optimem and filtered through a 0.22 µm filter. Similarly, 1 µl of 10 mM Polyethyleneimine (PEI; Sigma Aldrich, St. Louis, USA) was added to 5 ml of Optimem and filtered through a 0.22 µm filter. The two mixtures containing DNA and PEI were mixed and incubated at room temperature for 20 minutes. 10 ml of DNA-PEI complex was added to each T-175 flask and incubated at 37°C, 5% CO_2 for 4 hours following which the media was replaced with 18 ml of fresh complete DMEM. The existing media was harvested 48 hours post infection (hpi) and replaced with fresh complete DMEM, which was subsequently harvested 24 hours later. The harvested media containing virus is centrifuged at 2700 g for 10 mins and filtered through a 0.22 µm filter. 32 ml of the filtered supernatant was added per OptiSeal centrifuge tube (Beckman Coulter, Brea, USA) and all tubes were loaded onto the rotor and centrifuged at 100,000 g for 2 hours at 4°C (Beckman Coulter). The supernatant was carefully decanted and the pellet resuspended in 50 µl of Optimem per tube. The tubes were covered with parafilm and incubated on ice for 1 hour. Finally, the media was pipetted 10-15 times to resuspend the virus and aliquots of 30 µl were transferred to cryovials for storage at -80°C.

2.2.12 Titration of 3rd generation lentiviral vectors

10^5 cells of 293T were seeded in a 12-well plate made up to a final volume of 1 ml with complete DMEM and incubated overnight at 37°C with 5% CO_2. The following day cells were transduced with 5 µl, 10 µl, and 20 µl of concentrated virus in a total volume of 1 ml complete DMEM for 96 h. Transduced 293T cells were harvested 96 hours post transduction and centrifuged at 1100 g for 10 minutes. The supernatant was discarded and cells resuspended in 250 µl of PBS + 10% FCS for flow cytometric analysis. CyAn ADP flow cytometry analyser (Dako, Glostrup, Denmark) was used for detecting fluorescent cells expressing GFP and the data analysed using FlowJo software version 7.2.4 (Tree Star Inc, Ashland-OR, USA). The lentiviral titers were determined empirically using the following formula (Fig.1).

$$\text{Viral Titer (IU/ml)} = \frac{(\text{No. of cells seeded} * \text{dilution factor} * \text{Percentage of GFP positive cells})}{\text{Volume of virus solution added in ml}}$$

Figure 1. Emperical formula for calculation of lentiviral titer (Infectious Units/ml) using flow cytometry.

2.2.13 Lentiviral transduction of glioma cells

LN229 and LNZ308 cells were seeded as 5 X 10^4 cells in 12-well plates one day before transduction. The cells were transduced with GFP-expressing lentivirus, pSIN_GFP at 10 multiplicity of infection (MOI) to generate GFP$^+$ LN229 and GFP$^+$ LNZ308 cells, which were cultured similar to parental cells.

2.2.14 Measles virus production and amplification

The Edmonston strain of measles virus (NSe) encoding green fluorescent protein (GFP) were kindly provided by Dr. Michael Mühlebach (Paul Ehrlich Institute, Langen, Germany) and the rapidly maturing variant of Discosoma sp. red fluorescent protein (DsRed) was provided by Dr. Ulrich M. Lauer (Universitätsklinikum Tübingen, Tübingen, Germany). However, to maintain sufficient stock of virus we amplified the virus in Vero B4 cells. 10^7 Vero B4 cells were seeded in 15 cm petridish and incubated at 37°C with 5% CO_2. The confluent cell layer were infected with 0.03 multiplicity of infection (MOI) of MeV-GFP and incubated at 37°C for about 36-48 h up till all cells appeared as syncytia. The syncytial cells were completely scraped in 1ml of Optimem per dish and snap frozen in liquid nitrogen. The frozen suspension was thawed at 37°C and vortexed strongly to be centrifuged at 2000 g at 4°C for 15 min. The supernatant was harvested and transferred to cryovials as 300 µl aliquots to be frozen at -80°C.

23

2.2.15 Determination of MeV-GFP viral titer

The viral titers were determined by 50% tissue culture infective dose titration (TCID$_{50}$) by Kärber method [42]. 10^4 Vero B4 cells were seeded in a 96-well plate in 200 µl of complete DMEM along with another 96-well plate with 12 wells each containing 270 µl of complete DMEM. The virus stock thawed at 37°C were added as 30 µl of viral suspension into the first of the twelve wells. The resulting mixture was resuspended and 30 µl of the dilution from above were transferred to the next well. This was repeated resulting in a series of twelve 10-time dilution factors which were then transferred into all eight rows of the plate containing the Vero B4 cells with 30 µl per well. So eight wells of Vero B4 cells were infected with one virus dilution and the plate incubated at 37°C for 96 h. 96 hpi the readout was a binary identifying the presence of fluorescent syncytia defined as either 'positive' or 'negative' visualized by fluorescence microscopy. The binary readout was incorporated in the following formula (Fig. 2) to calculate TCID$_{50}$/ml. The TCID$_{50}$/ml was converted to Pfu/ml using the formula: **Pfu/ml = 0.7 X TCID$_{50}$/ml** and the determined plaque forming units used to calculate MOI for infectivity studies.

$$\frac{TCID_{50}}{ml} = \frac{10^{\text{dilution step log10} + 1 \times \left(\frac{\text{total number of positive wells}}{\text{number of wells per dilution factor}} - 0.5\right)}}{\text{Volume of virus used (ml)}}$$

Figure 2. Emperical formula for calculation of 50% tissue culture infectious dose (TCID$_{50}$/ml) for oncolytic measles virus.

2.2.16 Flow cytometry for basal CD46 receptor expression

Cells were counted and 10^5 cells stained with 0.25 µg antibody (either CD46-PE or IgG1κ-PE; Thermo Fisher Scientific). The CD46 receptor expression was measured along with viability dye, 7-aminoactinomycin D (7-AAD; Thermo Fisher Scientific) in MACSQuant Analyzer 10 (Miltenyi Biotec, Bergisch Gladbach, Germany). The ratio of mean fluorescence intensities of PE-conjugated CD46 vs isotype control (IgG1κ) were calculated and graphs generated using GraphPad Prism 6 software (GraphPad Software, La Jolla, USA).

2.2.17 CD46 receptor expression after treatments *in vitro*

LN229 and LNZ308 cells were seeded as 10^5 cells in T-25 flasks one day before treatment initiation. The cells were treated with TMZ (0 µM, 10 µM, 100 µM or 1000 µM), γ irradiation (0 Gy, 1 Gy, 2 Gy or 4 Gy) and under different oxygen conditions (21% O_2 (normoxia) or 1% O_2 (hypoxia)) for 48h. Levels of CD46 receptor expression were determined via flow cytometry as described above, along with viability staining using 7-aminoactinomycin-D (7-AAD).

2.2.18 Fluorescence microscopy

Cells were seeded as 5 X 10^5 cells in 2-well glass chamber slides coated with 20 µg/mL poly-L-lysine (PLL, Sigma Aldrich) alone for adherent cells or along with 5 µg/mL laminin (Sigma Aldrich) for suspension cultures in 2-well chamber slides one day before transduction with MeV-GFP at 1 MOI for 72 hours at 37°C. Cells were fixed with 4% paraformaldehyde followed by nuclear staining with 4′,6-diamidino-2-phenylindole (DAPI; Thermo Fisher Scientific). Images were captured with Zeiss microscope using Apotome (Carl Zeiss, Oberkochen, Germany) and image analysis carried out with Axiovision software (Carl Zeiss).

2.2.19 Co-culture assay of MeV infected HPC with GFP$^+$ glioma cells

GFP$^+$ LN229 and GFP$^+$ LNZ308 cells were seeded as 10^4 or 10^5 cells on 8-well chamber slides coated with PLL one day before co-culture with MeV-transduced HPCs. The HPCs were transduced at 1 MOI using MeV-DsRed and co-cultured with glioma cells at differing ratios of glioma cells to transduced HPCs, viz., 1:0 (No HPC), 1:10, 1:1 and 10:1, over a period of 192 hpi. A ratio of 1 indicated 10^4 cells, while 10 signified 10^5 cells in the co-culture ratios (Fig. 3). The cells were counterstained with DAPI before proceeding towards image capture at different time points (0 hpi, 24 hpi, 48 hpi, 96 hpi, 144 hpi and 196 hpi) using Zeiss microscope with Apotome (Carl Zeiss) and images analysed with Axiovision software (Carl Zeiss) as described above.

					Ratio of Glioma cells : HPCs
LN229	**Blank** **1:0**	**1:10**	**1:1**	**10:1**	10^4 cells ← 1 : 0 → No cells
					10^4 cells ← 1 : 10 → 10^5 cells
LNZ308	**Blank** **1:0**	**1:10**	**1:1**	**10:1**	10^4 cells ← 1 : 1 → 10^4 cells
					10^5 cells ← 10 : 1 → 10^4 cells

Figure 3. Schematic of 8-well chamber slide for co-culture experiment. *The ratio of GFP$^+$ glioma cells to MeV-DsRed infected HPCs are as enumerated.*

2.2.20 LC3-GFP puncta assay

Cells of LN229 and T1094/17 were seeded as 10^5 cells on 8-well chamber slides coated with PLL (LN229) and along with laminin (T1094/17) one day before treatment initiation. The cells were treated with different treatment regimens (Blank, VT, RT) in serum-free medium followed by serum supplementation and stained for LC3-GFP along with nuclear Hoechst 33342 using CYTO-ID Autophagy detection kit 2.0 (Enzo Life Sciences, Lausen, Switzerland) as per manufacturer's instructions. Images were captured with Zeiss microscope using Apotome (Carl Zeiss) and image analysis carried out with Axiovision software (Carl Zeiss).

2.2.21 Acute cytotoxicity assay

LN229 and LNZ308 were seeded as 5000 cells per well in 96-well plates one day before treatment initiation. All treatments were carried out in serum-free DMEM with their respective controls and cell viability measured at 72 hours post initial treatment (hpt) using Cell titer blue solution (Promega) as per manufacturer's instructions. The measured values were converted to percentage cell viability by normalising each treatment to its respective control within the individual regimens.

2.2.22 Determination of EC$_{50}$ using acute cytotoxicity assay

LN229 and LNZ308 were seeded as 5000 cells per well one day before treatment initiation. The determination of EC$_{50}$ for Lomustine (CCNU) were carried out in 2 µm increments for LN229 (0 µM – 20 µM) and in 7.5 µM increments for LNZ308 (0 µM – 75 µM) in serum free medium with DMSO controls for each concentration. Cell viability was measured at 72 hpt using Cell titer blue solution (Promega) as per manufacturer's instructions and the measured values were converted to percentage cell viability by normalising each treatment to 0 µM within each cell line. The CCNU concentration corresponding to 50% viability in respective cell line were defined as EC$_{50}$ value.

2.2.23 Clonogenic survival Assay

LN229 and LNZ308 were seeded as 1000 cells per well in 6 well plates one day before treatment initiation. All treatments were carried out in serum-free DMEM with their respective controls and cells allowed to form clones defined as individual population consisting of > 50 cells. The cells were stained with 0.5% crystal violet solution (dissolved in 20% methanol) and clones counted manually.

2.2.24 Generating temozolomide resistant cells

Temozolomide (TMZ) resistant cell line R-LN229 were generated by repetitive exposure of parental LN229 to TMZ as has been previously described [43]. Briefly, parental LN229 were

seeded as 1000 cells in 6 well plates and treated with 100 µM of TMZ in triplicates over a period of 10 days. The surviving fraction of cells were harvested and susbequent rounds of TMZ treatment continued as described above. Cells were considered resistant when treated cells exhibited significant clonogenic survival in comparison to parental cell line.

2.2.25 Cytotoxic survival Assay

We designed a cell viability assay to determine the oncolytic cascade effect initiated by the measles virus in combination with cytotoxic agents, such as TMZ. Herein, measurement of cytotoxicity associated with recurrent ineffective mismatch repair or lysis of MeV induced syncytia require longer readout periods of 144 hpt as opposed to a classical 72 hpt acute cytotoxicity assay.

LN229, R-LN229 and LNZ308 were seeded as 5000 cells per well in 96 well plates one day before treatment initiation with γ-irradiation (RT), alkylating chemotherapy (CT), measles virotherapy (VT) alone or sequentially as combinatorial regimens in serum-free DMEM at the indicated concentrations or doses. The cell viability was measured at 144 hpt using Cell titer blue solution (Promega) as per manufacturer's instructions and measured values were converted to percentage cell viability by normalising each treatment to its respective control within the individual regimens.

GS8 cells were seeded as 50,000 cells per 35 mm dish one day before treatment initiation and all treatments performed in serum-free neurobasal medium. The measurement of cell viability were performed in triplicates with 5000 cells at 144 hpt using Cell titer blue solution (Promega) as described previously. The graphs were generated using GraphPad Prism 6 with percentage cell viability post treatments and synergistic regimens were identified.

2.2.26 Chou-Talalay fractional product method

The predicted values of combinations used to determine synergy were calculated from the individual monotherapies, RT, CT and VT by Chou-Talalay fractional product method defined as the product of the viable fractions after treatment with all agents alone [44]. If the observed value of the co-treatment is less than that of the calculated predictive value (Fig. 4), the combination of agents were deemed to be synergistic and not only additive.
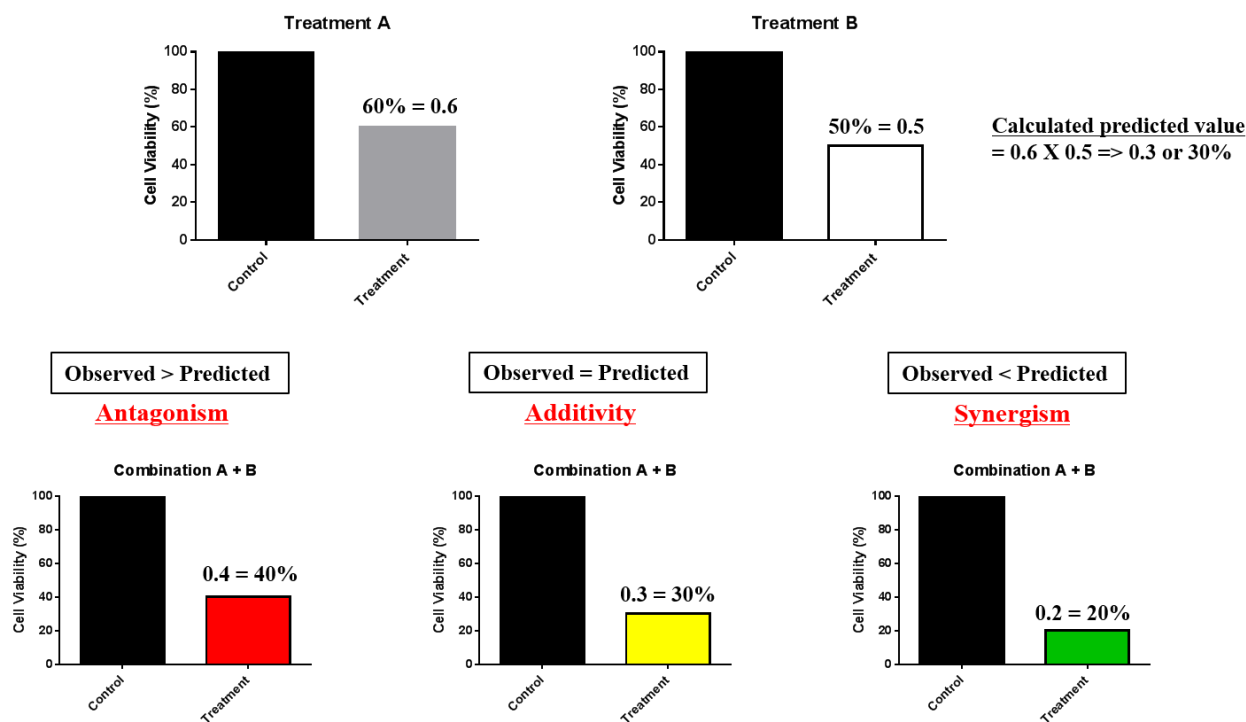
Figure 4. Diagrammatic representation of synergy calculation. *Calculated predicted values from monotherapies were compared against cell viabilities of observed combination treatments to determine antagonism, additivity or synergism as described.*

2.2.27 Immunoblotting

The cells were lysed in lysis buffer containing 25 mM Tris hydrochloric acid (Tris-HCl), 120 mM sodium chloride (NaCl), 5 mM ethylenediaminetetraacetic acid (EDTA), 0.5% NP-40 and phosphatase inhibitor cocktails (Sigma Aldrich). The lysed cells were centrifuged at 16000 g for 20 mins at 4°C and supernatant containing protein was harvested. The protein concentration was determined by using Bradford protein assay kit (Bio-Rad Laboratories) and 20 μg of protein was used for western blotting. Proteins were separated on 4-12% Bis-tris polyacrylamide gels (Thermo Fisher Scientific) followed by transfer to PVDF membranes (Thermo Fisher Scientific). The blots were blocked in Tris-buffered saline containing 5% skim milk (Becton Dickinson, New Jersey, USA) and 0.05% Tween 20 (Sigma Aldrich) for 1 hour. Protein blots were probed with primary antibodies overnight at 4°C and 1 hour at room temperature with horseradish peroxidase-coupled secondary antibodies (Abcam, Cambridge, UK) the following day. Protein bands were visualized using Pierce chemiluminescent substrate solutions (Thermo Fisher Scientific) and image capture and analysis carried out with ChemiDoc MP imaging system (Bio-Rad Laboratories, Hercules, USA) using Image lab software (Bio-Rad Laboratories, Hercules, USA).

2.2.28 Enzyme linked immunosorbent assay (ELISA)

LNZ308 cells were seeded as 3 X 10^6 cells per dish and treated with different regimens as described above, supernatants were harvested after 96 hpt and concentrated using Amicon Ultra-15 Ultracel-3K centrifugal filters (Merck Millipore, Burlington, USA) with subsequent determination of whole protein using Bradford protein assay kit (Bio-Rad Laboratories). The respective chemokine/cytokine concentration were determined enzymatically per microgram of whole protein using respective DuoSet ELISA kits according to manufacturer's instructions (R&D Systems, Minneapolis, USA).

2.2.29 Generating lysates for RNA sequencing

LNZ308 cells were seeded as 3 X 10^6 cells per dish and treated with monotherapies (RT, 2 Gy; CT, 130 µM; VT, 0.05 MOI), double regimen (CT-VT, 130 µM - 0.05 MOI), synergistic triple regimen (CT-VT-RT, 130 µM - 0.05 MOI - 2 Gy) along with untreated basal control Blank (0 hpt), DMSO control for CT initiated regimens, and Ctrl (R/V) serving as control for RT alone and VT alone regimens under serum-free conditions. The sample lysates including RNA and protein were harvested at 0 hpt, 36 hpt, 72 hpt and 96 hpt upon completion of treatment regimens and stored at -80°C. The samples harvested at 0 hpt, 36 hpt and 96 hpt (highlighted in green, Fig. 5) were processed for RNA sequencing while 72 hpt samples (highlighted in blue, Fig. 5) were used for transcriptome validation experiments.
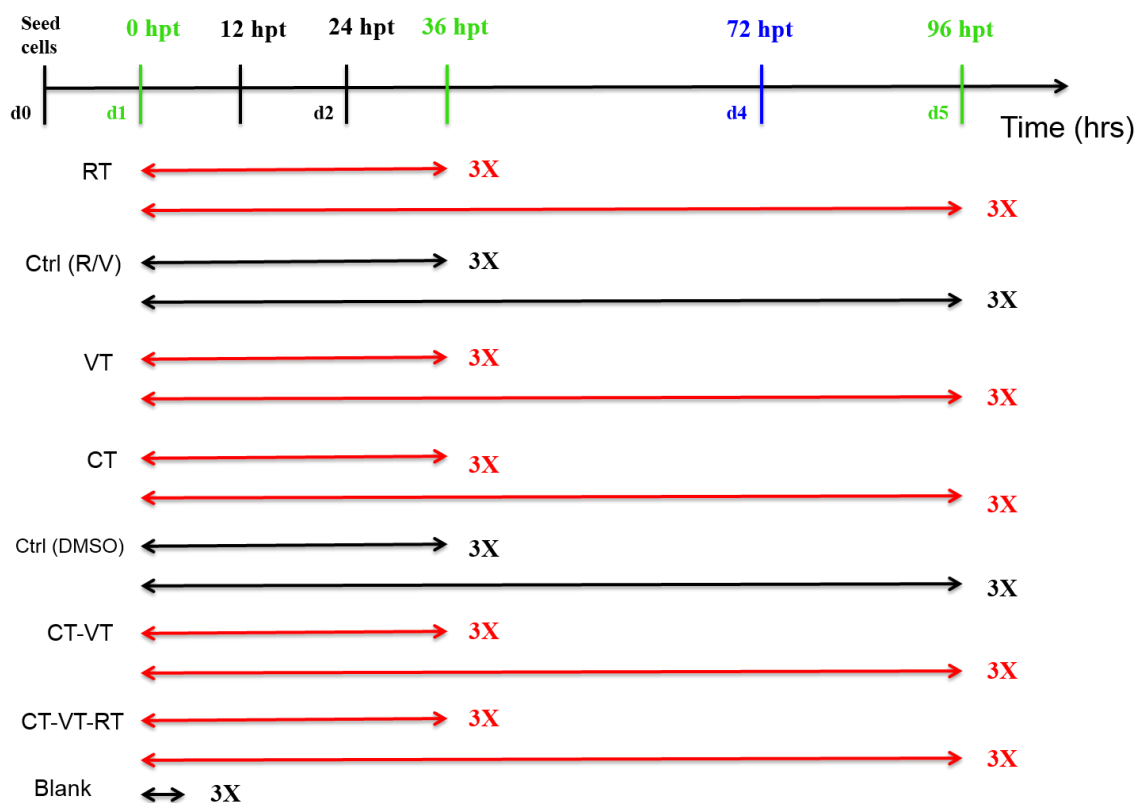

Figure 5. Timescale plot of samples in triplicates for RNA sequencing upon treatments.

2.2.30 RNA Sequencing and analysis

RNA was isolated at 36 hpt and 96 hpt using RNeasy Mini kit (Qiagen) according to manufacturer's instructions and quality assessed with an Agilent 2100 Bioanalyzer. Samples with high RNA integrity number (RIN > 8) were selected for library construction. Using the TruSeq Stranded RNA Sample Prep Kit (Illumina, San Diego, USA) and 400 ng of total RNA for each sequencing library, poly(A) selected single-read sequencing libraries (68 bp read length) were generated according to the manufacturer's instructions. All libraries were sequenced on an Illumina HiSeq2500 platform (Illumina) at a depth of 18-20 million read search. Library preparation along with sequencing procedures were performed by the same individual and a design aimed to minimize technical batch effects was chosen. Raw fastq files were pre-filtered using the chastity filter to remove reads that contain a "Y" flag. FastQC (Andrews S. (2010). FastQC: a quality control tool for high throughput sequence data. Available online at: http://www.bioinformatics.babraham.ac.uk/projects/fastqc) was used to determine quality of the resulting fastq files. Subsequently, adapter trimming/removal process was conducted with Cutadapt (https://pypi.python.org/pypi/cutadapt/), version 1.8.3) [45]. This step used the FastQC output to identify reads that showed a match to some typical overrepresented (Illumina) sequences/adapters. TopHat2 was used as aligner to map the quality controlled remaining reads to the human genome [46]. Read counting to features (genes) in the genome was performed with HTSeq (http://www-huber.embl.de/users/anders/HTSeq/doc/count.html, version 0.6.0.) [47]. Counting was performed using "union" mode on the feature "gene_id" where each gene is considered here as the union of all its exon counts. The stranded option was also set to "stranded=no" to count features on both strands. For differential expression analysis the raw read count table provided by HTSeq was used into the R package DESeq2 (version 1.10.1) [48]. Adjusted p-values were used at an FDR (False Discovery Rate) < 0.05 to account for multiple hypothesis testing.

2.2.31 Quantitative real-time PCR (qPCR)

RNA extractions were performed using the RNeasy mini kit (Qiagen) and reverse transcribed to cDNA using High-Capacity RNA-to-cDNA kit (Thermo Fisher Scientific) according to manufacturer's instructions. For each qPCR reaction, 20 ng of cDNA was amplified with custom designed primers (Table 1) and qPCR Mastermix Plus for SYBR Green (Eurogentec, Liege, Belgium) using the 7500 Fast Real time PCR system (Thermo Fisher Scientific). Relative gene expression was determined using the $\Delta\Delta$-CT method versus the housekeeping gene ARF1.

Gene	Forward Primer (5'→3')	Reverse Primer (5'→3')
ARF1	GACCACGATCCTCTACAAGC	TCCCACACAGTGAAGCTGATG
DDX58	AGACAAAGATGAAGAGAGCAGGA	GCTCGGACATTGCTGAAGAAG
HLA-A	GAGTATTGGGACCAGGAGACA	CGTCGCAGCCATACATTATCTG
HLA-B	TGAGATGGGAGCCGTCTTC	CTACACATCACAGCAGCGAC
IFIH1	CGGATATAAAGAATGTAACATTGTTATC	ATGAGCATACTCCTCTGGTTTCA
IFIT1	CCTCCTTGGGTTCGTCTACA	GGCTGATATCTGGGTGCCTA
IFN-β	GTCTCCTCCAAATTGCTCTCC	CAGTATTCAAGCCTCCCATTCA
ISG15	ATGGGCTGGGACCTGACG	GCCGATCTTCTGGGTGATC
MX1	CGCTGGTGCTGAAACTGAAGA	GCGATGGCATTCTGGGCTTTA
MX2	AGTTCAGAATGGAGCAGATGG	ACCGAAGACTCATTACTGGGAA
OAS1	CACAGAACTACAGAGAGACTTC	CAAGCATAGACCGTCAGGAG
OAS2	GACTTCTCCCAACCTGGATAATG	CTGTCAATCTGCTCTAGGAAGC
STAT1	CAGAACAGAGAACACGAGACCA	GTTCAGTGACATTCAGCAACTCTA
TAP1	AAAGACACTCAACCAGAAGGAG	GCCCACCAATGTAGAGGATTC

Table 1. List of primers used for qRT-PCR analysis. *The forward and reverse primers used for validation of genes identified from RNASeq using qRT-PCR.*

2.2.32 Functional inhibition of IFN-β and JAK-STAT pathway

LNZ308 cells were seeded as 3×10^6 cells per dish, and treated with synergistic CT-VT-RT regimen as described previously (2.2.29). TBK1/IKKε inhibitor, BX795 was purchased from Invivogen (Invivogen, San Diego, USA) and used at a concentration of 10μM [49]. Fludarabine was purchased from Selleckchem (Selleckchem, Houston, USA) and used as a functional STAT1 inhibitor at a concentration of 100μM [50]. At 36 hpt after completion of CT-VT-RT, IFN-β inhibitor (BX795) and STAT1 inhibitor (fludarabine) were added alone or in combination along with suitable DMSO control to obtain five regimens; CT-VT-RT alone, CT-VT-RT + fludarabine (100 μM), CT-VT-RT + BX795 (10 μM), CT-VT-RT + fludarabine (100 μM) + BX795 (10 μM), CT-VT-RT + DMSO (110 μM). The RNA, protein and supernatants were harvested at 96 hpt for further analysis.

2.2.33 Proximity ligation assay

LNZ308 cells were seeded as 5 X 10^4 cells in 8-well chamber slides coated with PLL, and treated with synergistic regimen as described previously. Following CT-VT-RT, the cells were treated with respective small molecule inhibitors as described above (2.2.32), and fixed in 4 % paraformaldehyde solution at 96 hpt. The cells were subjected to proximity ligation assay using Duolink In Situ red starter kit Mouse/Rabbit (Sigma Aldrich) along with suitable IgG controls as per manufacturer's instructions. Images were captured with Zeiss microscope using Apotome (Carl Zeiss) and image analysis carried out with Axiovision software (Carl Zeiss).

2.2.34 Isolation of HLA ligands

Cells subjected to treatment regimens as mentioned above were harvested at 96 h (highlighted in green), washed twice with cold phosphate buffered saline (PBS; Lonza), frozen at -80°C with subsequent iosolation of HLA class I molecules using standard immunoaffinity purification as described previously [51,52]. In brief, cell pellets were lysed in 10 mM 3-[(3-Cholamidopropyl)-Dimethylammonio]-1-Propanesulfonate (CHAPS; Applichem) /PBS (Lonza) containing protease inhibitor (Roche, Basel, Switzerland). HLA molecules were purified using the pan-HLA class I–specific monoclonal W6/32 Ab, which is covalently linked to CNBr-activated Sepharose (GE Healthcare, Little Chalfont, U.K.). Repeated addition of 0.2% trifluoroacetic acid (Merck Millipore) eluted HLA molecules and peptides. The peptides were isolated employing ultrafiltration with centrifugal filter units (Merck Millipore), extracted and desalted using ZipTip C18 pipette tips (Merck Millipore). Peptides were then eluted in 35 µL acetonitrile (Merck Millipore)/0.1% trifluoroacetic acid, vacuum centrifuged to 5 µL, and resuspended in 25 µL of 1% acetonitrile/0.05% trifluoroacetic acid. Finally, the peptide solutions were stored at -20℃ until analysis by LC-MS/MS.

2.2.35 Analysis of HLA Ligands by LC-MS/MS

Peptide were separated using reversed-phase liquid chromatography (nanoUHPLC, UltiMate 3000 RSLCnano, Dionex) and analysed in an on-line coupled LTQ Orbitrap XL hybrid mass spectrometer (Thermo Fisher Scientific). In five technical replicates volumes of 5 µL peptide solution (sample shares of 20%) were injected onto a 75 µm × 2 cm trapping column (Acclaim PepMap RSLC, Dionex) at 4 µL/min for 5.75 min. Peptide separation was performed at 50°C with a flow rate of 175 nL/min on a 50 µm × 50 cm separation column (Acclaim PepMap RSLC, Dionex) applying a gradient ranging from 2.4 to 32.0% of ACN over the course of 140 min. Eluted peptides were ionized by nanospray ionization and analyzed in the mass spectrometer implementing a top 5 collision induced dissociation (CID) method generating fragment spectra for the five most abundant precursor ions in the survey scans. For HLA class I ligands, the

mass range was limited to 400–650 m/z with charge states 2+ and 3+ selected for fragmentation and the resolution was set to 60,000.

2.2.36 Database search and spectral annotation

Data was processed against the LNZ308 proteome derived from RNA sequencing and the oncolytic measles virus proteome (UniProt) applying the SequestHT algorithm[53] in the Proteome Discoverer 1.3 (Thermo Fisher Scientific) software. Precursor mass tolerance was set to 5 ppm, fragment mass tolerance was set to 0.5 Da and oxidized methionine was allowed as a dynamic modification. Percolator[54] assisted FDR calculation was set at a target value of q ≤ 0.05 (5% FDR). Peptide spectrum matches with q≤ 0.05 were filtered according to additional orthogonal parameters to ensure spectral quality and validity. Peptide lengths were limited to 8–12 aa. HLA annotation was performed using NetMHCpan-3.0[55] based on the HLA class I typing of LNZ308 [56].

2.2.37 Analysis of LNZ308 ligandomes in different conditions

For label-free quantification of the relative HLA ligand abundances under the different conditions (CT, CT-VT, CT-VT-RT, VT and RT), the injected peptide amounts of paired samples were normalized and LC-MS/MS analysis was performed in five technical replicates for each sample [51]. In brief, relative amounts of substance of paired samples were calculated from average precursor ion intensities determined in dose-finding mass spectrometry runs and adjusted accordingly by dilution. Relative quantification of HLA ligands was performed by calculating the area under the curve of the corresponding precursor extracted ion chromatograms using Proteome Discoverer 1.3. The ratios of the mean areas of the individual peptides in the five label-free quantification-MS runs of each sample were calculated and two-tailed t tests were performed using an in-house Matlab script (v8.2, MathWorks, Natick, USA).

2.2.38 Peptide synthesis

The automated peptide synthesizer Liberty Blue (CEM, Kamp-Lintfort, Germany) was used to synthesize peptides using 9-fluorenylmethyl-oxycarbonyl/tert-butyl (Fmoc/tBu) strategy. The identity and purity of peptides were validated by reversed-phase liquid chromatography (nanoUHPLC, UltiMate 3000 RSLCnano, Dionex) and on-line coupled LTQ Orbitrap XL hybrid mass spectrometer (Thermo Fisher Scientific) system. Synthesized peptide was used in the validation of LC-MS/MS identification as well as in functional experiments.

2.2.39 T-cell culture

Blood samples of healthy donors were kindly provided by the Institute for Clinical and Experimental Transfusion Medicine at the University Hospital Tübingen after obtaining written

informed consent. Peripheral blood mononuclear cells (PBMCs) were isolated by standard Ficoll-Hypaque (Biocoll, Biochrom, Berlin, Germany) density gradient centrifugation. Cells were stored at -80°C in FCS (Sigma Aldrich) and 10% DMSO (Merck, Whitehouse Station, New Jersey, USA). After thawing, the cells were rested overnight prior to stimulation with culture conditions of 37°C and 7.5% CO_2 in humidified incubators.

2.2.40 IFNγ enzyme linked immunospot (ELISPOT) Assay

The IFNγ ELISpot assay after 12 day stimulation was performed as described previously [57]. Briefly, 24 h after thawing, cells were stimulated with 1 µg/ml candidate measles viral peptide or control peptides. IL 2 (R&D Systems) was added on day 2, 5 and 7 with a final concentration of 20 U/ml and 1000 U/ml for PBMCs of healthy donors and TILs, respectively. On day 12, cells were harvested and IFNγ ELISpot was performed. Phytohaemagglutinin (PHA, Sigma Aldrich), the HLA-A*24:02 restricted epitope TYPVLEEMF (EBV BRLF1198-206) or a pool of 18 viral peptides of different HLA restrictions was used as positive control. HLA-A*24:02 restricted peptide KYPENFFLL (HUMAN PP1G113-121) or medium alone served as negative control. Spot counts were determined using an ImmunoSpot S6 Analyzer (CTL, Shaker Heights, Ohio, USA) with T cell responses considered to be positive if the mean number of spots per well was at least ten and more than three times the mean number of spots of the negative control.

2.2.41 TCGA dataset analysis

We downloaded the gene expression RNASeq data of LGGs and GBMs (Illumina) and the associated clinical data from the NIH National Cancer Institute GDC portal (https://portal.gdc.cancer.gov) released by TCGA. The survival data from TCGA were merged with gene expression data and other associated clinical information using corresponding sample ID.

2.2.42 Statistical analyses

Statistical significance were calculated using two-way ANOVA followed by Tukey's multiple comparison test, one-way ANOVA with Dunnett's multiple comparison test or with multiple t-test as suitable. All values are expressed as mean ± standard error of the mean (SEM).

Results

3.1 GFP expression visualized upon successful transduction of glioma cells with 3rd generation lentivirus pSIN_GFP

The 3rd generation lentiviral vector, pSIN_GFP was produced and concentrated using standard ultracentrifugation procedures with calculated viral titer of 1.3×10^8 IU/mL (Fig. 6a and 6b) using flow cytometric analysis. Long term glioma cell lines, LN229 and LNZ308 were transduced using pSIN_GFP at 10 MOI and verified for expression of GFP (Fig. 6c) through fluorescence microscopy.

a

b

c

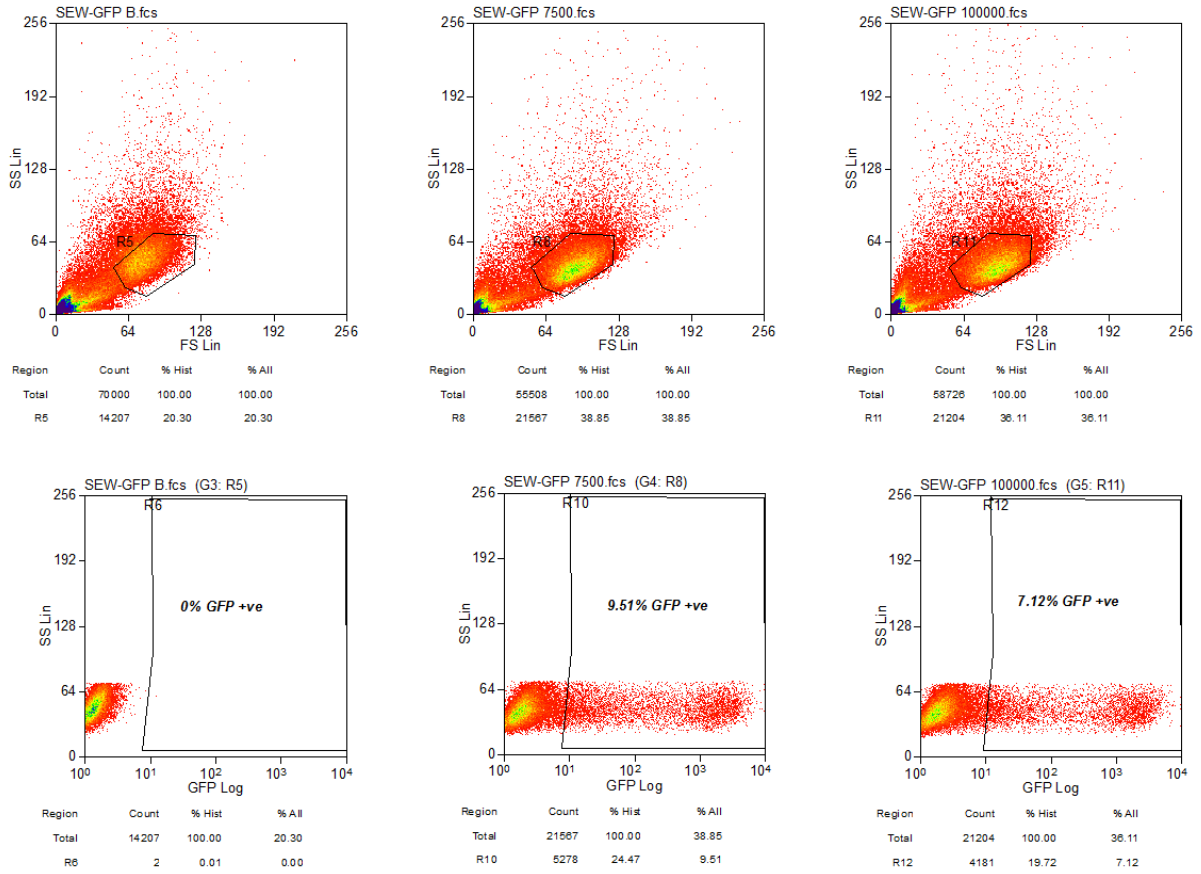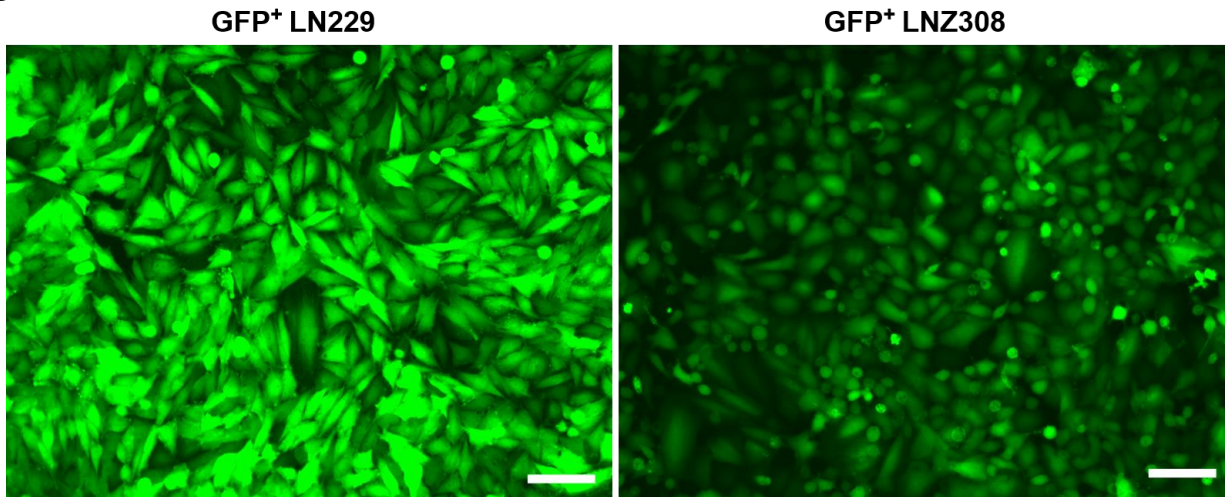GFP⁺ LN229　　　　　GFP⁺ LNZ308
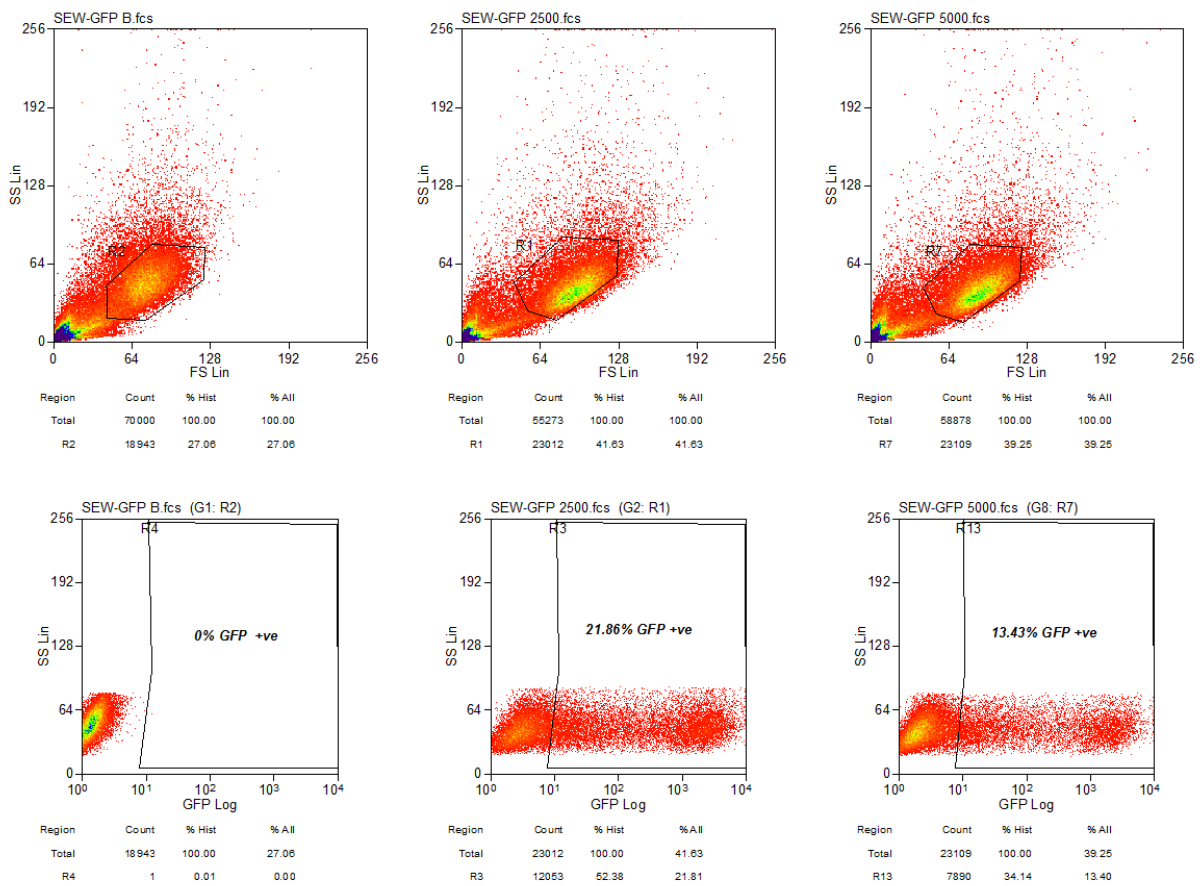
*Figure 6. Generation of GFP⁺ glioma cells. a - b, Flow cytometric analysis of GFP expression in pSIN_GFP lentiviral transduced cells used for viral titer determination. **c,** Glioma cell lines, LN229 and LNZ308 successfully transduced to express GFP. Scale bar = 100 µm. Abbreviations: GFP, green fluorescent protein.*

3.2 CD46 receptor is expressed on glioma cells, glioma stem-like cells and primary glioblastoma cell lines

Membrane cofactor protein (MCP) or CD46 serves as the receptor for the entry of the vaccine strain of measles virus [58], expressed in all human nucleated cells but frequently upregulated in tumors including GBM, breast cancer, etc, [59,60]. We characterized the different glioma cell lines for CD46 expression via flow cytometric analysis with high expression observed in long term glioma cell lines LNZ308 and LN229 (Fig. 7a). Glioma stem-like cells GS3 and GS8 showed comparably lower, but clearly detectable CD46 expression with levels similar to the primary glioblastoma cells T81/16, T708/16 and T1094/17 (Fig. 7a). Isolated HPCs showed high levels of CD46 expression similar to LN229 (Fig. 7a), supporting the feasibility of employing them as viral cellular carriers. Moreover, all long term glioma cell lines were checked for basal Nectin-4 expression, an alternative MeV entry receptor expressed in respiratory epithelium but also in breast cancer and ovarian cancer [61-63]. The glioma cells did not express Nectin-4 (Fig. 7b), however low level of expression was observed with positive control HT29 cells. Despite differing levels of CD46 expression, viral infectivity visualized by GFP expression showed characteristic 'syncytia' formation in all cell lines using fluorescence microscopy (Fig. 7c).

a Basal CD46 expression

b Basal Nectin-4 expression
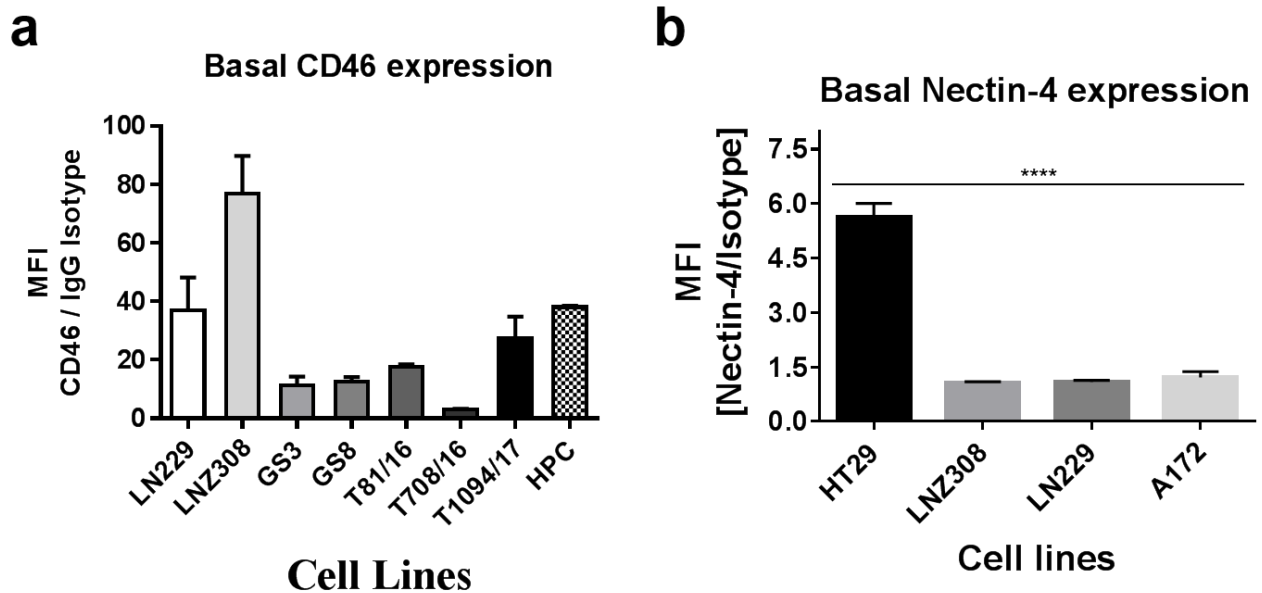
c
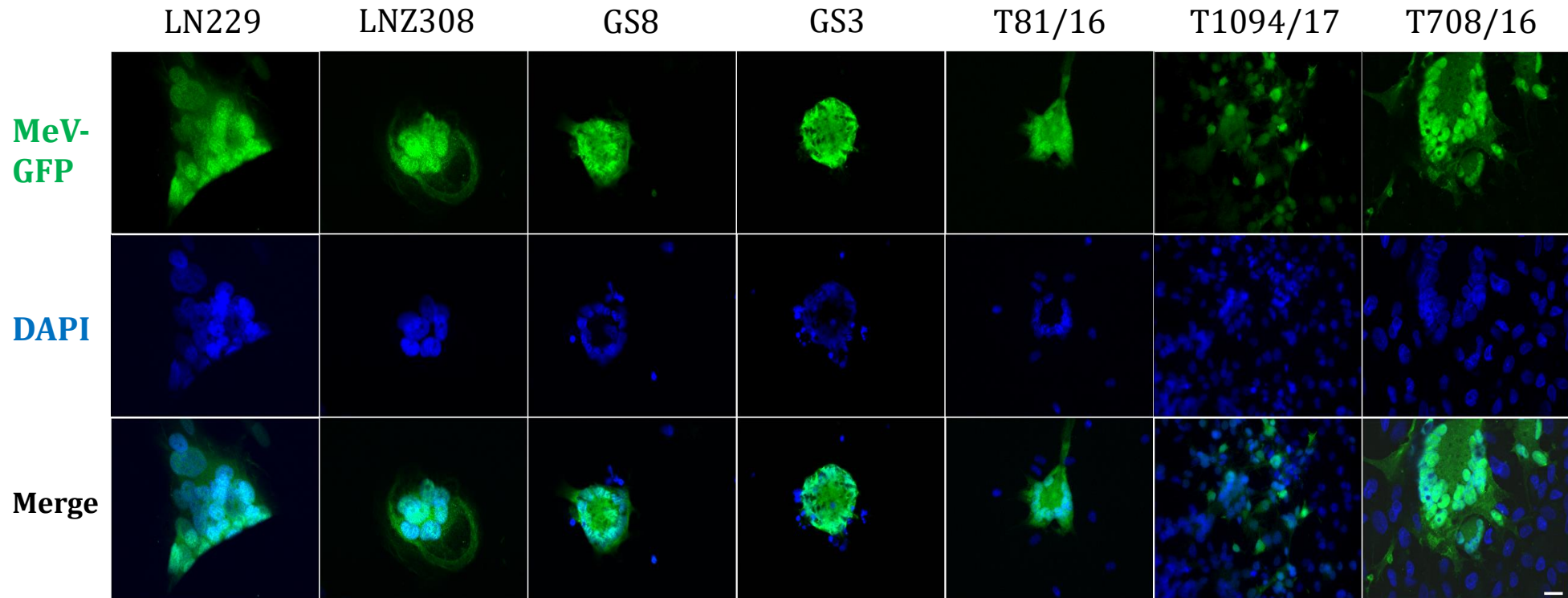
Figure 7. MeV infectivity characterized through CD46 receptor expression. a, Basal level of human CD46 receptor expression determined by flow cytometry using CD46-PE antibody in glioma cell lines, HPCs and primary glioblastoma cells. **b,** Glioma cell lines LN229, LNZ308 and A172 did not express Nectin-4 as analysed via flow cytometry along with positive control HT29 cells. **c,** MeV infectivity observed through GFP expression with characteristic syncytial morphology visualized as giant multinuclear aggregates. **a - b,** Data expressed as Mean ± SEM, n = 3. **c,** Scale bar = 20 μm.

3.3 Modification of CD46 receptor expression in LNZ308 by hypoxia and temozolomide but not by irradiation

We next assessed CD46 expression in LN229 and LNZ308 after culturing at 1% O_2 or treatments with irradiation or TMZ (Figs. 8a - c). The expression of CD46 expression increased in LNZ308 after culturing in hypoxia (Fig. 8a) but remained unchanged in LN229. The DNA double strand break inducing radiotherapy (RT) [64] did not affect CD46 expression in both the cell lines (Fig. 8b) while no change was observed in LN229 post treatment with TMZ (Fig. 8c). Low doses of temozolomide, 10 µM and 100 µM, significantly increased CD46 expression (Fig. 8c) in LNZ308. However, we observed a significant decline when treated with 1000 µM in LNZ308 (Fig. 8c) implicating the cytotoxic nature with high dosage of TMZ.
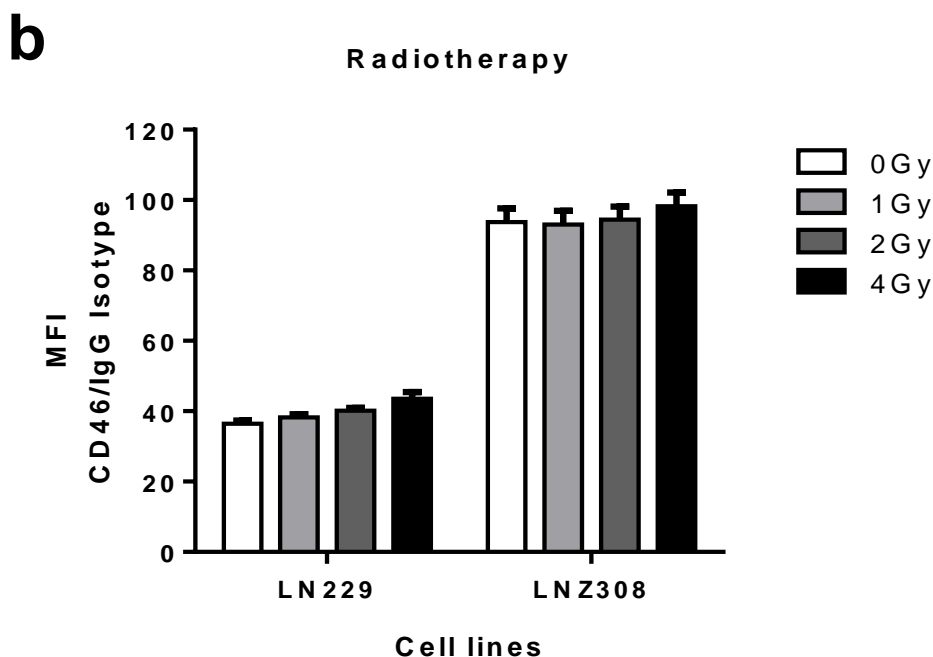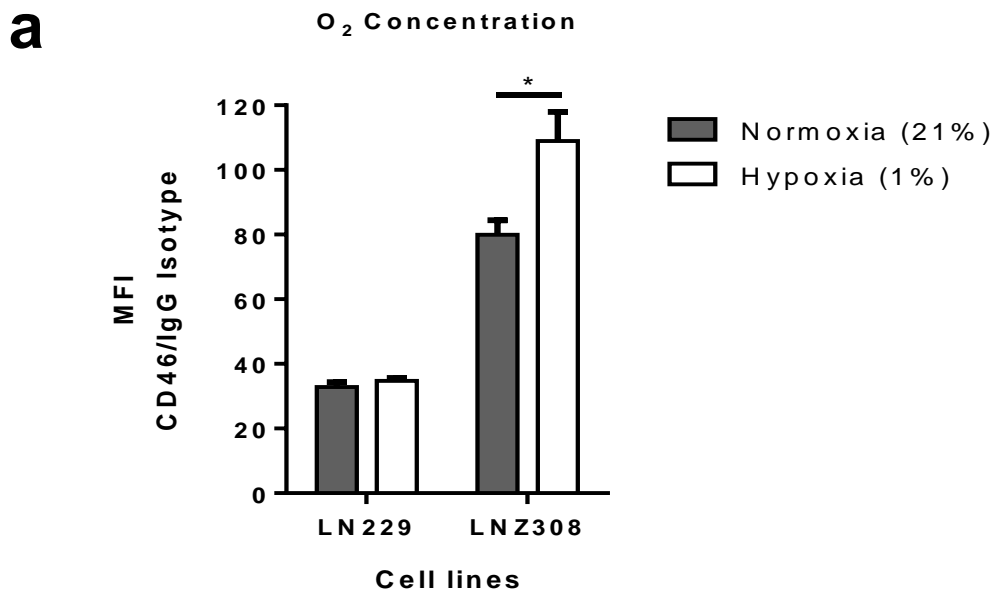
C

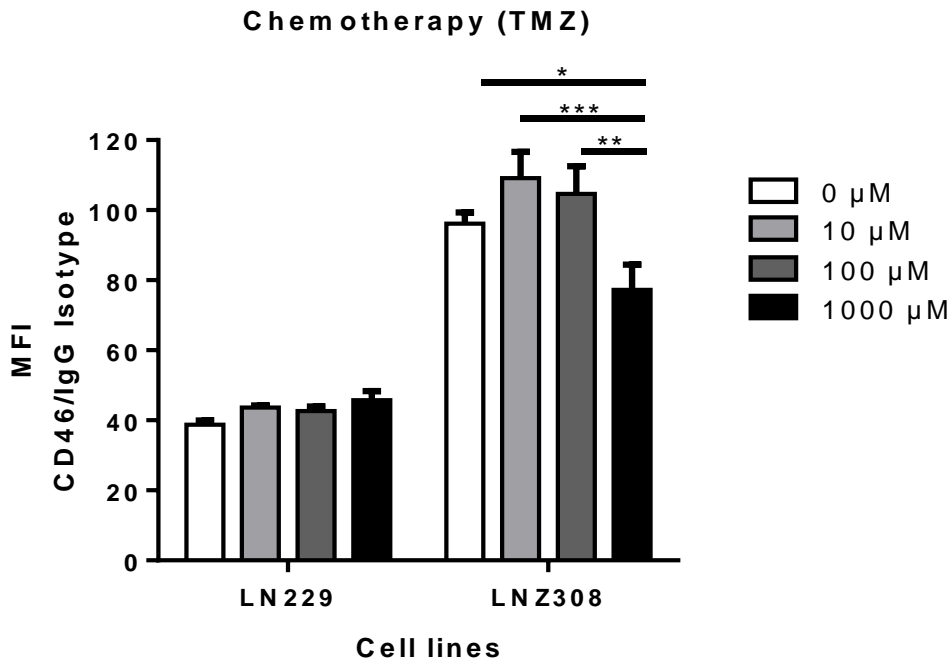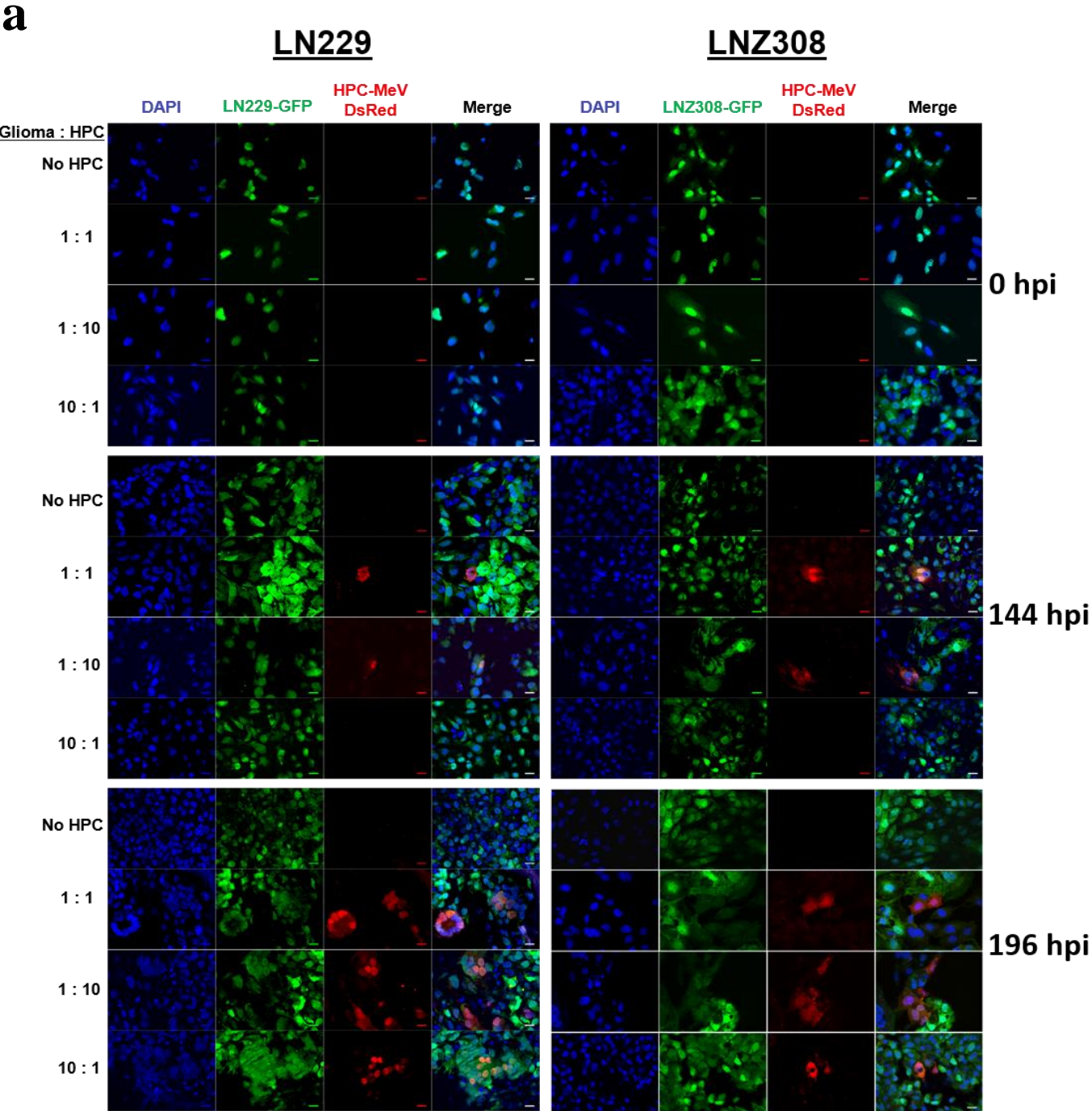Figure 8. CD46 expression in LNZ308 is affected upon hypoxia and temozolomide. a, Significant increase in CD46 surface expression on LNZ308 cells subjected to hypoxia with no effect of hypoxia in LN229 cells. b, No change in CD46 expression after γ-irradiation of LN229 or LNZ308 cells. c, Low dose (10 μM, 100 μM) TMZ increases CD46 surface expression while high dose of TMZ (1000 μM) impairs CD46 expression in LNZ308 cells. a - c, Data expressed as Mean ± SEM, n = 9. Multiple t-test with Holm-Sidak post hoc test in a; Two-way ANOVA with Tukey's multiple comparison test in b, c; *, p < 0.05; **, p < 0.01; ***, p < 0.001.

3.4 HPC's deliver measles virus to glioma cells in a payload and CD46 expression dependent manner

We have shown previously that HPC's home towards gliomas due to intrinsic chemokine signalling such as CXCL12-CXCR4, stem cell factor (SCF)-CD117 and this further exacerbated through stress factors including irradiation, TMZ chemotherapy and hypoxia [65-67]. We co-cultured GFP⁺ LN229 and GFP⁺ LNZ308 cells with HPC's transduced with MeV-DsRed at different ratios of glioma cells to HPC's over time (0 hpi to 192 hpi) to observe viral infectivity through DsRed expression and syncytial morphology of cells (Fig. 9a). The highest infectivity was observed in 1:10 ratio as expected in both cell lines and earliest DsRed expression in LNZ308 at 96 hours post infection (hpi) in the 1:10 ratio explained by their high CD46 receptor levels augmenting viral entry. However, DsRed expression was quite evident in both LN229 and LNZ308 cells in the 1:1 and 1:10 ratios at 144 hpi (Fig. 9a) substantiating the viral load dependent effect as observed by lack of signal from the 10:1 ratio. Viral infectivity was observed in all transduced cells at 192 hpi accompanied with bright syncytial DsRed

expression. The low cell viability along with syncytial morphology observed in both the cell lines at 192 hpi in the 1:1 and 1:10 ratios (Figs. 9b and 9c) indicate successful delivery of MeV by the HPC's with subsequent viral proliferation leading to an oncolytic cascade and eventual tumor cell lysis *in vitro*.

b

	DAPI	LN229-GFP	HPC-MeV DsRed	Merge
Glioma cell : HPC				
No HPC				
1 : 1				
1 : 10				
10 : 1				

c

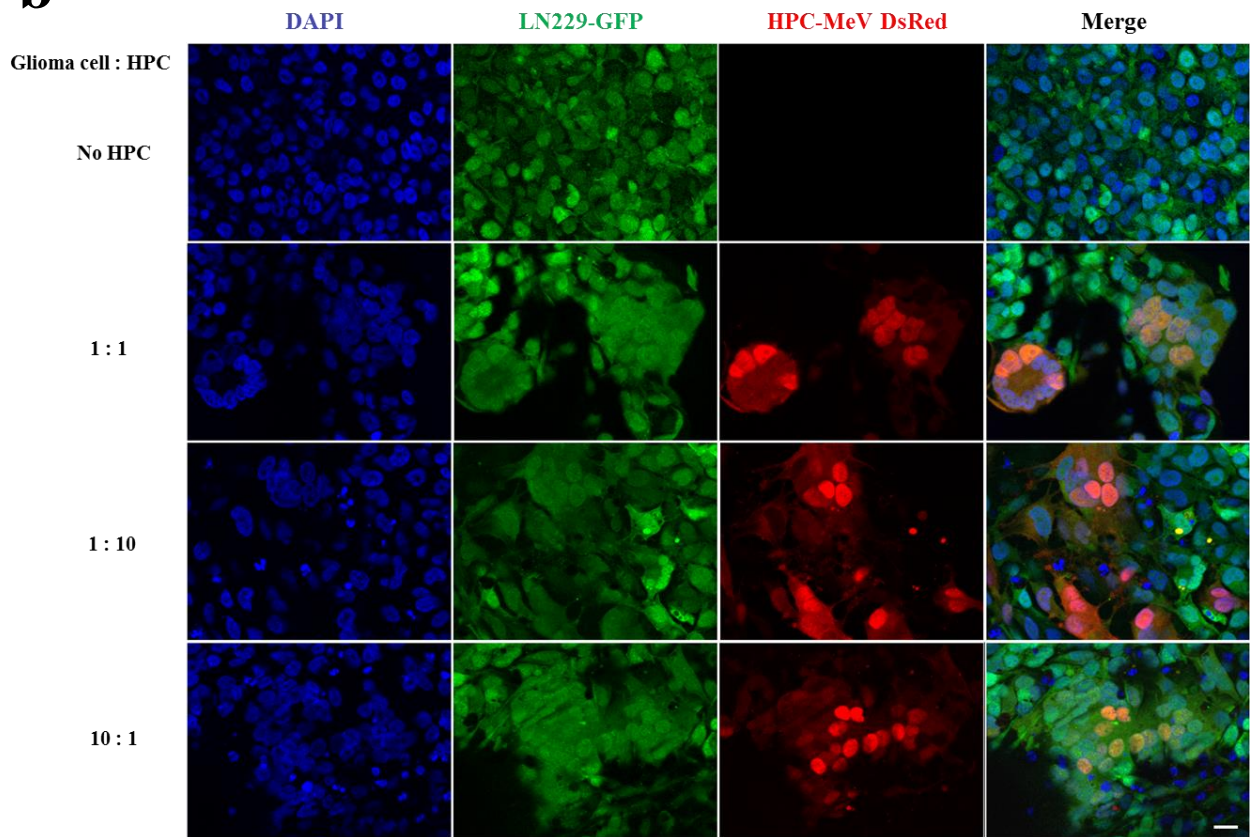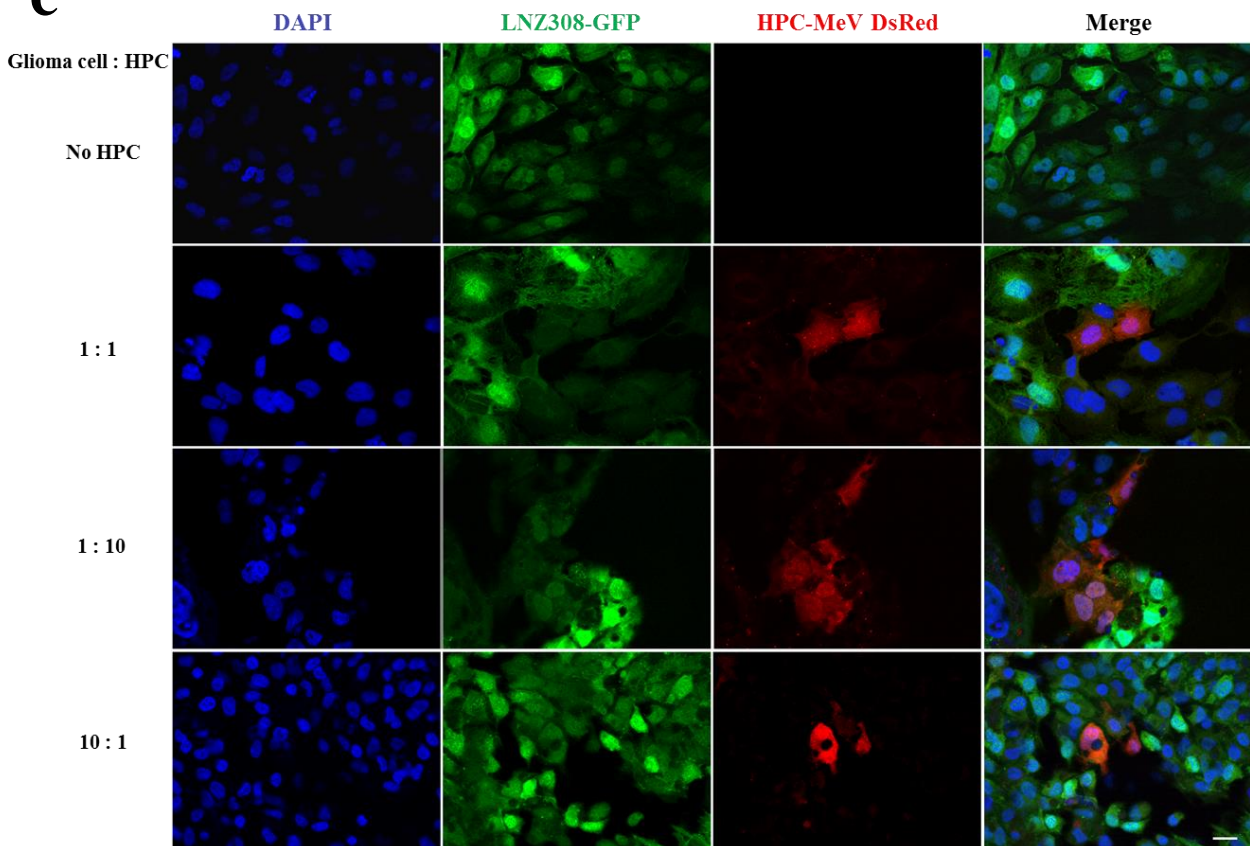|	DAPI	LNZ308-GFP	HPC-MeV DsRed	Merge
Glioma cell : HPC				
No HPC				
1 : 1				
1 : 10				
10 : 1				

Figure 9. Co-culture of MeV-DsRed transduced HPCs with GFP⁺ glioma cells. *Successful cell based delivery of measles virus in GFP⁺ glioma cells co-cultured with MeV-DsRed transduced HPCs over 192 hpi. **a,** Time course analysis of co-culture with early DsRed expression observed at 144hpi in 1:1 and 1:10 ratios in both cell lines. All ratios containing transduced HPCs showed DsRed expression at 192 hpi. **b,** Enlarged picture of LN229 co-culture at 192 hpi. Syncytial multinuclear aggregates visualized in GFP⁺ LN229 with a pronounced morphology in 1:10 ratio when compared to 1:0 (no HPCs). **c,** Enlarged picture of LNZ308 co-culture at 192 hpi. Oncolytic cascade effect of MeV-DsRed observed in GFP⁺ LNZ308 visualized by fewer cell numbers in 1:10 ratio suggesting reciprocity between high CD46 expression and enhanced MeV infectivity.*

3.5 Measles virus infection initiates and sustains autophagy

Measles virus has been shown to induce autophagy, including mitophagy to sustain an anti-apoptotic environment through prevention of cytochrome-C thereby enhancing its replicative potential [68-70]. We observed conversion of soluble LC3-I to lipid bound LC-II, the hallmark of autophagy, in LNZ308 cells infected with MeV-DsRed as early as 12 hpi and we observed more conversion in the 0.1 MOI than 0.5 MOI (Fig. 10a). This was further supported by basal level of LC3 observed in untreated Blank and after RT in both 2 Gy and 4 Gy implicating a clear MeV infection associated increase in LC3 conversion. Moreover, a similar effect was recapitulated with fluorescence microscopy by using a GFP-tagged LC3 (LC3-GFP) as observed by GFP puncta at 48 hpi (Fig. 10b). The autophagic flux initiated by MeV was verified in primary glioblastoma cell, T1094/17 with brighter GFP puncta observed at 0.1 MOI (Fig. 10b) along with viral spread and syncytial morphology viewed through DsRed expression. Importantly, we observed that the LC3-tagged GFP signal was minimal and more nuclear in LNZ308 after RT indicating the lack of autophagic activity.
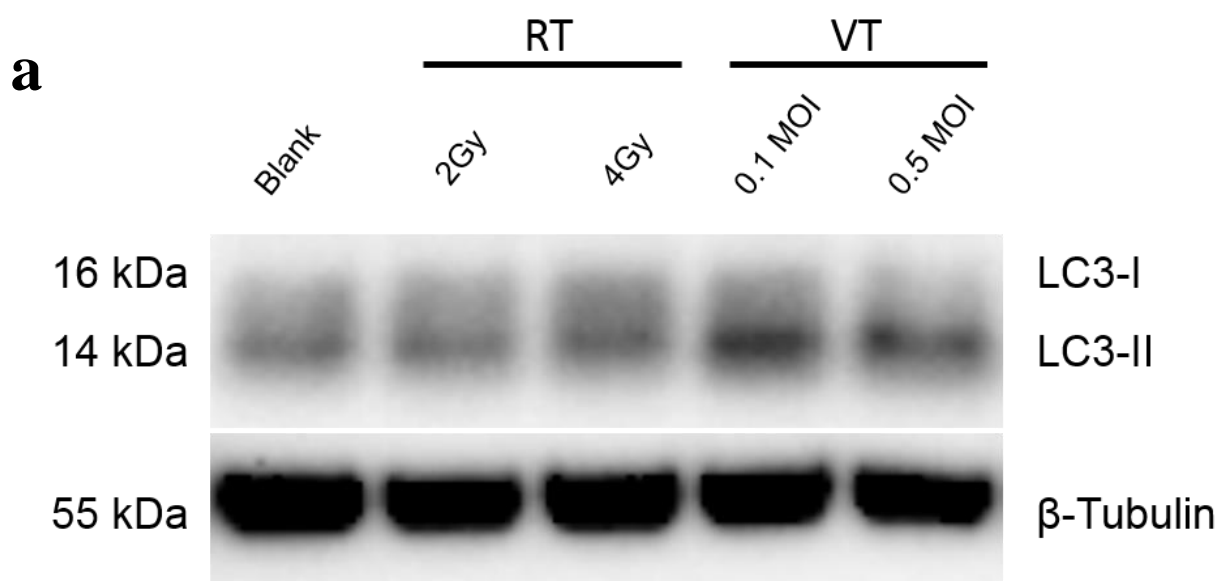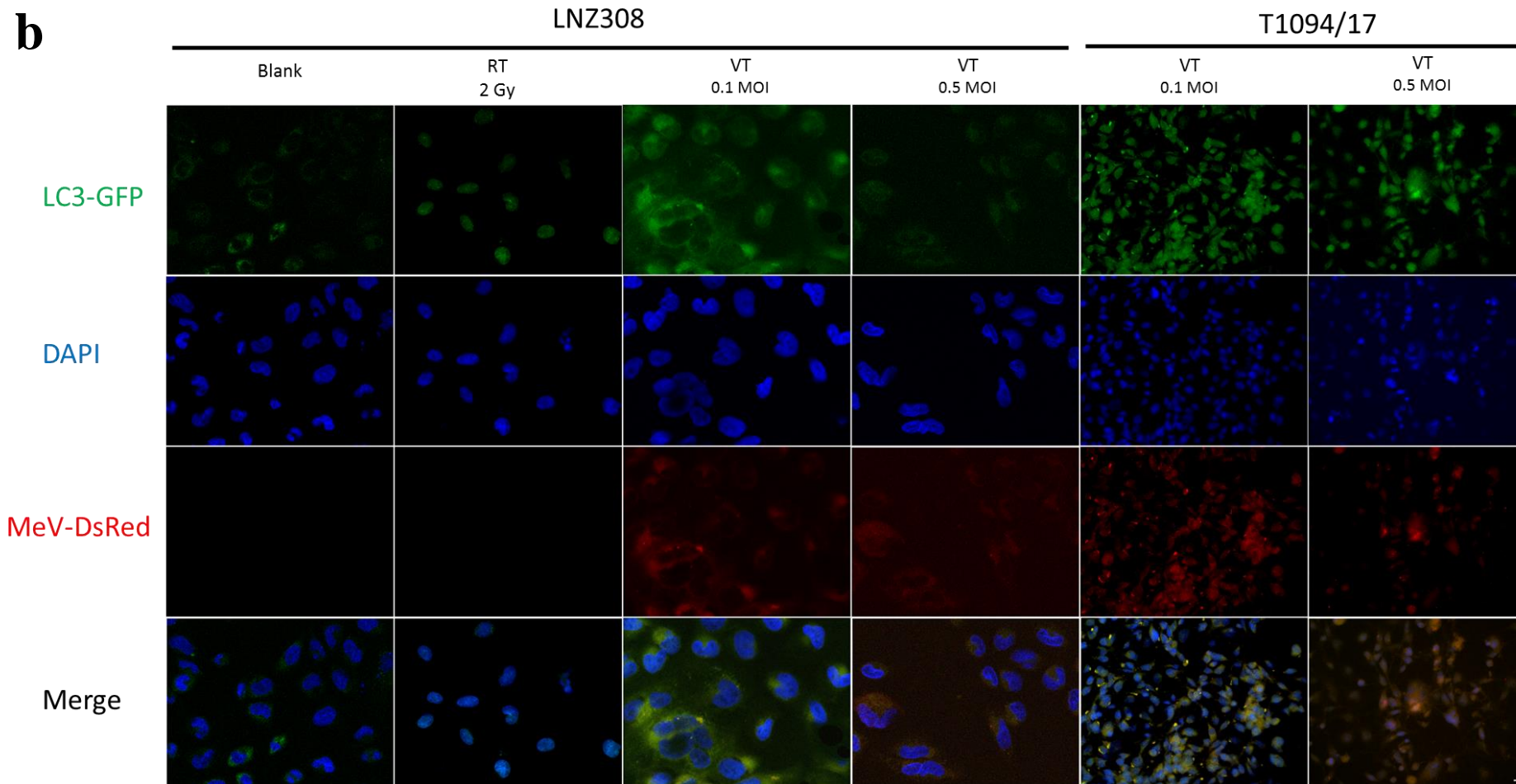
Figure 10. MeV infectivity induces autophagy in glioma cells. a, *Increased conversion of LC3-I to LC3-II (upper panel) in VT treated samples as opposed to basal level of LC3 expression in Blank and RT treated cells. β-tubulin was used as loading control (lower panel).* **b,** *Measles viral infection initiates autophagy as observed through GFP tagged LC3 expression in LNZ308 and primary GBM T1094/17 while minimal basal nuclear LC3 signal noticed in Blank and γ-irradiated cells.*

3.6 Combined treatments of virotherapy and radiation therapy are only synergistic when radiation therapy is administered after virotherapy

Due to its relevance to the current clinical scenario we combined virotherapy (VT) with radiotherapy (RT) and alkylating chemotherapy (CT) to identify a chronological synergistic regimen elicited by such a treatment strategy. The induction of autophagy including mitophagy upon MeV infection prevents release of cytochrome-C thereby inhibiting apoptosis. This suggests that, initiation of treatment with irradiation, an established apoptosis inducer [71,72], will likely lead to an antagonistic "antiviral" effect when followed by virotherapy. This was confirmed through acute cytotoxicity assays with VT and RT performed in three sequential regimens in LN229 cells (Figs. 11a - c): RT followed by VT (RT-VT), VT followed by RT (VT-RT) and simultaneous treatments (Sim Trt). The treatment regimen initiated with virotherapy followed by irradiation (VT-RT) showed significantly lower cell viability than the other regimens (Fig. 11a) in accordance with previous results [73]. Sim Trt with virus and irradiation displayed higher cell survival than VT-RT but with a better dose dependent response than RT-VT (Fig. 11b). Moreover, in our setting RT-VT exhibited an antagonistic effect with higher cell survival despite increasing doses of virus and radiation indicating an unfavourable role of irradiation to viral proliferation when treated first (Fig. 11c). The adverse effects of RT on MeV was distinct in cells treated with 4 Gy irradiation wherein, cell viability was lower in absence of MeV (0 MOI) than with 0.01 MOI. Consequently, we incorporated alkylating chemotherapy (CT) to the current treatments such that virotherapy always precedes radiotherapy, leading to three possible combination regimens: (i) virotherapy → radiotherapy → temozolomide (VT-RT-CT) (ii) virotherapy → temozolomide → radiotherapy (VT-CT-RT) and (iii) temozolomide →
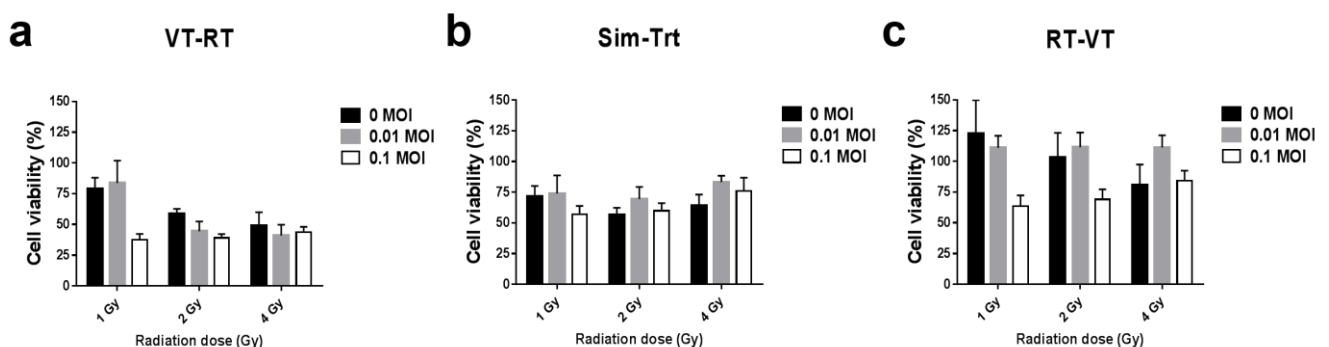
virotherapy → radiotherapy (CT-VT-RT).

Figure 11. Virotherapy followed by irradiation (VT-RT) is highly cytotoxic over other regimens in LN229. a, Cell viability post VT-RT was least thereby elucidating its synergistic potency. b, Simultaneous treatment of MeV with irradiation c, The sequential regimen RT-VT showed poor

combinatorial efficacy with increasing doses of radiation and virus. Black, grey and white bars indicate viral doses in MOI. Data expressed as Mean ± SEM, n = 6.

3.7 Triple therapies including virotherapy, radiotherapy and chemotherapy are synergistic if the treatment algorithm starts with chemotherapy and is followed by virotherapy and finally radiotherapy

We carried out cytotoxic survival assays in glioma cell lines, LN229 and LNZ308 utilising TMZ in combination with VT and RT as monotherapies, dual or triple regimens. The cell viability observed post monotherapies were used to calculate the predictive values employing the Chou-Talalay fractional product method [74]. LN229 and LNZ308 cells were treated with temozolomide chemotherapy based on their EC_{50} values described previously [75] and administered doses of 0 µM, 10% EC_{50}, 50% EC_{50} and EC_{50}. Cells were treated with radiation doses of 0 Gy, 1 Gy, 2 Gy and 4 Gy while MeV was provided at doses of 0 MOI, 0.01 MOI and 0.05 MOI. The monotherapy with γ-irradiation and TMZ clearly revealed a dose-dependent response in both cell lines (Figs. 12a and 12c). LN229 had lower cell viability with increasing doses of radiation and temozolomide which could be due to the mutated but active p53 expression in comparison to the p53 null LNZ308 [76]. Conversely, lower cell viability was observed in LNZ308 upon virotherapy (Fig. 12b) wherein absence of viral gatekeeper p53 and increased expression of CD46 might potentially play key roles (Fig. 7a).
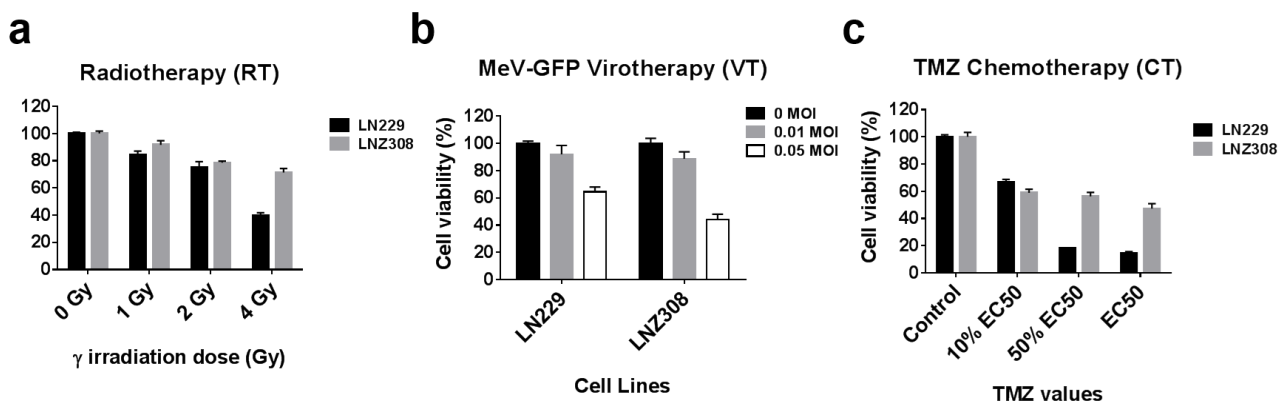
***Figure 12. Cytotoxic survival assay using temozolomide (TMZ) as an alkylating agent.** LN229 and LNZ308 cells were treated with monotherapies of **a,** γ-irradiation (RT), **b,** measles virotherapy (VT) and **c,** TMZ chemotherapy (CT). The cell viability post monotherapies were used to calculate predicted values of combinatorial treatment using fractional product method. Data expressed as Mean ± SEM, n = 9. Abbreviations: MOI, multiplicity of infection; EC_{50}, half maximal effective concentration.*

All triple regimens elicited a dose dependent effect with synergistic effects (indicated by red arrows) mainly observed in CT-VT-RT in both cell lines (Figs. 13a and 13b). The effect of virotherapy was prominent in CT-VT-RT with maximal cell death despite viral infection 12 h

later in comparison to VT-initiated regimens, VT-RT-CT and VT-CT-RT (Fig. 13). The treatment with double therapy, CT-VT (CT-VT-RT with RT = 0 Gy) can elicit synergy at low doses of 10% EC_{50} of TMZ in combination with 0.01 MOI and 0.05 MOI of MeV in both cell lines as does VT-CT. However, the synergy associated when combining TMZ with MeV is lost in VT-CT when applying 50% EC_{50} of TMZ in LN229. In contrast, the synergistic effect was sustained in CT-VT and a similar effect more evident with the highest dose of TMZ (EC_{50}) in both cell lines (Fig. 13). The additional cytotoxicity due to γ-irradiation was evident in VT-RT-CT treatment sequence, while found limited in both CT-VT-RT and VT-CT-RT, possibly due to delayed radiation treatment (12 h later). The dose-dependent effect of TMZ in the highest virus dose (0.05 MOI) and radiation dose (4 Gy) is lost in both cell lines in non-synergistic regimens, VT-CT-RT and VT-RT-CT (Figs. 13c - f). In contrast, dose-dependent decline in cell viability was sustained in CT-VT-RT, although an additive rather than a synergistic effect became evident here.

The simplistic visualization of our combinatorial treatments as Chou-Talalay coefficients (observed/predicted cell viability) reveal identical treatment dependent effects with values below the red line implying synergy (Fig. 14). The cytotoxicity of triple regimens were reflected, with lower coefficient values in CT-VT-RT (Figs. 14a and 14b) and high coefficients with increasing doses of treatments in VT-initiated triple regimen (Figs. 14c - f) clearly indicating here that, the observed cell viability was higher than predicted combination. Moreover, the synergy coefficient distinctly proves the combinatorial efficacy of CT-VT-RT with more values < 1 (Figs. 14a and 14b) while VT-initiated regimen primarily exhibited additive (=1) and antagonistic (>1) effects (Figs. 14c - f). Furthermore, as seen previously, RT at 4 Gy resulted in loss of synergy and an additive effect was seen in CT-VT-RT in both cell lines, (Figs. 14a and 14b) while the extreme antagonistic values in VT-initiated regimen suggest that observed cell viability was very high, particularly in LN229 (Figs. 14c and 14e).

The ultimate goal for synergistic treatments with combination of agents is to elicit maximal therapeutic effect with minimal toxic doses in patients. Given the clinical routine for treatment of glioblastoma with fractionated individual doses up to 2 Gy irradiation, we identified CT-VT-RT as the only regimen to exhibit a synergistic effect at 2 Gy in both LN229 and LNZ308 at 10% EC_{50} and 50% EC_{50} of TMZ along with 0.05 MOI of MeV-GFP (Figs. 13a and 13b). The pronounced oncolytic effect observed in the most synergistic regimen initiated with chemotherapy over the VT-initiated triple regimen suggests that initial TMZ treatment established an environment conducive for viral proliferation. The observed increase in CD46 receptor expression subjected to low doses of TMZ (Fig. 8c) through flow cytometric analysis might be one factor in augmenting viral infectivity.
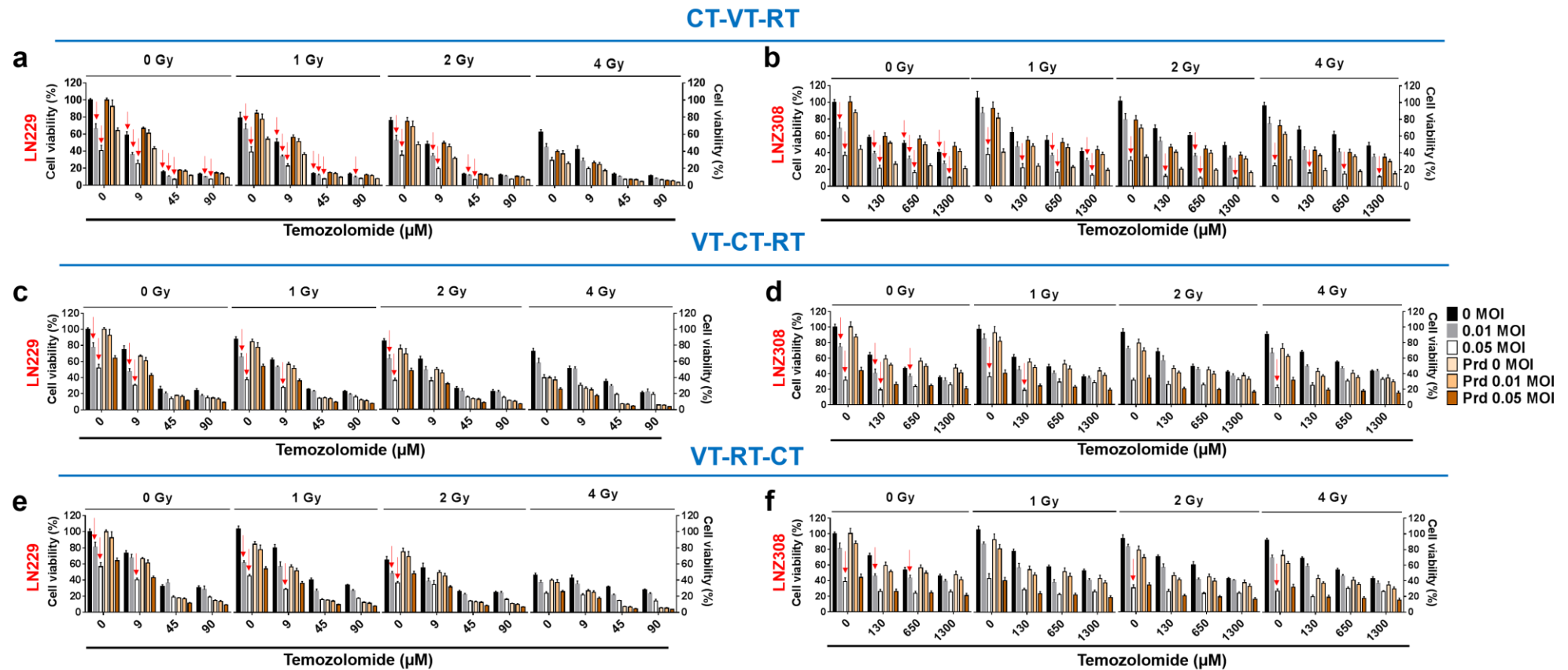
***Figure 13. CT-VT-RT exhibited synergy while using Temozolomide as chemotherapeutic agent (a)** in LN229 and **(b)** LNZ308 cells respectively. Non-synergistic regimen VT-CT-RT showed poor combinatorial efficacy in **(c)** LN229 and **(d)** LNZ308. Non-synergistic regimen VT-RT-CT with poor combinatorial efficacy in **(e)** LN229 despite stronger radiation dose dependent effect and **(f)** also in LNZ308. Red arrows indicate synergy realized in observed cell viability when compared to predictive values of co-treatments. Black, grey and white bars indicate observed values; Orange, brown bars indicate calculated predictive values from individual monotherapies (RT, VT, CT). Data expressed as Mean ± SEM, n = 9. Abbreviations: Prd, predicted; MOI, multiplicity of infection.*
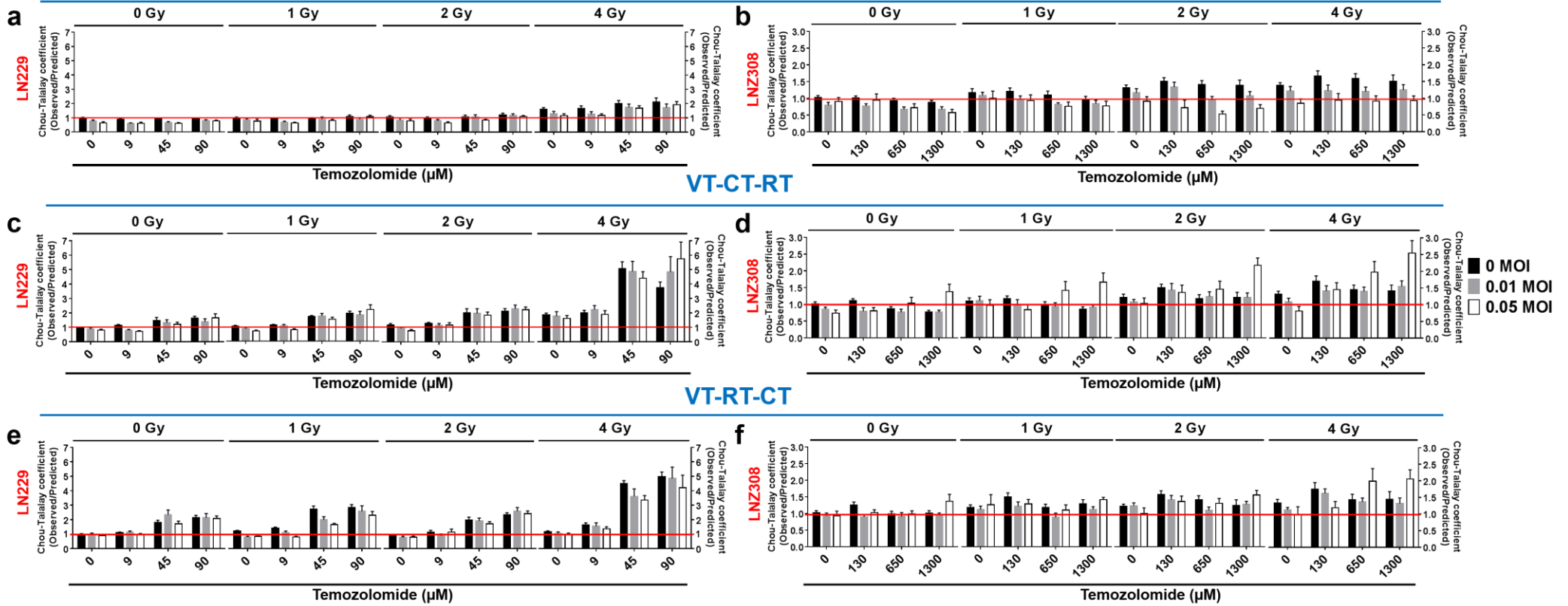
Figure 14. Triple regimen using TMZ as alkylating agent expressed as Chou-Talalay coefficients (ratio of observed/predicted cell viability). The red line indicates coefficient of 1 which allows for determination of synergy (when < 1), additivity (when =1) and antagonism (when > 1) upon combination of therapeutic agents. CT-VT-RT elicited maximal synergy in both *(a)* LN229 and *(b)* LNZ308. VT-initiated regimens showed non-synergistic activity in both LN229 and LNZ308 respectively in *(c, d)* VT-CT-RT and *(e, f)* VT-RT-CT. Black, grey and white bars indicate viral doses.

49

3.8 CT-VT-RT effected synergy in glioma stem-like cell, GS8

We determined the EC_{50} of TMZ in GS8 to be 250 µM (Fig. 15) using acute cytotoxicity assays as described. Employing selective doses identified synergistic in LN229 and LNZ308 we performed cytotoxic survival assays with 2 Gy irradiation, 0.05 MOI of MeV and 10% EC_{50} of TMZ in previously established combinations. Unlike the long-term glioma cells, we observed no effect in GS8 cells treated with 25 µM of TMZ but observed a significant cytotoxicity associated with 2 Gy irradiation and 0.05 MOI of virus when performed as monotherapies (Fig. 16a). The therapy-initiating dual regimens of CT-VT (CT-VT-RT when RT= 0 Gy, (Fig. 16b)) did not elicit combinatorial efficacy but VT-CT (VT-CT-RT when RT= 0 Gy, (Fig. 16c)) and VT-RT (VT-RT-CT when CT= 0 µM, (Fig. 16d)) were identified synergistic. The early administration of MeV in the VT-initiated regimens potentially aids in synergy as opposed to non-effectual dosage of TMZ in CT-VT. As previously observed, combination of RT and VT doses showed synergy as double regimens in CT-VT-RT (when CT= 0 µM) and VT-RT-CT (when CT= 0 µM) but not in VT-CT-RT (when CT= 0 µM). Furthermore, addition of TMZ to VT and RT regimens effected synergy only in CT-VT-RT (Fig. 16b) and despite, observed synergy in double regimen, VT-RT-CT only elicited an additive effect (Fig. 16c) as a triple regimen. This further proves the combinatorial efficacy of our synergistic triple regimen in an alternate glioma stem-like cell line.

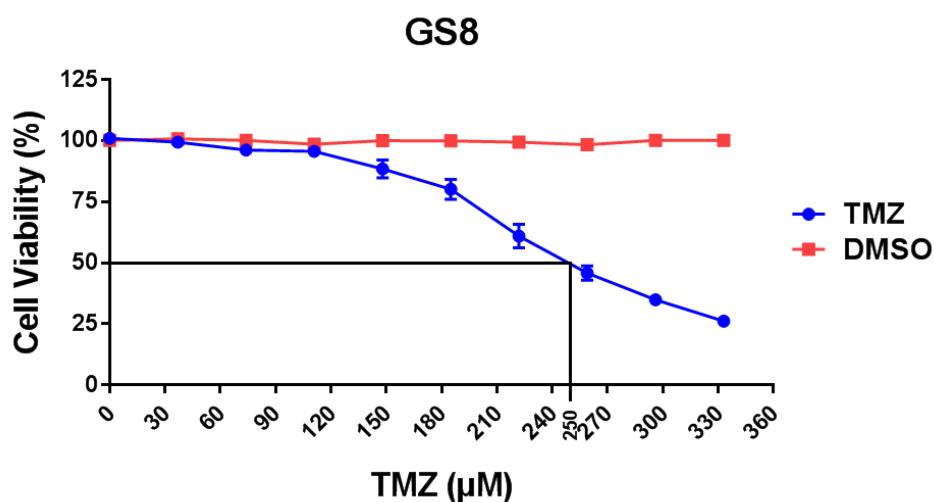
Figure 15. Determination of EC_{50} value for TMZ in GS8 cells. *The EC_{50} for GS8 was identified to be 250 µM when carried out with respective DMSO controls. TMZ and DMSO are depicted by blue and red dose-response curves respectively.*
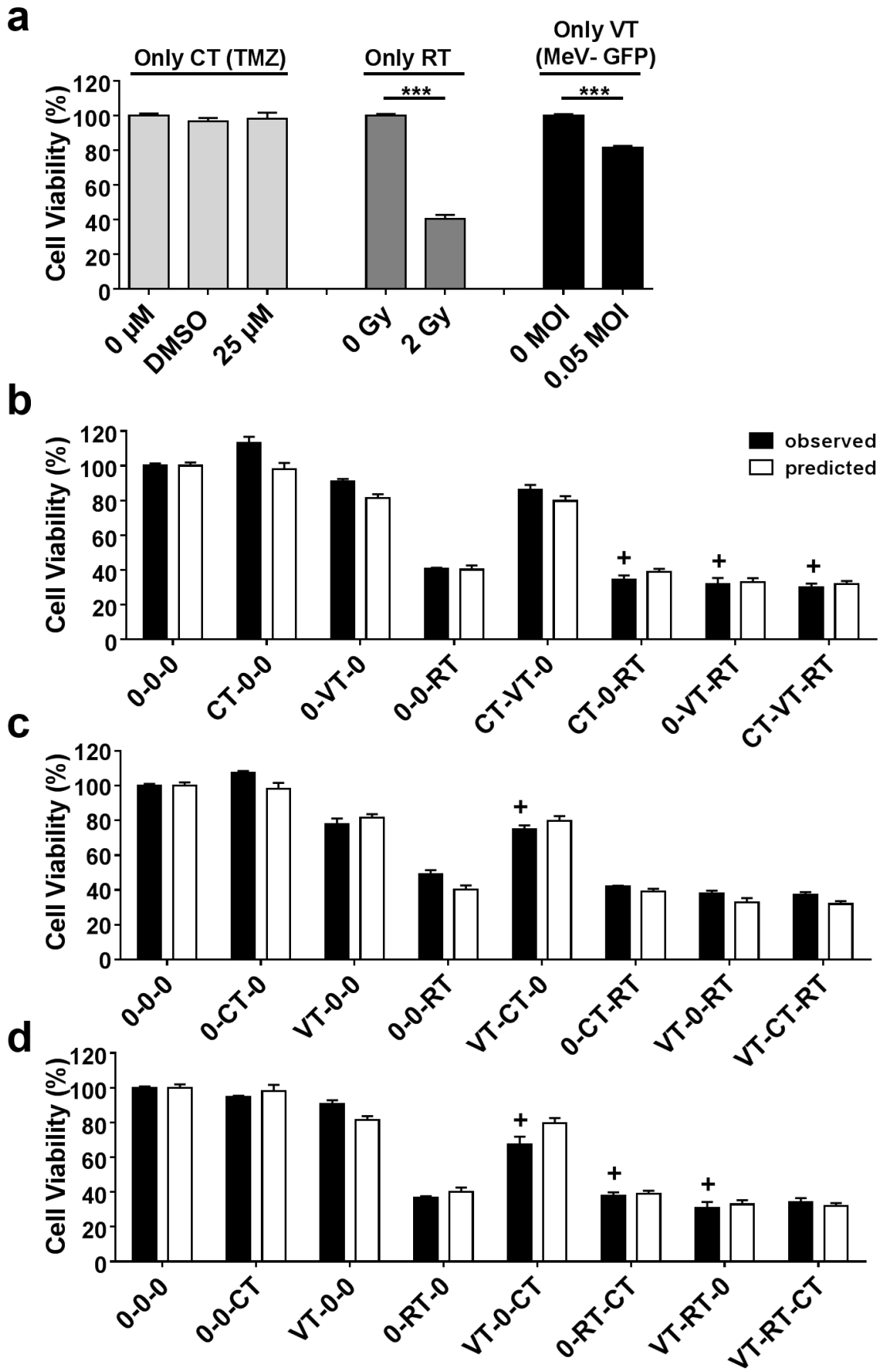
Figure 16. Cytotoxic survival assay in GS8 using TMZ as the alkylating agent. a, Monotherapies with TMZ (CT), γ-irradiation (RT) and measles virotherapy (VT). b - d, Black bars indicate observed values and white bars indicate calculated predicted values in the triple regimens. Triple regimens carried out with 0 indicate absence of treatment (0 Gy, 0 MOI or 0 µM) while CT = 25 µM, VT = 0.05 MOI, RT = 2 Gy as performed chronologically in that regimen. For example: CT-0-RT, the VT was carried out with 0 MOI while CT was 25 µM and RT with 2 Gy. Similarly, position of treatment is indicated in accordance with chronology within each regimen as in VT-0-0 indicates regimen initiated with VT while 0-VT-0 suggest virotherapy performed 12 h after first treatment. Hereby, we can visualize all observed monotherapies, dual therapies and triple therapies with '+' indicating synergy while comparing observed vs predicted values. b, CT-VT-RT is the only regimen to elicit synergy as a triple regimen.

3.9 CT-VT-RT induced synergy was sustained upon substitution of temozolomide with lomustine

We aimed at identifying the specificity of synergistic regimen, CT-VT-RT by substituting TMZ with alternative alkylating agent, lomustine (CCNU), as is the case in patients with recurrent glioblastoma [12]. We determined the EC_{50} of lomustine in LN229 and LNZ308 to be 16 µM and 45 µM respectively using acute cytotoxicity assays (Fig. 17). As described previously, we performed cytotoxic survival assay with CCNU in combination with VT and RT as monotherapies, dual and triple regimens. The cell viability observed post monotherapies with RT and VT were similar to those seen in cytotoxic survival assays with TMZ (Figs. 18a and 18b). CCNU elicited a dose dependent effect in both LN229 and LNZ308 with comparable cell viability (Fig. 18c) upon treatments with respective EC_{50} dosages.
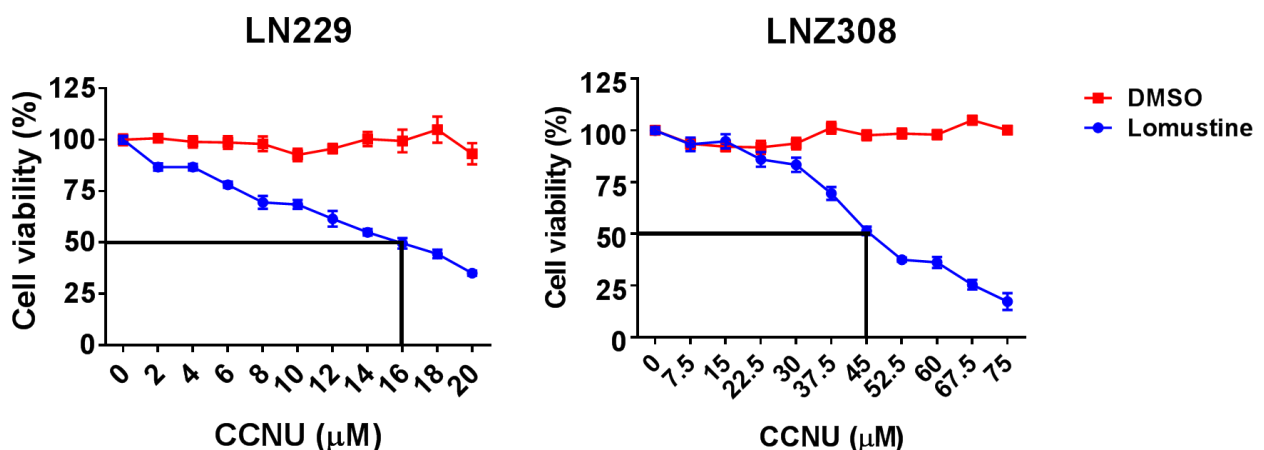

Figure 17. Determination of EC_{50} value for CCNU in LN229 and LNZ308 cells. The EC_{50} was identified to be 16 µM for LN229 and 45 µM for LNZ308. CCNU and DMSO are depicted by blue and red dose-response curves respectively.
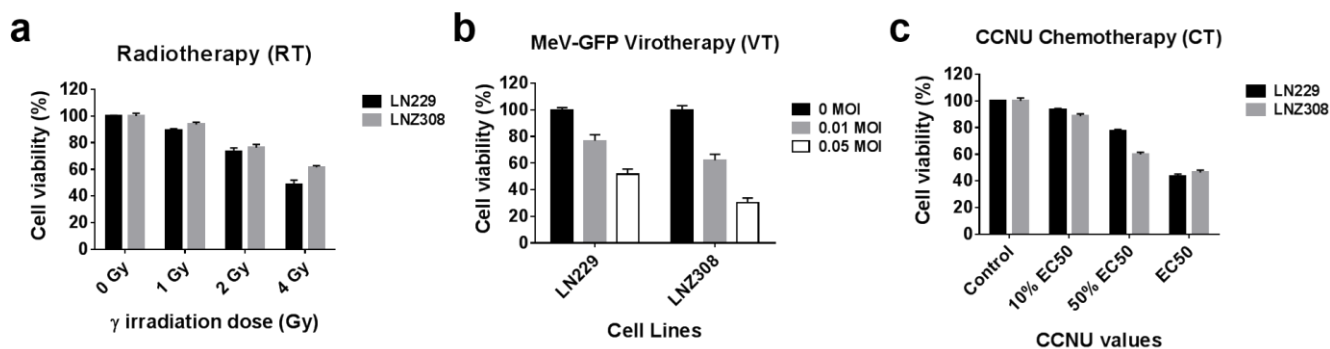
Figure 18*. Cytotoxic survival assay using lomustine (CCNU) as an alkylating agent.* *LN229 and LNZ308 cells were treated with monotherapies of **a,** γ-irradiation (RT), **b,** measles virotherapy (VT) and **c,** CCNU chemotherapy (CT). The cell viability post monotherapies were used to calculate predicted values of combinatorial treatment using fractional product method. Abbreviations: MOI, multiplicity of infection; EC_{50}, half maximal effective concentration.*

The CT-VT-RT initiated synergistic effect was sustained (Fig. 19) and more evident when substituting TMZ with CCNU implicating that underlying molecular machinery driving synergy were not restricted towards a specific chemotherapeutic drug but rather mobilized by similar mechanism of action. The CCNU employed CT-VT-RT sustained a significant synergistic effect even with maximal doses of irradiation (4 Gy) as was not the case with temozolomide in both LN229 and LNZ308 cells (Fig. 19a and 19b). Once again, in clinically relevant doses of 1 Gy and 2 Gy, CT-VT-RT was the only regimen to elicit synergy as a combination in both cell lines, at all dosages of virus and CCNU. VT-RT-CT could also elicit synergy at 1 Gy and 2 Gy in LN229 when combined with no CCNU or 10% EC_{50} (Fig. 19e) with loss of synergistic potential when dosing of CCNU was increased. The visualization of synergy as Chou-Talalay coefficients reaffirms the combinatorial efficacy of CT-VT-RT in both cell lines (Fig. 20) even with increasing doses of γ-irradiation upto 4 Gy.

We next characterized the potential of the synergistic regimen to improve therapy response in acquired temozolomide-resistant cells, recapitulating the nature of progressive recurrent tumor in glioblastoma patients undergoing treatment.
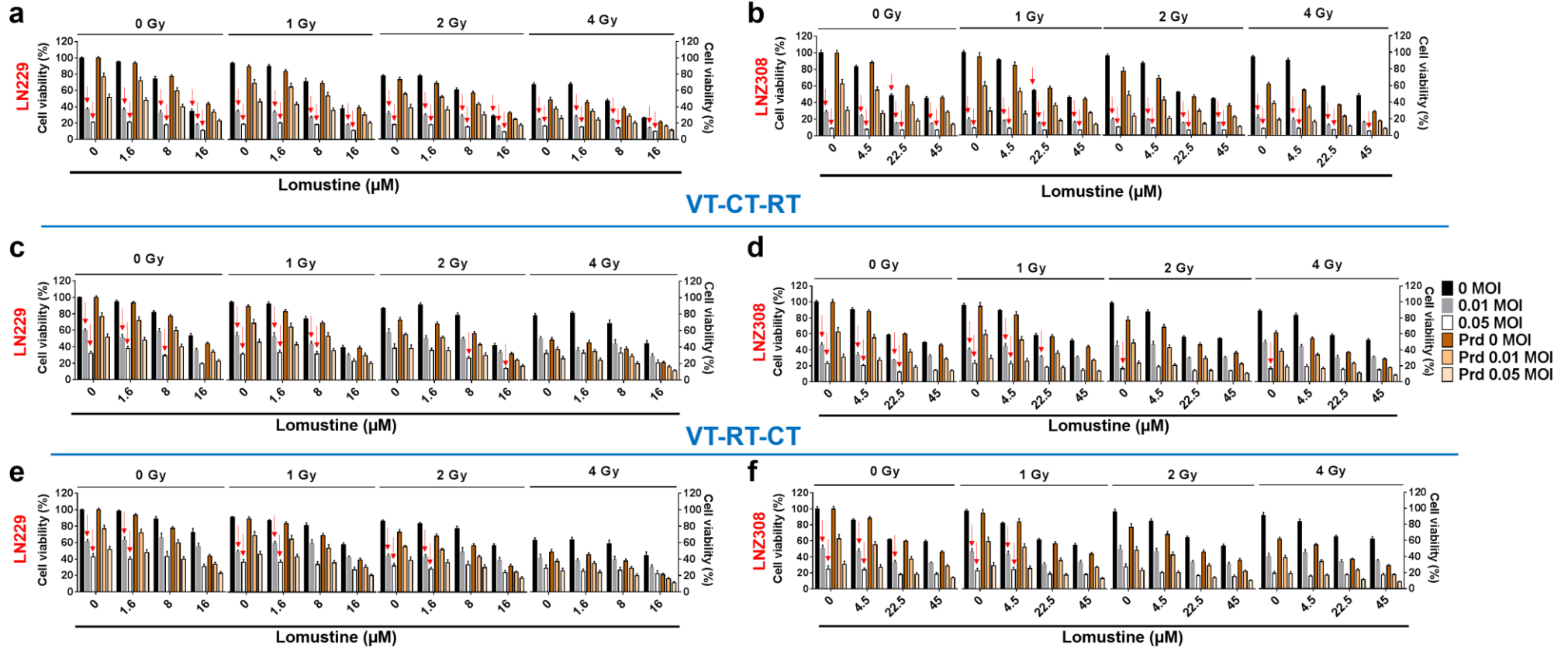
Figure 19. CT-VT-RT exhibited synergy while using Lomustine as chemotherapeutic agent (a) in LN229 and **(b)** LNZ308 cells respectively. Non-synergistic regimen VT-CT-RT showed poor combinatorial efficacy in **(c)** LN229 and **(d)** LNZ308. Non-synergistic regimen VT-RT-CT with poor combinatorial efficacy in **(e)** LN229 and **(f)** also in LNZ308. Red arrows indicate synergy realized in observed cell viability when compared to predictive values of co-treatments. Black, grey and white bars indicate observed values; Orange, brown bars indicate calculated predictive values from individual monotherapies (RT, VT, CT). Data expressed as Mean ± SEM, n = 9. Abbreviations: Prd, predicted; MOI, multiplicity of infection.
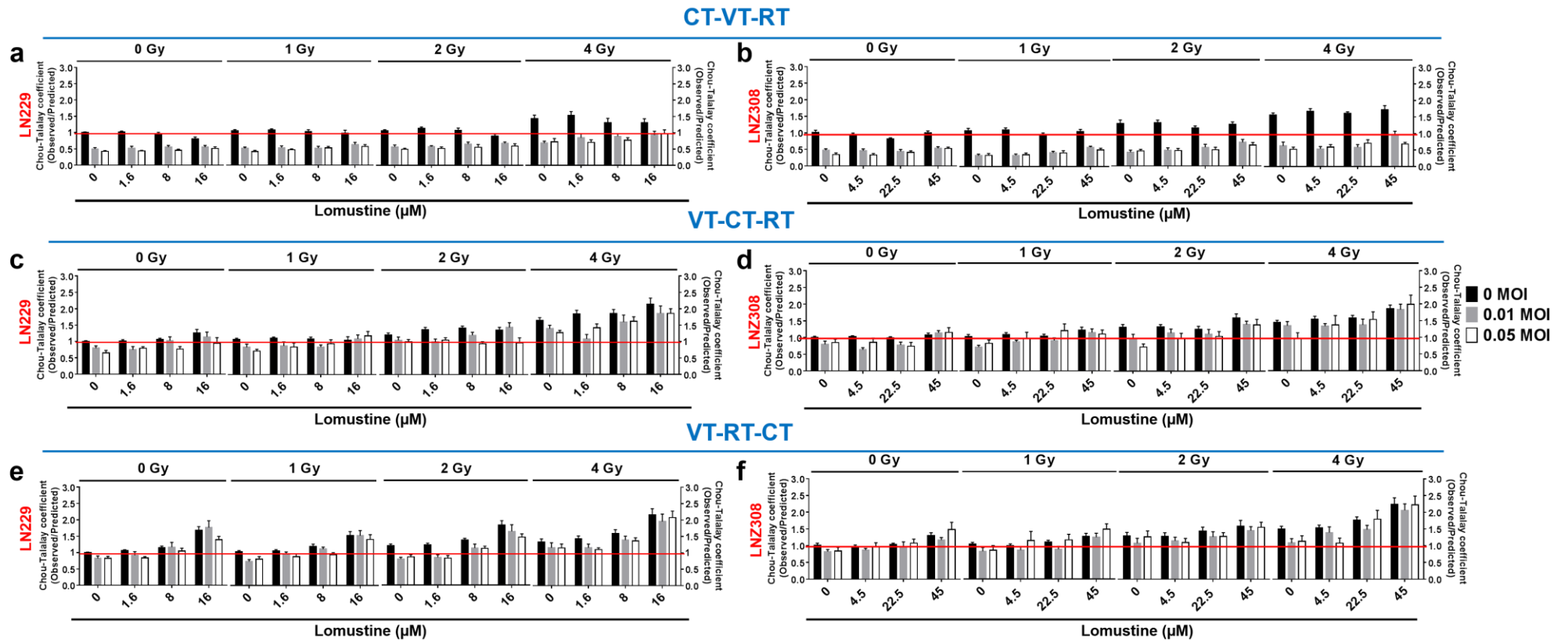
Figure 20. Triple regimen using CCNU as alkylating agent expressed as Chou-Talalay coefficients (ratio of observed/predicted cell viability). *The red line indicates coefficient of 1 which allows for determination of synergy (when < 1), additivity (when =1) and antagonism (when > 1) upon combination of agents. CT-VT-RT elicited maximal synergy in both **(a)** LN229 and **(b)** LNZ308. VT-initiated regimens showed non-synergistic activity in both LN229 and LNZ308 respectively in **(c, d)** VT-CT-RT and **(e, f)** VT-RT-CT. Black, grey and white bars indicate viral doses.*

3.10 CT-VT-RT rescues proliferative effect in temozolomide-resistant LN229 (R-LN229) cells

LN229 was continually treated with 100 µM TMZ in clonogenic survival assays to generate temozolomide-resistant LN229 (R-LN229) *in vitro*. R-LN229 cells were treated with CT-VT-RT employing CCNU, as used in patients with acquired temozolomide-resistant glioblastoma, along with clinically relevant radiation doses of 1 Gy and 2 Gy. The R-LN229 cells displayed higher cell viability than LN229 in the absence of CCNU (0 µm or DMSO) despite receiving treatment with irradiation and measles virus (Fig. 21, blue lines). However, both R-LN229 and parental LN229 cells exhibited comparable levels of susceptibility to MeV infection. Strikingly, treatment with synergistic CT-VT-RT resulted in killing of R-LN229 cells similar in parental LN229 cells (Fig.21, red lines) thereby rescuing the resistant proliferative effect. The initiation of treatment with alkylating chemotherapy followed sequentially with MeV and γ-irradiation (CT-VT-RT) was synergistic in glioma cells LN229 and LNZ308, glioma stem-like cell GS8 and in chemo-resistant cells R-LN229 with pronounced induction of viral proliferative mechanisms resulting in an enhanced oncolytic cascade effect.
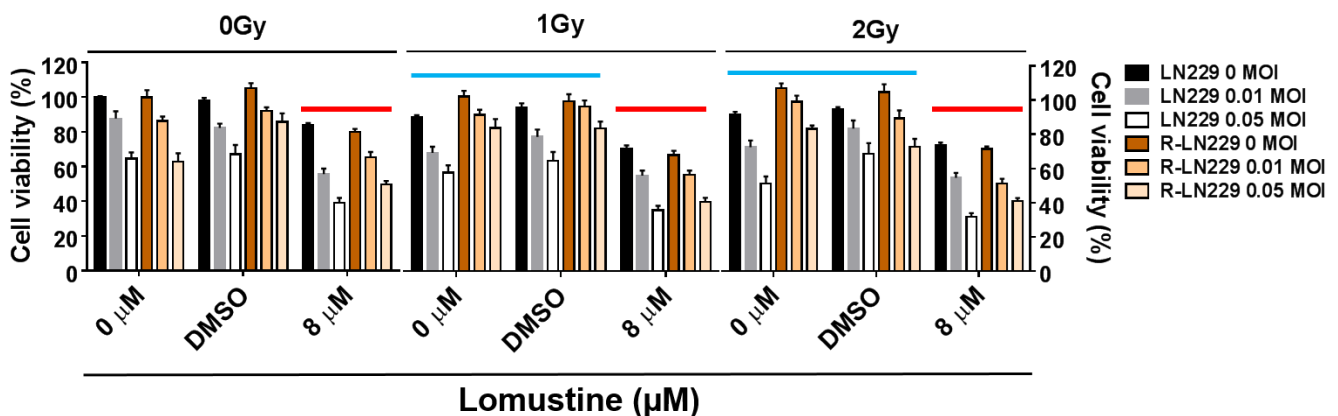
Figure 21. Synergistic triple regimen CT-VT-RT rescues temozolomide resistant effect using CCNU as the alkylating agent in R-LN229 cells. *Black, grey and white bars indicate cell viability post CT-VT-RT in parental LN229 cells. Orange, brown bars indicate cell viability post CT-VT-RT in temozolomide resistant R-LN229 cells. Addition of CCNU rescues resistant effect in synergistic regimen (red lines) as opposed to aggressive proliferative effect in absence of CCNU, i.e., 0 µM or DMSO (blue lines) with increasing doses of γ-irradiation. Data expressed as Mean ± SEM, n = 9.*

We aimed to understand these intrinsic molecular drivers of synergy in CT-VT-RT through RNA sequencing and their extracellular antigenic peptide presentation through HLA ligandome with consideration that the oncolytic nature of measles virus might lead to presentation of tumor associated / specific antigens or viral antigens resulting in a host initiated anti-tumoral immune response.

56

3.11 Generation of samples for RNASeq

We performed a RNASeq in LNZ308 cells at specific doses identified synergistic in LN229 as well, (i.e.) 2 Gy irradiation, 10% EC_{50} TMZ and 0.05 MOI MeV. LNZ308 cells were treated with monotherapies (RT- 2 Gy, CT- 130 μM, VT- 0.05 MOI), double regimen (CT-VT, 130 μM - 0.05 MOI), synergistic triple regimen (CT-VT-RT, 130 μM - 0.05 MOI - 2 Gy) along with CTL (DMSO) as control for CT initiated regimens and CTL (R/V) serving as control for RT alone and VT alone regimens. Samples including RNA and protein were harvested at 36 hpt, 72 hpt and 96 hpt along with a basal expression control (Blank) at 0 hpt. The RNA harvested at 0 hpt, 36 hpt and 96 hpt were sequenced to identify molecular signatures occurring chronologically at a transcriptional level. Supernatants were harvested post treatments at 96 hpt and used for cytokine/chemokine determination using ELISAs.

3.12 Data processing and identification of transcriptional signatures

Upon processing of the raw sequencing data and the statistical analysis of the data, we identified 2592 genes (Fig. 22) with significant alterations induced predominantly by regimens with MeV-GFP (Fig. 23) in our experimental setting. Extensive analysis of individual genes based on substantial literature review helped us identify transcriptional signatures induced by the virus resulting in viral proliferation enhancing proinflammatory, antiviral and anti-tumoral response pathways.

We set out a hypothesis that viral infectivity and proliferation in glioma cells allow for enhanced detection of viral RNA through innate sensors activating the RIG-I like receptor signalling pathway (RLR) resulting in production of interferon-beta (IFN-β) and ensuing type-1 interferon response (Fig. 24a). The binding of secreted IFN-β to the interferon α-β receptor (IFNAR) triggers the canonical Janus kinase/ signal transducers and activators of transcription (JAK-STAT) signalling (Fig. 24b) leading to phosphorylation of signal transducer and activator of transcription 1 (STAT1) and 2 (STAT2). STAT1 and STAT2 along with interferon regulatory factor 9 (IRF9) forms the interferon stimulated gene factor 3 complex (ISGF3) leading to transcription of interferon stimulated genes (ISGs). All transcribed ISGs possess the ability to initiate apoptosis apart from their innate antiviral responses [77]. The antiviral ISGs led to the activation of TNF-related apoptosis-inducing ligand (TRAIL) triggering apoptotic cascade (Fig. 24c). Furthermore, we identified a number of genes with antiviral and anti-tumoral properties, which were distinctively upregulated upon MeV infection and set out to characterize their role in eliciting combinatorial synergy in our CT-VT-RT regimen.
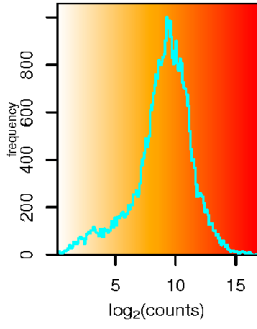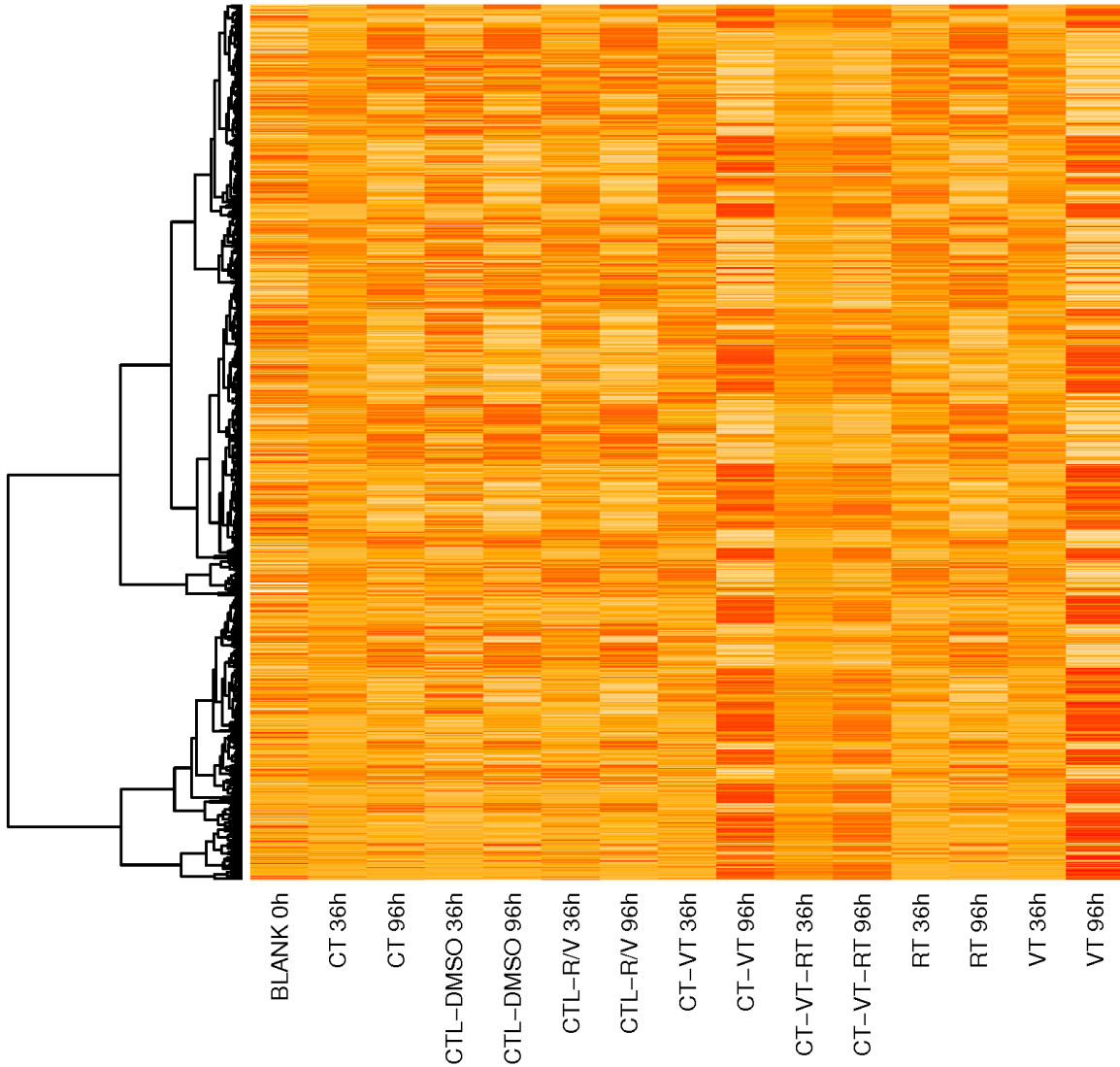
Figure 22. Transcriptional clustered heatmap of genes with significant interactions in our combinatorial treatment model. *The clustered genes (Y-axis) expressed as log₂ counts in a heatmap for each treatment (X-axis) sequenced at two time points of 36 hpt and 96 hpt along with basal expression control, Blank at 0 hpt.*
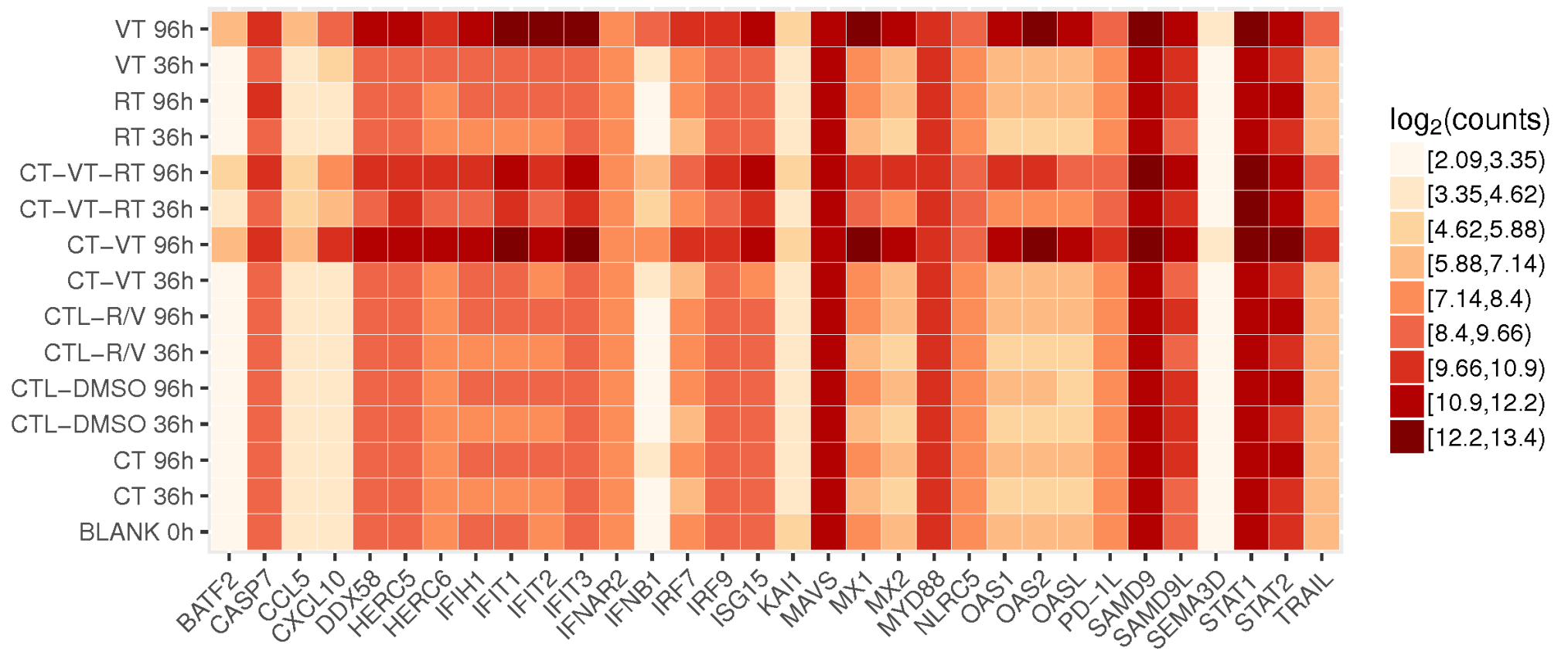
Figure 23. Transcriptional signature heatmap of select genes driving synergy post CT-VT-RT identified using RNASeq. *The list of genes (X-axis) were identified as key factors in determining synergy and their transcriptional profile in all treatments at 36 and 96 hpt (Y-axis) represented as log2 counts (mRNA copy numbers) in a heatmap. Blank (0 hpt) served as the basal expression control for further analysis.*

a

IFN-β

MeV fusion

MeV

MeV

CD46

CD46

CD46

MeV entry

MeV RNA

RIG1

MeV RNA

PACT MDA5

MeV RNA

RIG1

MAVS

MeV RNA

PACT MDA5

MAVS

MeV RNA

TLR 3/7/8

IKKε TBK1

BX795

MyD88

P IRF3 IRF7 P

IFN-β

Innate Viral
Sensors & Signalling

IRF3/7

IRE

NF-κB

IFN-β Genes

Cytokines/
Chemokines
(CXCL10, CCL5)

b

IFN-β

IFN-β

IFNR

Jak1 Jak2

P P

STAT2 STAT1

P STAT2

P STAT1

IRF9

Fludarabine

Anti-Viral
Response

IRF9

STAT1 STAT2

ISRE

ISGs
(OAS1, MX1, ISG15, IFIT1)

c

TRAIL

TRAILR1

GTP

DAP3

FADD

Caspase8

Caspase3/7

CYTOPLASM

Viral Initiated
Anti-Tumoral Response

Apoptosis

NUCLEUS

Fig. 24. Schematic overview of molecular drivers in CT-VT-RT based on RNA sequencing. a, Measles virus entry through receptor fusion events lead to insertion of viral genome recognized by innate RLR signalling pathway which initiated a Type I Interferon response through secretion of IFN-β along with pro-inflammatory chemokines. b, Activation of JAK-STAT signalling by IFN-β lead to transcription of ISGs along with maintenance of autocrine STAT1 signalling eventually leading to c, TRAIL dependent apoptosis of glioma cells in addition to the oncolytic death cascade initiated by the virus. Red circles highlight inhibitors BX795 and fludarabine; white font indicates human molecules, viral molecules are indicated in black font. Underlined molecules were not identified as significantly interacting genes in the RNASeq.

3.13 Activation of type-1 interferon response by VT-containing regimens

All VT containing regimens (VT, CT-VT, CT-VT-RT) significantly induced detection of MeV RNA genomes by RLR signalling pathway through upregulation of DDX58 and IFIH1 leading to phosphorylation of IRF7 with eventual transcription of IFN-β (Fig. 23 and 24a). The innate RNA sensor, DDX58 was maintained at basal levels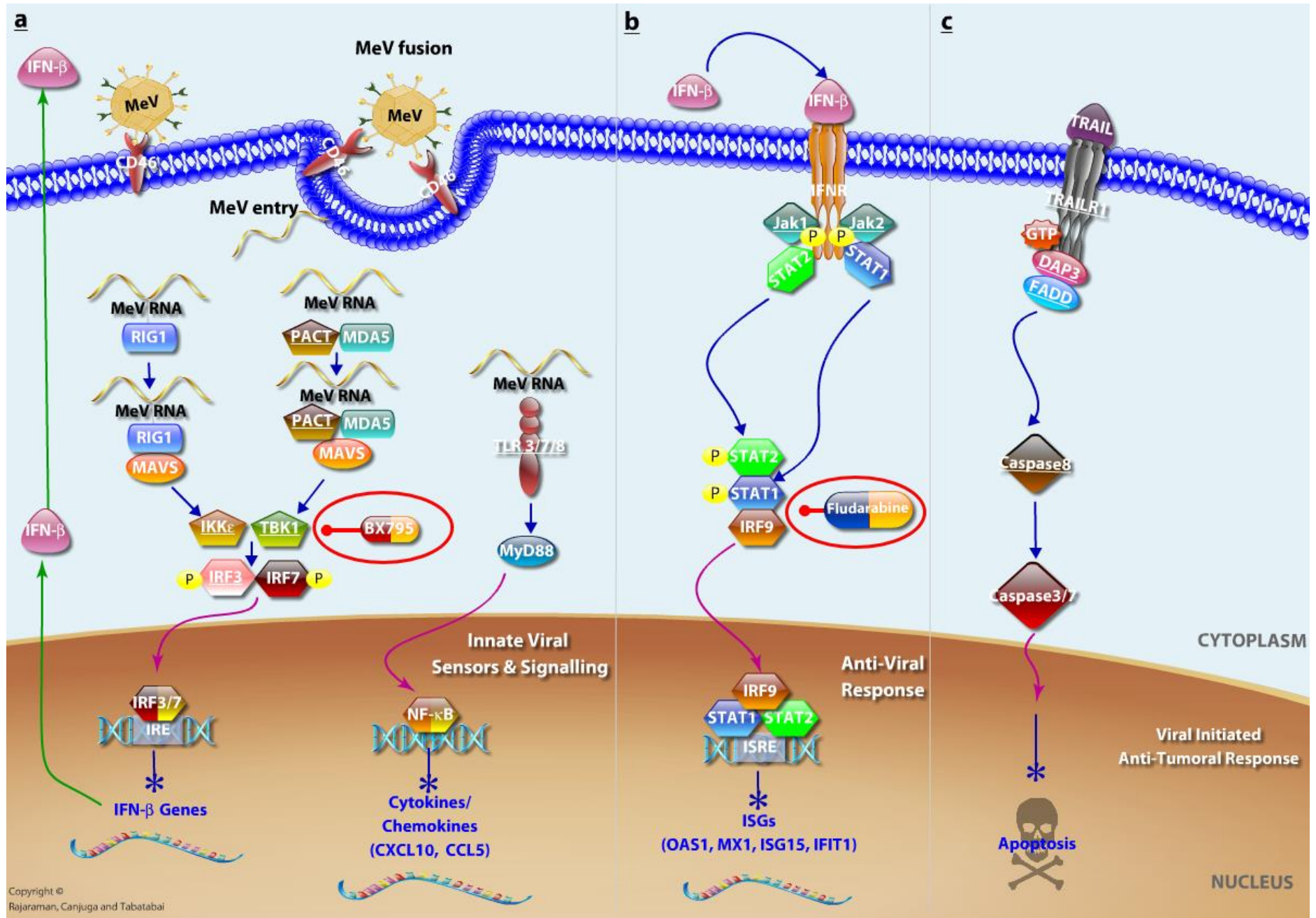 at 36 hpt in all treatments including VT containing regimens with a 100-fold increase in mRNA levels at 72 hpt in VT, CT-VT and CT-VT-RT (Fig. 25a) indicating the viral replication events leading to availability of higher copy number of viral genomes for detection. Intrinsic RLR signalling leading to transcription and secretion of IFN-β peaked at 96 hpt with a 1000-fold increase in mRNA levels in VT, CT-VT and CT-VT-RT (Fig. 25b) further validating the chronological sequence of early innate sensors at 72 hpt culminating in Type I interferon production maintained at 96 hpt due to autocrine nature of IRF7 - IFN-β - STAT1 signalling. Furthermore, our transcriptional data correlated with secreted IFN-β protein levels with detection of 123 pg/ml, 113 pg/ml and 103 pg/ml of IFN-β per microgram of whole protein in VT, CT-VT and CT-VT-RT respectively (Fig. 25c) using Enzyme linked immunosorbent assay (ELISA) measured at 96 hpt with no detectable IFN-β in other treatment regimens.
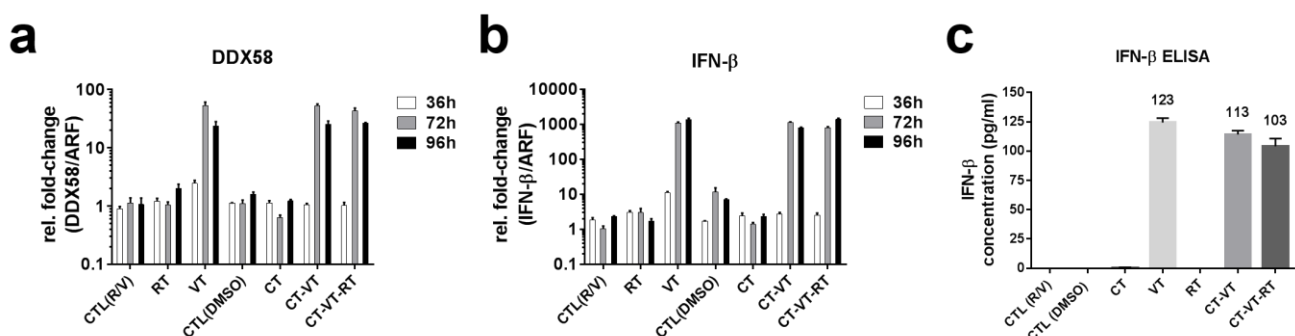
Figure 25. MeV initiates type-1 interferon response through RLR signalling. a, Increase in mRNA expression of innate sensor DDX58 in VT-containing regimens detected by qPCR. b, Increased IFN-β transcription observed upon MeV infection by qPCR c, MeV induced secretion of IFN-β detected by ELISA. Data expressed as Mean ± SEM, n = 3.

3.14 IFN-β activates canonical JAK-STAT signalling to initiate an antiviral, anti-proliferative state

The binding of secreted IFN-β to the IFNAR receptors triggers the downstream canonical JAK-STAT signalling leading to phosphorylation of STAT1 and STAT2 which along with IRF9 forms the ISGF3 leading to transcription of interferon stimulated genes (ISGs, (Fig. 24b)). We observed a 6-8 fold increase in STAT1 mRNA levels in VT and CT-VT regimen at 72 hpt, with a gradual decline at 96 hpt (Fig. 26a). Inversely, the STAT1 mRNA levels increased from 5-fold at 72 hpt to 6-8 fold at 96 hpt in CT-VT-RT (Fig. 26a) indicating a delayed STAT1 signalling allowing for efficient viral proliferation in the absence of host antiviral responses. The nuclear translocation of phosphorylated ISGF3 induced the transcription of antiviral ISGs (Fig. 24b), which include the viral RNA degradation proteins 2'-5'-oligoadenylate synthases 1 and 2 (OAS1 and OAS2), inactivators of viral ribonucleocapsid; i.e., MX Dynamin Like GTPase 1 and 2 (MX1 and MX2), antiviral ubiquitin like protein ISG15 ubiquitin-like modifier (ISG15), antiviral ligases for ISGylation HECT and RLD domain containing E3 ubiquitin protein ligase 5 and 6 (HERC5 and HERC6) and inhibitors of viral mRNAs; Interferon induced protein with tetratricopeptide repeats 1, 2 and 3 (IFIT1, IFIT2 and IFIT3). All transcribed ISGs possess the ability to initiate apoptosis apart from their innate antiviral responses [77]. The ISG transcripts indicate a distinct antiviral state as early as 72 hpt with a 100-fold increase in ISG15 and IFIT2 mRNA levels, while a 1000-fold increase was observed in MX1, MX2, OAS1 and OAS2 mRNAs in all virus containing regimen (Figs. 26b - g). We observed a significant increase particularly in ISG15 and OAS1 mRNAs in CT-VT-RT compared to VT and CT-VT at 96 hpt along with non-significant differences in other ISGs (Figs. 26b - g).
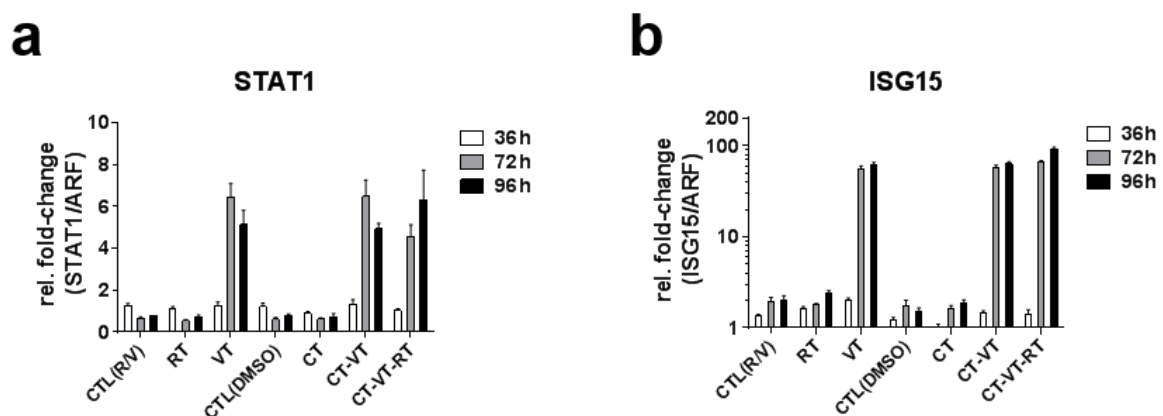
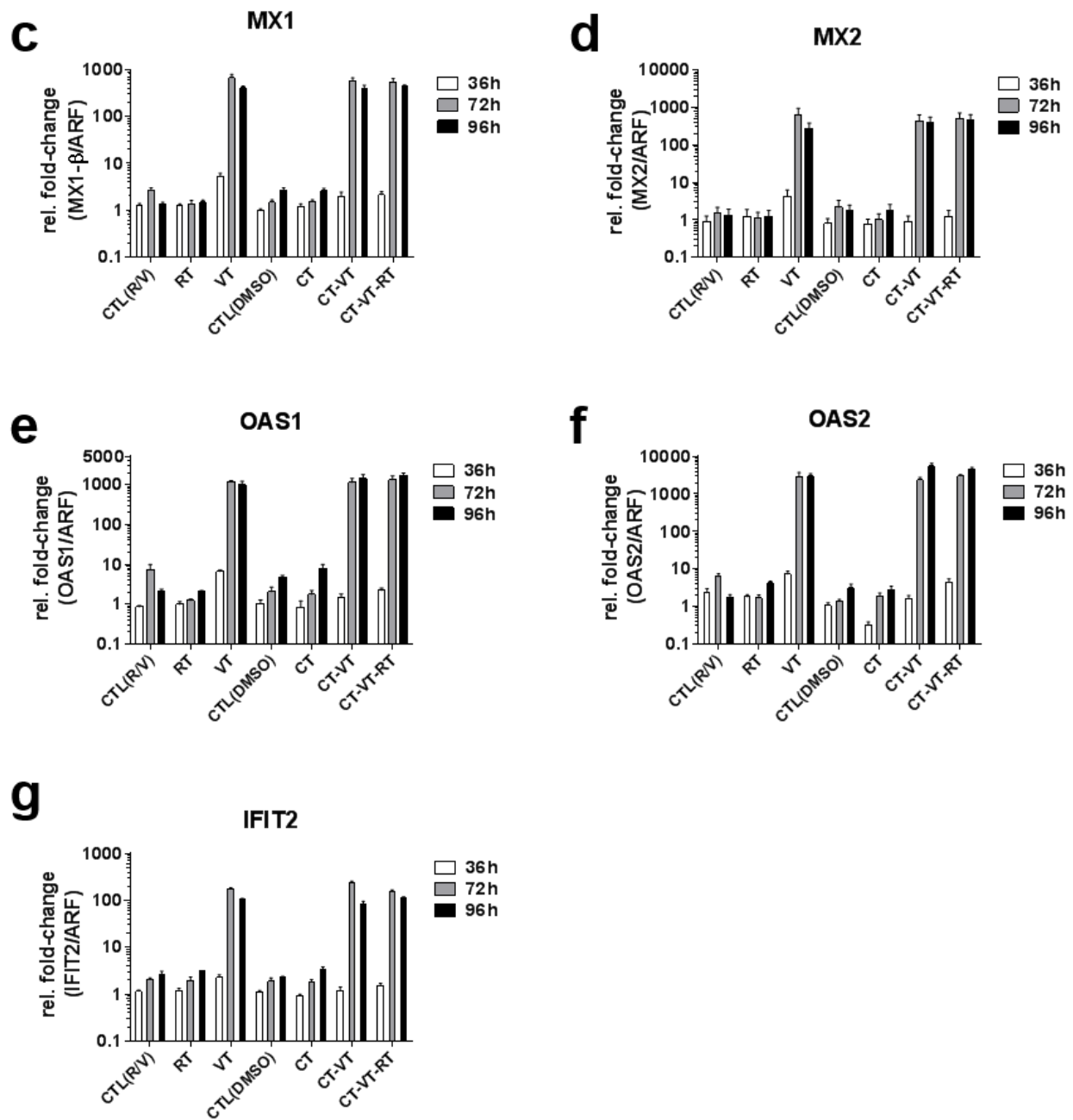**Figure 26. MeV activates JAK-STAT signalling resulting in transcription of ISGs.** *MeV dependent increase in mRNA expression of **a,** STAT1 leading to downstream transcription of ISGs including **b,** ISG15 **c,** MX1 **d,** MX2 **e,** OAS1 **f,** OAS2 and **g,** IFIT2 as detected by qPCR. Gene expression expressed in terms of relative fold-change to housekeeping gene, ARF. Data expressed as Mean ± SEM, n = 3.*

3.15 CT-VT-RT upregulates expression of antiviral, anti-tumoral interferon related gene SAMD9

We identified a number of interferon related genes with antiviral and anti-tumoral properties, which were distinctively upregulated upon MeV infection. The sterile alpha motif domain – containing protein 9 (SAMD9) was expressed at basal levels in LNZ308 (0 h) with no change in expression upon CT, DMSO or RT (Fig. 27a, upper panel). However, there was a significant increase in SAMD9 protein expression upon MeV infectivity at 72 hpt and 96 hpt in all VT containing regimens with CT-VT-RT showing heightened expression in comparison to VT alone (Fig. 27a, upper panel). SAMD9 is a host factor involved in suppression of myxoma virus with interaction through its N-terminus and shown to form antiviral stress granules to sequester poxvirus [78,79]. Moreover, deletion of SAMD9 has been associated with formation of tumors while overexpression has been shown to suppress non-small cell lung cancer *in vitro* and *in vivo* thereby signifying its antiviral, tumor suppressive characteristics in our setting [80,81]. Similarly, we observed overexpression of anti-tumoral host factor, basic leucine zipper transcriptional factor ATF2- like protein (BATF2) during RNASeq (Fig. 23) in all VT containing regimens with emerging evidence supporting its tumor suppressive properties [82,83]. However, the increase in mRNA expression from RNASeq did not correlate with BATF2 protein levels with basal level (0 h) of BATF2 expression detected in all treatments (Fig. 27b, upper panel) with increasing time course.

3.16 IFN-β stimulated ISGs initiate TRAIL dependent apoptosis in CT-VT-RT

The IFN-β stimulated antiviral ISGs lead to the activation of TNF related apoptosis inducing ligand (TRAIL) triggering apoptotic cascade in all VT containing regimens. TRAIL protein expression observed through immunoblots was higher in CT-VT and CT-VT-RT compared to VT at 72 hpt and 96 hpt (Fig. 27a, middle panel). Furthermore, expression of TRAIL corresponded to Caspase 3/7 activity with a 3-fold increase observed in CT-VT at 72 hpt and over 2-fold increase in CT-VT-RT regimen at 72 hpt and 96 hpt in comparison to 1.5-fold increase in VT alone (Fig. 27c). Moreover, the absence of TRAIL expression in other regimens indicated that the elevated expression in CT-VT-RT was not due to a mere additive effect of VT with RT and CT but rather a consequence of enhanced viral replication favoured in the synergistic regimen provoking a substantial host antiviral response with eventual apoptosis (Fig. 24c).

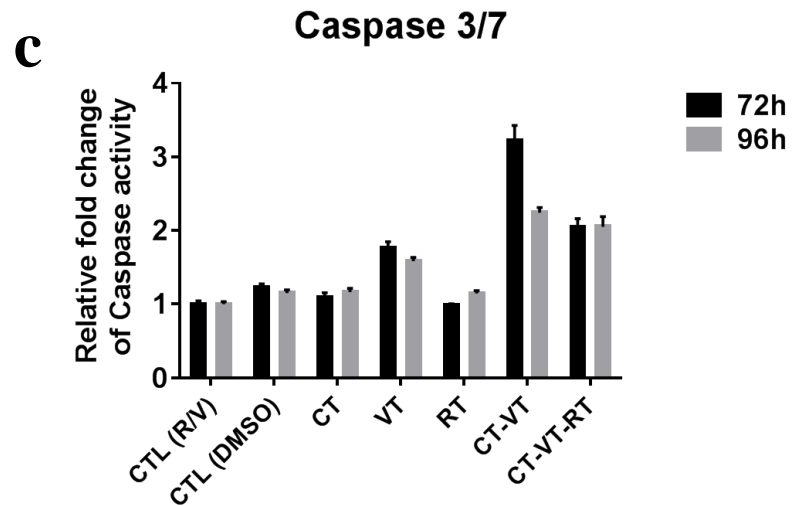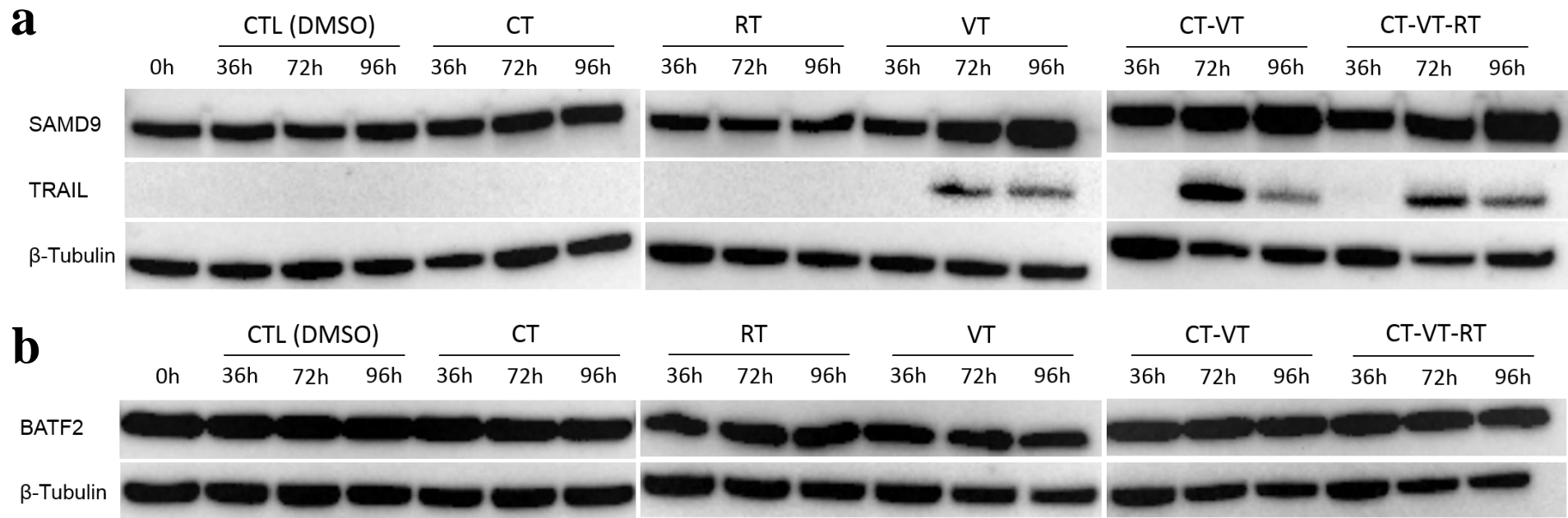**Figure 27. VT-containing regimens activate TRAIL dependent apoptosis. a,** *Immunoblot analysis of SAMD9 (upper panel), TRAIL (middle panel) and loading control, β-tubulin (lower panel) performed chronologically in all regimens.* **b,** *Immunoblot analysis of BATF2 (upper panel) and β-tubulin (lower panel).* **c,** *Caspase 3/7 activity assay measured at 72 hpt and 96 hpt. Data expressed as Mean ± SEM, n = 3.*

3.17 Production of chemokines triggering an antiviral, anti-tumoral immune response

In addition to induction of apoptosis, the infection of LNZ308 cells with MeV-GFP led to secretion of chemokine signalling molecules quantified by ELISA, which are associated with stimulation and function of immune cells. The synergistic regimen, CT-VT-RT, significantly upregulated C-X-C motif chemokine-10 (CXCL10) expression with detection of 633.9 pg/ml of CXCL10 per microgram of whole protein in comparison to 289.6 pg/ml in CT-VT, 263.3 pg/ml in VT (Fig. 28a) and only 25.1 pg/ml in CTL (R/V). The overexpression of CXCL10 upon CT-VT-RT treatment signifies the immune-stimulatory potential of this regimen with upregulated mortality. CXCL10 is a virus driven protein in this setting, since it is a RIG-1/IFIH1 inducible gene, which can further instigate anti-tumoral immune response through activation of CD8^{+} cytotoxic T cells [84,85]. Interestingly, only the virotherapy-containing regimens (Fig. 23) uniquely expressed the leukocyte migratory C-C motif chemokine-5 (CCL5), also known for its antiviral action against different human immunodeficiency virus (HIV) strains [86,87]. VT elicited a maximal secretion of CCL5 with 45.2 pg/ml per microgram of whole protein, while CT-VT and CT-VT-RT had lower expression with 25.7 pg/ml and 32.5 pg/ml (Fig. 28b) respectively. The potent immune-stimulatory and chemoattractant potential of both induced chemokines, CXCL10 and CCL5 can trigger a virotherapy-induced host-directed immune response with eventual anti-glioma activity.
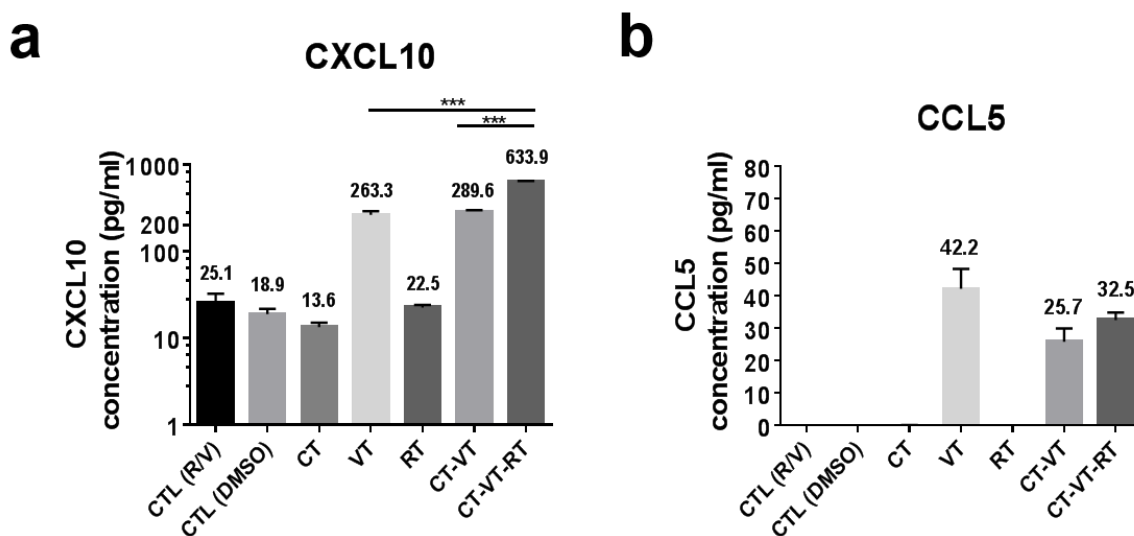

***Figure 28. VT-containing regimes induce production of proinflammatory chemokines. a,** CT-VT-RT significantly increased secretion of CXCL10 in comparison to CT-VT and VT alone. **b,** CCL5 was produced only by VT-containing regimens with highest secretion observed in VT alone as detected by ELISA. Data expressed as Mean ± SEM, n = 3.*

3.18 Selective inhibition of TBK1/IKKε or STAT1 signalling abrogates type-1 interferon response and canonical JAK-STAT signalling resulting in loss of TRAIL expression

We aimed to further characterize the role of the RLR - IFN-β - STAT1 signalling axis by using the compound BX795 to selectively inhibit Tank binding kinase-1 (TBK1)/ IkappaB kinase epsilon (IKKε) signalling that should downregulate IFN-β (Fig. 24a, red circle). Moreover, we used fludarabine to inhibit downstream STAT1-signalling (Fig. 24b, red circle) and the transcription of STAT1 was indeed downregulated (Fig. 29a) by both substances as well as by the combination post CT-VT-RT treatment. Further, as expected IFN-β transcription was downregulated upon BX795 and combination of BX795 + fludarabine but also in fludarabine alone (Fig. 29b) post CT-VT-RT. The mRNA expression correlated with production of IFN-β corresponding to 158 pg/ml and 226 pg/ml of IFN-β protein detected in CT-VT-RT alone and CT-VT-RT + DMSO respectively (Fig. 29c) but no IFN-β in samples treated with inhibitors. The specific inhibition of STAT1 phosphorylation by fludarabine resulting in upstream inhibition of IFN-β suggested interdependency and autocrine feedback loop in our setting. We have previously shown the absence of RLR and downstream type-1 interferon signalling in CTL (R/V) regimen (Figs. 25a - c) and were hence, not pursued in this experimental setting with molecular inhibitors.

The inhibition of STAT1-signalling was further validated through immunoblot analysis with complete loss of phospho-STAT1 (Y701) in treatments with CT-VT-RT plus fludarabine, CT-VT-RT plus BX795, and CT-VT-RT plus BX795 plus fludarabine while phospho-STAT1 was visible in CT-VT-RT alone and CT-VT-RT + DMSO (Fig. 29d, upper panel). However, despite the absence of phospho-STAT1 we identified similar levels of total STAT1 protein (Fig. 29d. middle panel) in all treatments besides cells treated with CT-VT-RT plus fludarabine that revealed increased amounts of STAT1 protein. These increased levels of total STAT1 when subjected to fludarabine alone (Fig. 29d. middle panel) could be due to intact upstream signalling with induction of IFN-β and subsequent STAT1 transcription, but lack of phosphorylation thereof preventing activation of downstream transcriptional and autocrine signalling events via the IFNAR feedback loop.

The viral RNA-dependent RLR signalling was activated through upregulation of DDX58 mRNA levels in CT-VT-RT alone and CT-VT-RT + DMSO (Fig. 29e) as expected. Interestingly, mRNA levels of DDX58 were significantly downregulated in IFN-β–STAT1 inhibited samples suggesting a role of IFN-β in sustenance of DDX58 transcription. The secretion of IFN-β correlates with downstream transcription of ISGs as evidenced by increased levels of MX1 and ISG15 mRNA (Figs. 29f and 29g) in CT-VT-RT alone and CT-VT-RT + DMSO. This was accompanied with a complete loss of ISGs at the transcriptional level (Fig. 29f and 29g) upon

inhibition of IFN-β - STAT axis. The transcriptional downregulation of ISGs was followed by subsequent loss of TRAIL expression in the IFN-β - STAT axis inhibited samples (Fig. 29h, upper panel) and thereby validating our hypothesis of apoptosis induction by the stimulated ISGs. We distinctively observed TRAIL expression in CT-VT-RT alone and in CT-VT-RT + DMSO (Fig. 29h, upper panel), further demonstrating the proinflammatory and anti-tumoral activity of IFN-β.
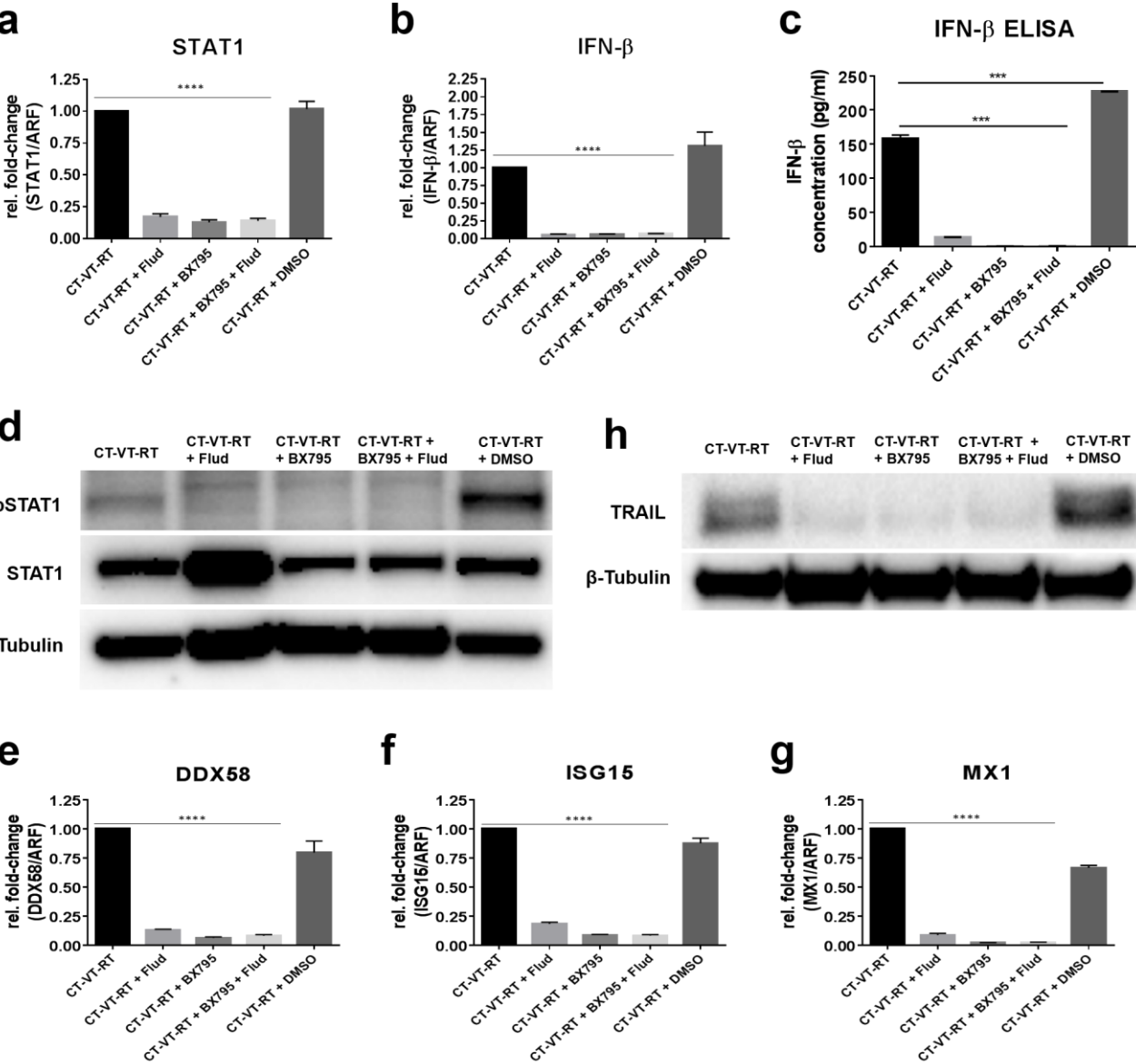
Figure 29. BX795 and Fludarabine inhibits IFN-β induced JAK-STAT pathway. a, *Transcription of STAT1 mRNA is significantly downregulated upon treatment with CT-VT-RT plus BX795 and/or fludarabine as detected by qPCR. b, Loss of IFN-β mRNA transcription in treatments with small molecule inhibitors detected by qPCR. c, BX795 inhibits IFN-β production while negligible amounts detected after treatment with fludarabine. CT-VT-RT + DMSO significantly increases secretion of IFN-β as detected by ELISA. d, Immunoblot revealing lack of STAT1 phosphorylation in samples treated with*

fludarabine and in BX795 alone or combination (upper panel). All samples expressed total STAT1 (middle panel) and β-tubulin served as loading control (lower panel). e - g, Complete loss of ISG transcription as detected by mRNA expression of e, DDX58 f, ISG15 and g, MX1 in cells treated with CT-VT-RT containing BX795 and/or fludarabine. h, Immunoblot analysis revealed absence of TRAIL protein (upper panel) in IFN-β –STAT1 inhibited samples while TRAIL was distinctively observed in CT-VT-RT alone and CT-VT-RT + DMSO. β-tubulin served as loading control (lower panel). One-way ANOVA with Dunnett's multiple comparison test in a - c, e - g; *, p < 0.05; **, p < 0.01; ***, p < 0.001; ****, p < 0.0001. Data expressed as Mean ± SEM, n = 3 in a - c, e - g.

3.19 SAMD9 and BATF2 are not classical interferon stimulated genes in our paradigm

The selective inhibition of IFN-β – STAT1 axis downregulates classical interferon stimulated genes transcribed through ISGF3 complex (Figs. 29f and 29g), but we identified SAMD9 and BATF2 to be innate host factors independent of type I interferon response. The expression of SAMD9 was uninfluenced upon inhibition of IFN-β – STAT1 pathway with similar levels of expression observed in all treatments (Fig. 30, upper panel). Accompanied with basal level of SAMD9 expression previously observed (Fig. 27a, upper panel), the subsequent increase in SAMD9 protein expression upon MeV infection warrants further studies to characterize its antiviral mechanism of action.
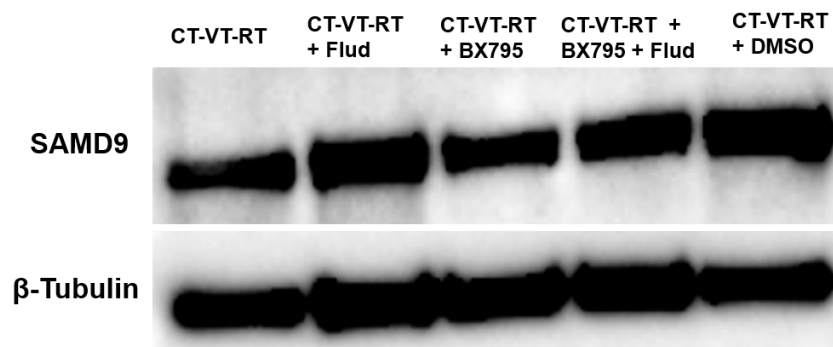
Figure 30. SAMD9 expression remains unchanged upon small molecule inhibition. Immunoblots reveals similar levels of SAMD9 protein (upper panel) post CT-VT-RT and in combination with inhibitors. β-tubulin served as loading control (lower panel).

Interestingly, the previously uninfluenced BATF2 protein (Fig. 27b, upper panel) was highly upregulated in IFN-β – STAT1 inhibited samples in comparison to CT-VT-RT alone or CT-VT-RT + DMSO (Fig. 31, upper panel) suggesting possible interactions of host antiviral factors in the absence of type I interferon response. Cells subjected to CT-VT-RT + fludarabine expressed BATF2 at high levels with corresponding increase in IRF1 expression (Fig. 31, middle panel). Similar correlation of IRF1 with BATF2 expression were observed in cells subjected to CT-VT-RT + BX795 alone or together with fludarabine but no expression of IRF1

in CT-VT-RT alone or in CT-VT-RT + DMSO suggesting a BATF2 dependent transcription of IRF1.
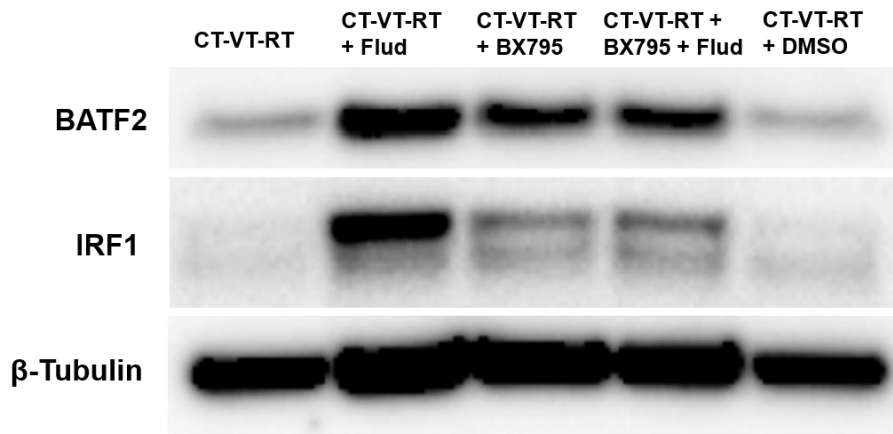
Figure 31. Inhibition of type 1 interferon response pathway post CT-VT-RT results in synchronous increase of BATF2 and IRF1 protein. Immunoblot analysis revealed increased in BATF2 protein expression (upper panel) in IFN-β-STAT1 inhibited samples with maximal expression after treatment with CT-VT-RT + fludarabine. Corresponding increase in IRF1 expression (middle panel) and β-tubulin (lower panel) was used as loading control.

3.20 BATF2 interaction with IRF1 in absence of type I interferon response visualized through proximity ligation assay

We therefore carried out a proximity ligation assay to test for possible interaction of BATF2 with IRF1 and identified an increased red amplification signal in cells subjected to CT-VT-RT plus fludarabine (Fig. 32a). Despite a minimal basal signal in treatments and in IgG controls (Fig. 32a, insets), we noticed a coherence along with immunoblot analysis to confirm increased abundance of BATF2 and IRF1 in close proximity leading to transcription of downstream targets resulting in apoptosis as evidenced by caspase 3/7 activity (Fig. 32b). Moreover, we observed caspase activity similar to CT-VT-RT despite the abrogation of TRAIL expression in CT-VT-RT plus BX795, (Fig. 32b and 29h, upper panel) demonstrating the induction of an alternative apoptotic machinery by the substitutive BATF2-IRF1 interaction. Furthermore, we identified decreased but clearly detectable expression of CCL5 in synergistic regimen combined with small molecule inhibitors. We found relative higher expression in CT-VT-RT plus fludarabine treated cells in comparison to CT-VT-RT plus BX795 alone or together with fludarabine treatment (Fig. 32c). Of note, *CCL5* has previously been reported to be a BATF2 – IRF1 induced gene [88], and we observed a correlation in expression in accordance with BATF2 and IRF1 expression in our setting.
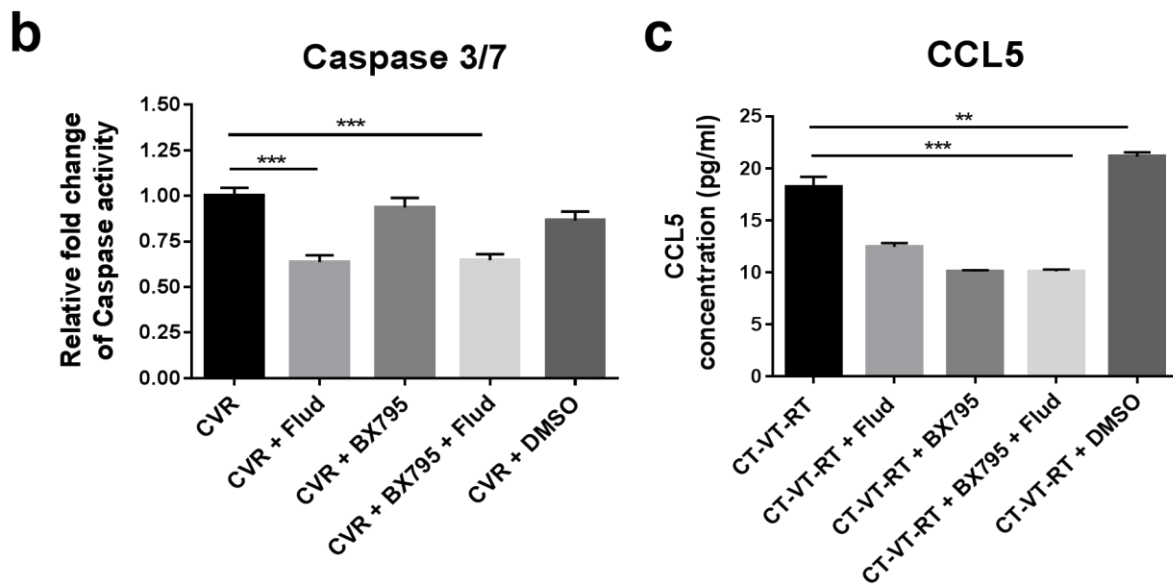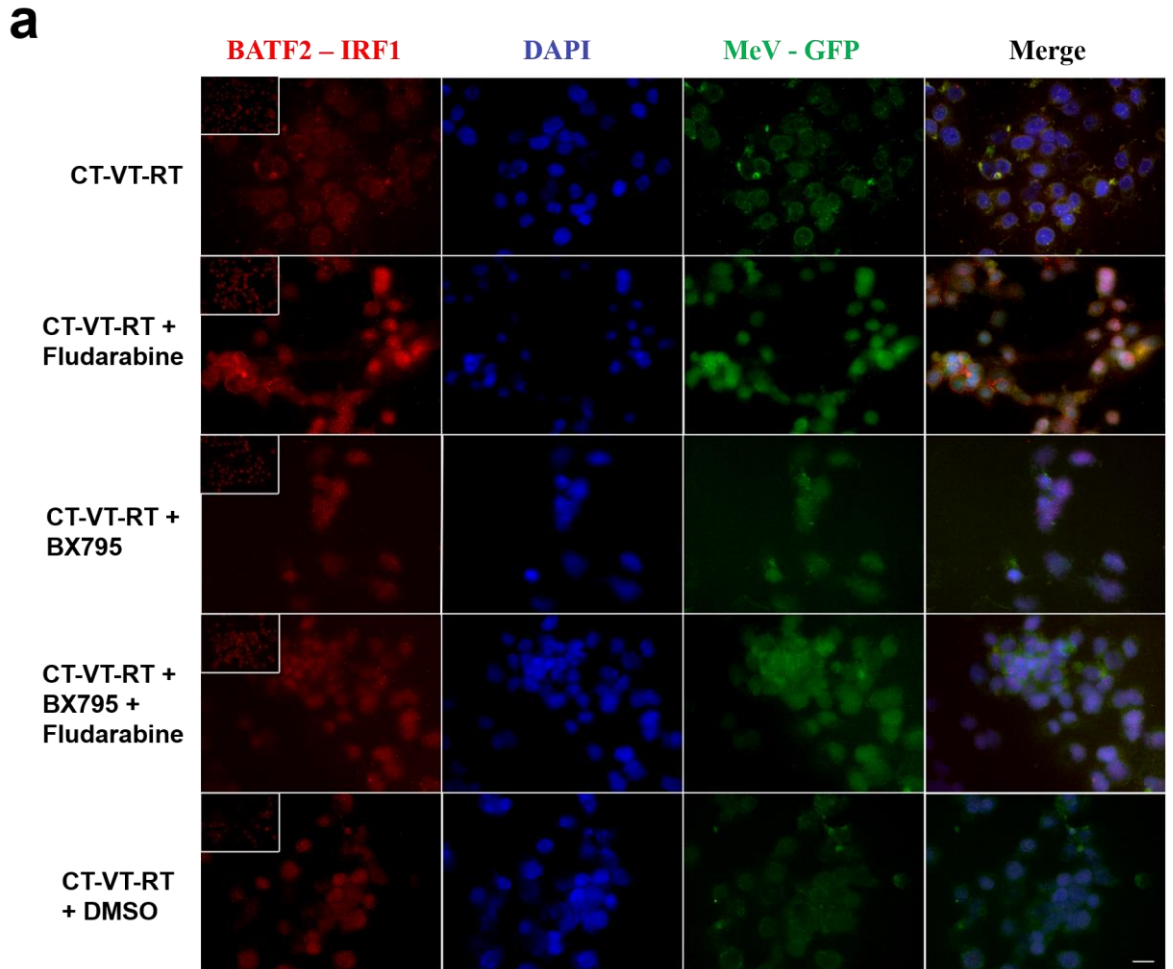
Figure 32. BATF2 interacts with IRF1 in the absence of IFN-β-STAT1 signalling. a, *Proximity ligation assay reveals potential interaction of BATF2 with IRF1 observed through red amplification signal with highest intensity in cells treated with CT-VT-RT + fludarabine while basal signal was observed in CT-VT-RT and CT-VT-RT + DMSO alongside IgGs (Inset). **b,** Caspase 3/7 activity assay in CT-VT-RT*

*treatments along with BX795 and/or fludarabine. **c,** Decreased CCL5 expression in CT-VT-RT treatments containing small molecule inhibitors detected by ELISA. Data expressed as Mean ± SEM, n = 3 in **b** and **c**.*

3.21 Activation of MHC class I expression by IFN-β dependent ISGF3 transcription

The ISGF3 complex upon activation by IFN-β can bind the ISRE element in the promoter region and upregulate MHC class I expression [89]. We observed a significant increase in MHC class I expression in the virus-containing regimens including antigen processing protein such as antigen peptide transporter protein TAP1 through RNASeq (Fig. 23) and the antigen processing pathway protein was indeed upregulated with similar mRNA levels of TAP1 at 72 hpt and 96 hpt (Fig. 33a) in all virus-containing regimens. The synergistic regimen CT-VT-RT showed 1.5- to 2-fold elevated expression of mRNA levels in MHC I, A (HLA-A) and B (HLA-B) at 96 hpt in comparison to CT-VT or VT (Figs. 33b and 33c) suggesting a potential for increased presentation of host tumor antigens along with putative viral antigens. This was further complemented with no MHC class I expression observed in other treatments (Figs. 33b and 33c) indicating a clear IFN-β-dependent expression and thus the increase in MHC class I expression was due to CT-VT-RT sustained innate antiviral response. Identification of potential tumor or viral antigens presented through HLA ligandome might help identify immunogenic peptides that could be used to mobilize adaptive immune responses targeting tumor/viral host.

*Figure 33. MeV infection increased transcription of antigen processing and presentation pathways. VT-containing regimens increased antigen processing through **a,** upregulated TAP1 transcription along with increase in **b,** HLA-A and **c,** HLA-B mRNA expression as detected by qPCR.*

3.22 CT-VT and CT-VT-RT lead to increased presentation of antigens on MHC class I molecules
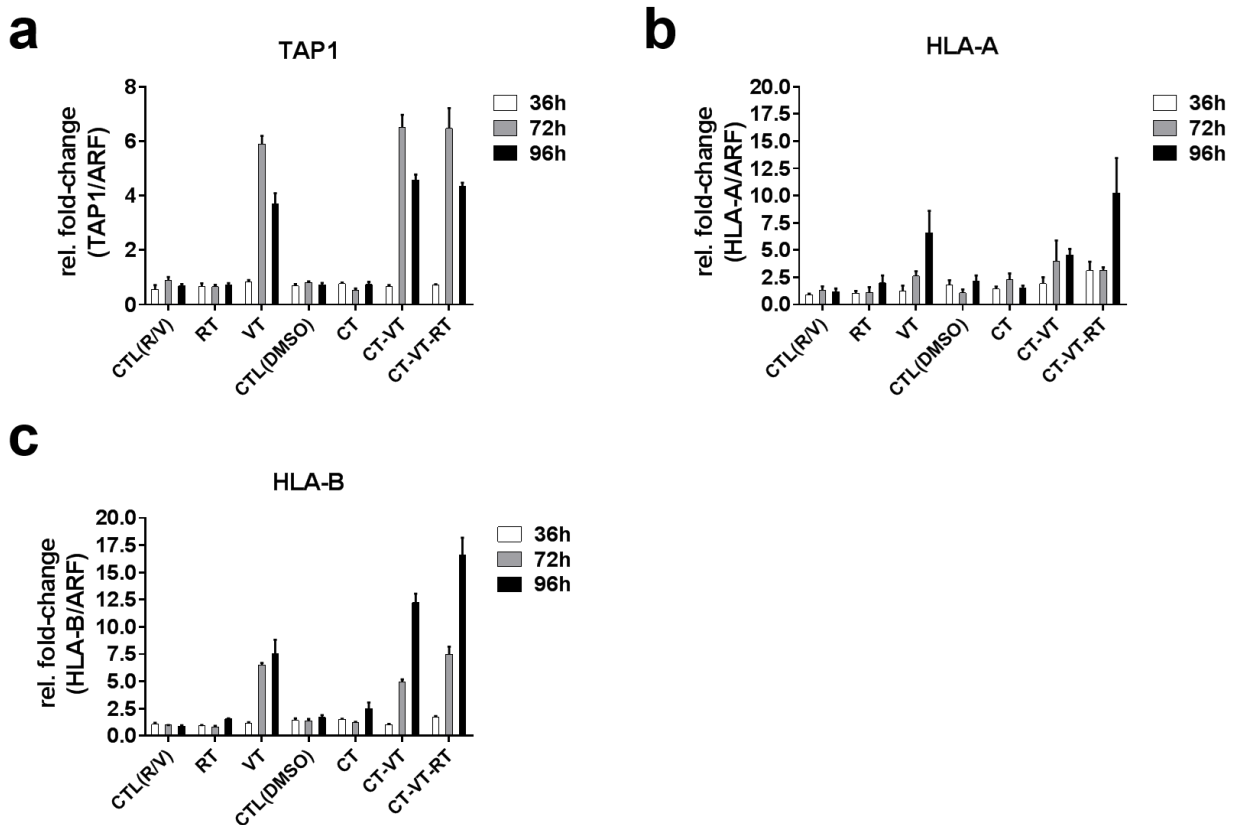
Oncolysis by MeV results in the release of cellular contents including virions, peptides and debris containing DAMPs and PAMPs potentially triggering induction of antiviral or anti-tumoral immune responses [30-32]. We therefore reasoned that CT-VT-RT might stimulate the presentation of tumoral antigens by glioma cells, coincided with upregulation of expression of HLA-A and HLA-B. Consequently, we performed an immunopeptidome analysis. We isolated HLA ligands with subsequent identification of peptides by mass spectrometry and data were processed against our RNA sequenced reads and MeV proteome. We observed that CT-VT and CT-VT-RT distinctively increased antigen presentation with 1430 and 1222 peptides isolated respectively (Figs. 34a and 34b). CT-VT in particular increased presentation of antigens (Fig. 35) when compared against SOC, RT (23%) and CT (13%) using semi-quantitative volcano plot analysis. All treatment regimens revealed presentation of tumor associated antigenic peptides of Ephrin type-A receptor 2 (EPHA2) and Tenascin (TNC), which have been studied for association with tumors including glioblastoma [90,91]. We isolated a tumor-associated peptide (LYTDRTEKL) processed from transforming growth factor-beta-induced (TGFBI), exclusively presented in CT-VT. The expression of TGFBI is associated with anti-adhesive metastatic properties in cancers including melanoma and prostate cancer [92,93] and was significantly overexpressed in glioblastoma compared to low grade gliomas based on our TCGA dataset interrogation (Fig. 36). Moreover, other TGFBI-derived peptides from glioblastoma sample have been previously discovered and shown to be immunogenic [94].

a

Treatments	MHC ligands	Peptides
CT	912	829
VT	935	852
CT-VT	1412	1401
RT	758	660
CT-VT-RT	890	843

b
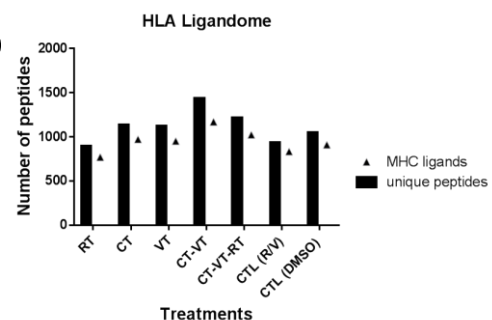
Figure 34. Table (a) and graph (b) enumerating MHC ligands and unique peptides isolated from LNZ308 cells post individual treatments using HLA ligandomics. The samples were normalized using similar cell seeding density prior to treatment and area adjustment during measurement.

Treatments
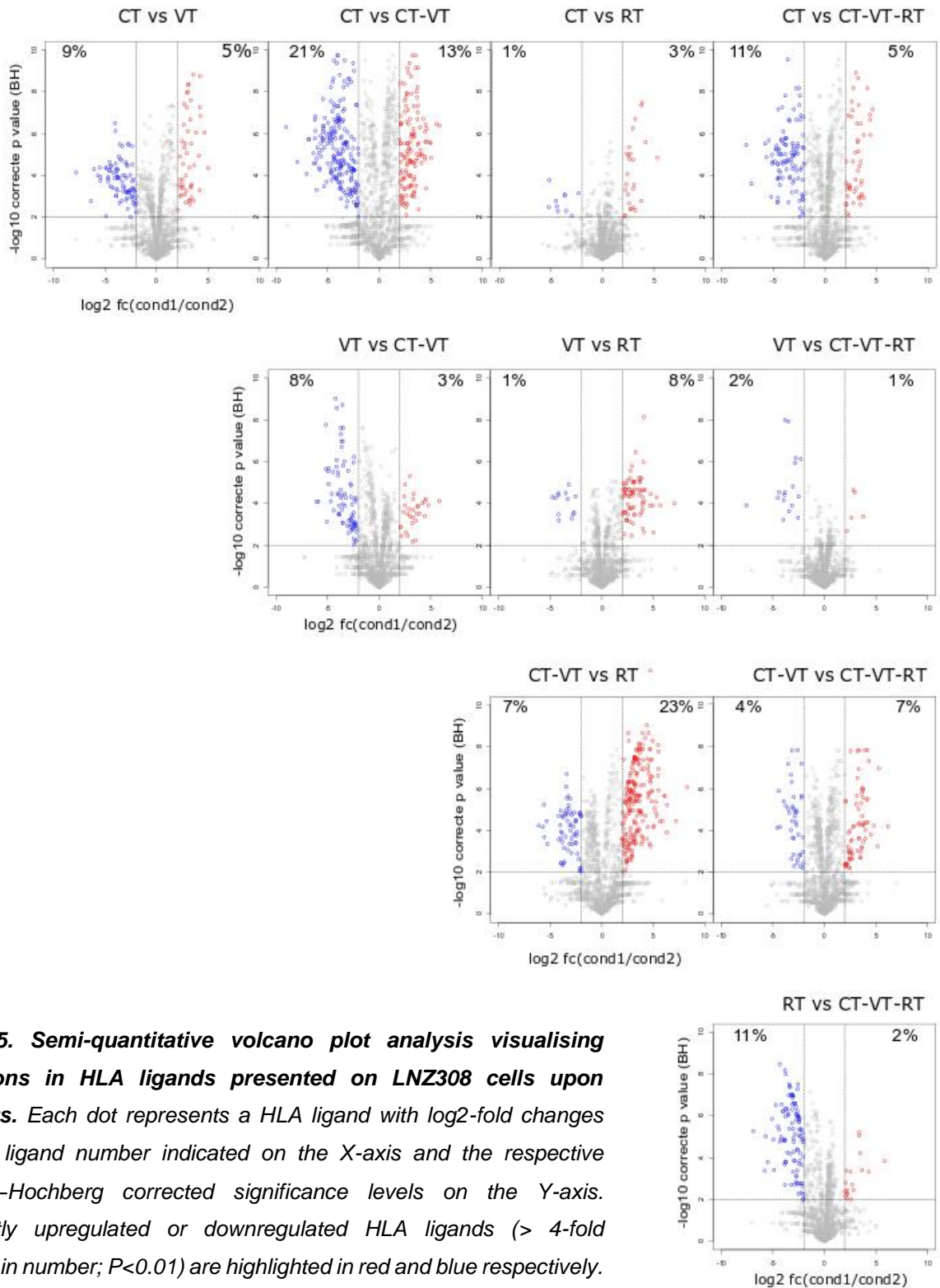
Figure 35. Semi-quantitative volcano plot analysis visualising modulations in HLA ligands presented on LNZ308 cells upon treatments. Each dot represents a HLA ligand with log2-fold changes with HLA ligand number indicated on the X-axis and the respective Benjamini–Hochberg corrected significance levels on the Y-axis. Significantly upregulated or downregulated HLA ligands (> 4-fold difference in number; P<0.01) are highlighted in red and blue respectively. The significantly modulated HLA ligand percentages are mentioned in the quadrats.

74
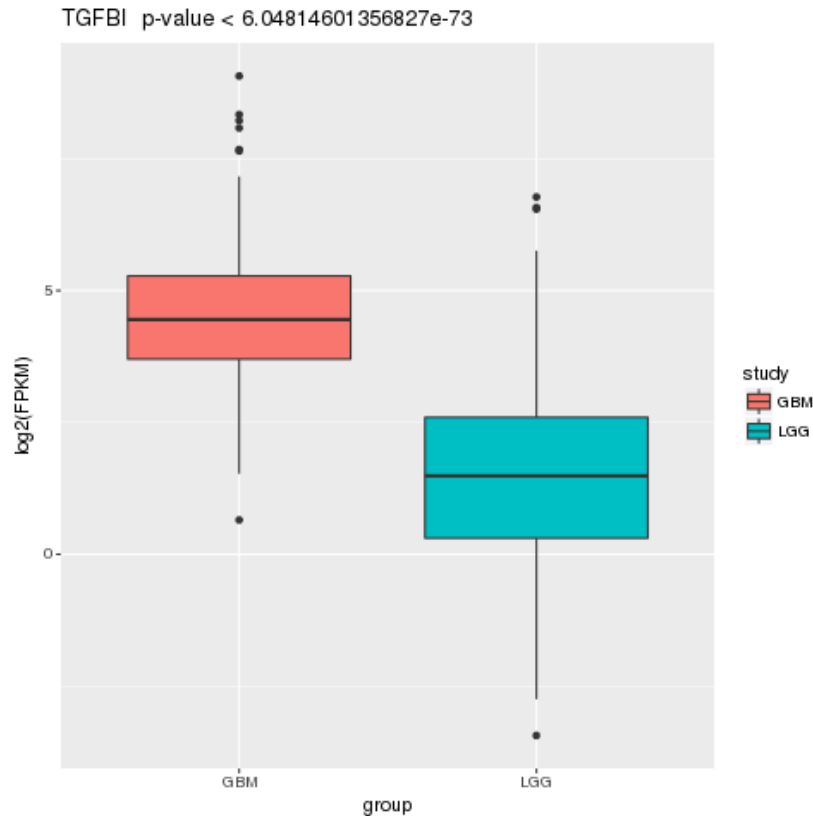
Figure 36. Expression profile of TGFBI analysed in TCGA dataset. TGFBI was significantly overexpressed in glioblastoma patients (GBM) in comparison to patients with low grade gliomas (LGG). The TGFBI expression represented in terms of log2 (FPKM). Abbreviations: TGFBI, TGF-β induced; GBM, glioblastoma; LGG, low grade glioma; FPKM, Fragments Per Kilobase of transcript per Million mapped reads. P-value : 6.04 X 10^{-73}.

3.23 MeV - L peptide is immunogenic and elicits CD8+ T cell responses

Interestingly, we identified the presentation of a novel viral peptide. We detected the HLA-A*24 specific MeV peptide, VYPRYSNFI processed from a highly conserved viral region, the MeV-L polymerase, in all virus-containing regimens. This peptide was particularly increased in the triple regimen CT-VT-RT (2.7 fold increase), compared with virotherapy alone (Fig. 37a). The identified MeV- L peptide (VYPRYSNFI) was synthetized and validated by matching fragmented spectra observed in VT containing regimens (Fig. 37b). To evaluate the immunogenicity and specificity of the HLA-A*24 specific peptide, we used a 12-day recall IFN-γ ELISPOT assay. Six PBMCs were obtained from six HLA-A*24 positive patients and stimulated with the viral peptide resulting in significant IFN-γ secretion in one of six samples with a mean spot count of 264.5 (Fig. 37c) further proving that the identified viral peptide is highly immunogenic. The IFN-γ ELISPOT assay reveals VYPRYSNFI functions as measles derived HLA-A*24 specific T-cell epitope capable of stimulating adaptive immune responses against viral hosts.
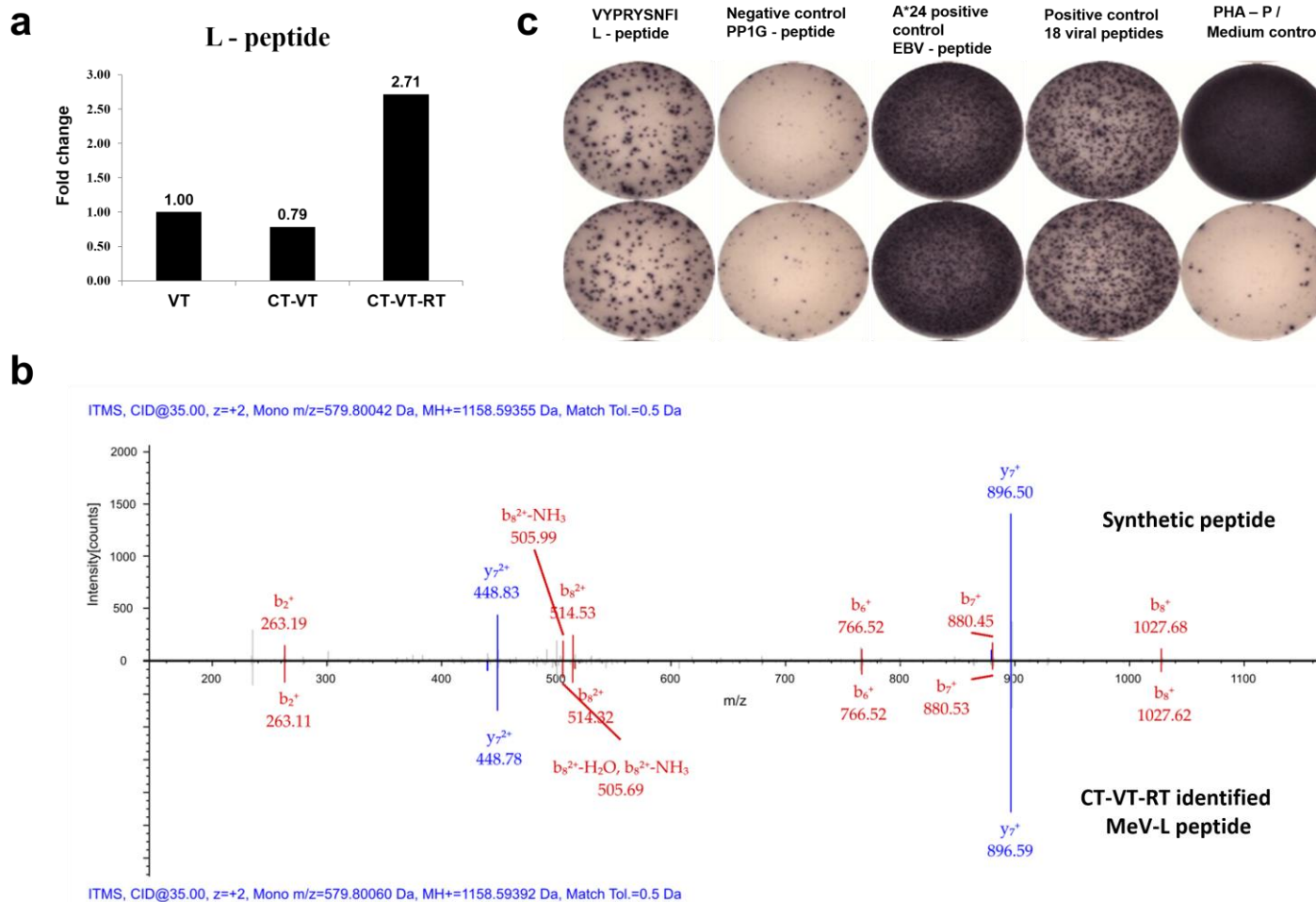
Figure 37. Antigenic presentation of immunogenic MeV-L peptide VYPRYSNFI. a, *CT-VT-RT leads to increased presentation of MeV L-peptide, VYPRYSNFI in HLA-A*24 with a 2.71 fold increase over VT alone.* **b,** *The synthetic viral peptide (upper axis) had identical fragmented spectra compared to MeV-L peptide isolated from CT-VT-RT treated cells (lower axis).* **c,** *VYPRYSNFI peptide stimulated healthy donor PBMCs secrete IFNγ indicating immunogenic potential of the peptide to elicit CD8+ T cell responses in ELISPOTs carried out with appropriate positive and negative controls.*

Discussion

Here, we aimed to identify and understand a chronological synergistic combination of oncolytic measles virus with standard of care radiotherapy and alkylating chemotherapy for treatment of glioma. The therapeutic safety profile of using Edmonston strain of measles as vaccine along with its ability to initiate an oncolytic cascade thereby triggering host immune responses offers promise for clinical translation.

Our study demonstrated the feasibility of using vaccine strain of measles in glioma tissue due to overexpression of viral receptor CD46 and frequent mutation of tumor suppressor genes as well as immunosuppressive nature of glioma presents as ideal hosts for viral proliferation. Measles virus initiates autophagy upon binding host CD46 with sustenance of autophagic flux through cell-cell fusing syncytial formation and thus inhibits host cell apoptotic induction through prevention of cytochrome-C release [68-70]. We reasoned that initiation of treatment with apoptosis inducing RT [71,72] would hinder measles viral proliferation thereby restricting synergy. Initial double regimens proved VT-RT to be synergistic (Fig. 11a) and we observed a clear antagonistic effect with RT-VT (Fig. 11c). Further, identical results observed by Liu *et al* (2007) validated our hypothesis that VT should always precede RT [73]. Upon incorporation of alkylating chemotherapy (CT), we designed three sequential therapy regimens and successfully identified a synergistic regimen, CT-VT-RT eliciting maximal therapeutic effect with low doses such as 2 Gy radiation in glioma cell lines LN229, LNZ308 and GS8 (Figs. 13, 14 and 16). Interestingly, we observed an enhanced virus associated cytotoxicity in our synergistic CT-VT-RT regimen (Fig. 13) over the VT-containing triple regimens (VT-RT-CT and VT-CT-RT), despite treatment with MeV 12 h earlier. Moreover, as relevant to recurrent glioblastomas we observed a CT-VT-RT driven synergy even when temozolomide (Figs. 19 and 20) was substituted with lomustine and such a CCNU dependent CT-VT-RT was able to rescue a progressive resistant effect in *in vitro* generated temozolomide resistant LN229 (Fig. 21) cells [12]. We investigated the molecular mechanism of synergy in CT-VT-RT by transcriptomics (RNASeq) and ligandomics (immunopeptidome) approaches and detected a clear signature of MeV-initiated proinflammatory responses (Figs. 22, 23 and 24).

The VT driven regimens including VT, CT-VT and CT-VT-RT efficiently triggered RLR signalling through increased transcription of RNA sensors, DDX58 (Fig. 25a) and MDA5 as early as 72 hours post treatment (hpt) leading to production of IFN-β. We detected an increase in IFN-β secretion upto 103 pg/ml per microgram of whole protein in CT-VT-RT (Fig. 25c) subsequently activating the canonical JAK-STAT pathway resulting in transcription of antiviral ISGs such as OAS's, MX's, ISG15 and IFIT's (Fig. 24b). The synergistic regimen stalled antiviral ISG transcription through delayed STAT signalling with 6-8 fold increase in STAT1 at

96 hpt (Fig. 26a), in comparison to CT-VT with a similar 6-8 fold transcription of STAT1 observed earlier at 72 hpt (Fig. 26a). Despite similar levels of ISGs observed in all VT regimens we identified an upregulation of TRAIL expression in CT-VT and CT-VT-RT at 72 hpt and 96 hpt through immunoblots (Fig. 27a, middle panel) with corresponding downstream effector caspase 3/7 activity (Fig. 27c). CT-VT at 72hpt exhibited highest caspase activity followed by CT-VT-RT indicating synergistic efficacy sequentially resulting in the successful initiation of programmed death cascades. In addition to the classical proinflammatory antiviral responses we observed increased transcription of genes such as SAMD9, BATF2, KAI1, SAMD9L and SEMA3D possessing anti-tumoral characteristics in our RNASeq (Fig. 23).

Sterile α motif domain-containing protein 9 (SAMD9) was upregulated in VT containing regimens with maximal expression in CT-VT-RT at 72 hpt and 96 hpt (Fig. 27a, upper panel). The deleterious mutation resulting in loss of SAMD9 causes normophosphatemic familial tumoral calcinosis while overexpression was shown to suppress non-small cell lung cancer *in vitro* [80,81]. Recent evidence of host SAMD9 expression in response to interferon stimulation and interaction with different viruses such as Sendai virus, vaccinia virus, myxomavirus, suggest a potential role as an innate antiviral host factor besides its anti-tumorigenic properties [79,95-97]. Therefore, the induction of SAMD9 as an antiviral factor during viral oncolysis would also be beneficial to initiate an anti-tumoral action thereby contributing to the synergistic mechanism. Contrary to reports suggesting downregulation of SAMD9 in response to interferon inhibition in Sendai virus-treated cells [95], we observed that SAMD9 expression remained unchanged by inhibition of IFN-β or STAT1-signalling (Fig. 30). Furthermore, we observed similar levels of effector caspase 3/7 activity in CT-VT-RT alone when compared to treatment with CT-VT-RT plus BX795 (Fig. 32b), a small molecule inhibitor of IFN-β production and downstream JAK/STAT pathway. The consistent caspase activity accompanied with loss of TRAIL expression in CT-VT-RT plus BX795 (Fig. 29h, upper panel) suggests that SAMD9 does not influence IFN-β dependent apoptosis. Thereby, we provide evidence of SAMD9 as an innate antiviral host factor, whose expression can be independent of STAT1 signalling. The SAMD9 mechanism of action in the context of MeV infection is yet to be determined and will be a matter of future research.

Despite, a transcriptional increase in BATF2 mRNA in MeV-containing regimens in our RNASeq (Fig. 23), no change in BATF2 protein expression was observed by immunoblotting (Fig. 27b, upper panel). Strikingly, inhibition of IFN-β – JAK-STAT signalling through BX795 and fludarabine respectively, lead to an increase in BATF2 protein levels corresponding to elevated IRF1 protein (Fig. 31) expression. Roy *et al* (2015) demonstrate co-immunoprecipitation of BATF2 with IRF1 verifying interaction in response to Mycobacterial

infection resulting in induction of inflammatory responses along with regulation of immune response [88]. The coherent increase in expression of BATF2 and IRF1 in response to inhibition of type 1 interferon signalling was verified by immunoblotting (Fig. 31) and their corresponding interaction detected via proximity ligation assay with an increase in red amplification signal post CT-VT-RT plus fludarabine (Fig. 32a). Moreover, we detected secretion of BATF2-IRF1 transcriptionally induced chemokine, CCL5 [88], in cells treated with CT-VT-RT in combination with fludarabine and/or BX795 (Fig. 32c) while IFN-β was not detectable (Figs. 29b and 29c). This is particularly relevant, as CCL5 and IFN-β are known to be secreted in response to viral infection via the IRF3 signalling pathway, which is specifically inhibited upon BX795 treatment in our experimental setting [98,99]. The absence of IRF1 during proinflammatory type-1 interferon signalling and subsequent interaction with BATF2 upon inhibition of IFN-β implicates mutual exclusivity. Moreover, the expression of T cell stimulant, CCL5 and the activity of effector caspase 3/7 suggests a role as an alternative antiviral host machinery. Similar to SAMD9, reports demonstrate anti-tumoral properties of BATF2 in hepatocellular carcinoma, squamous cell carcinoma and colon cancer through different mechanisms [82,100,101]. Furthermore, BATF2 was shown to inhibit epithelial to mesenchymal (EMT) transition through suppression of Wnt/β-catenin signalling in glioblastoma and lung adenocarcinoma suggesting potential use as a therapeutic target in combination with Bevacizumab [102,103].

We observed increased expression of metastasis suppressor gene, KAI1 in our VT-containing regimen (Figs. 23 and 38). KAI1 overexpressing clones of H1299 human non-small cell lung cancer cells decreased MMP9 enzyme activity by upregulation of TIMP1 resulting in decreased invasion and metastasis *in vitro* [104]. Interestingly, we observed a consistent significant increase in TIMP1 and KAI1 transcription particularly in our CT-VT-RT treated cells at 96 hpt (Fig. 38). Moreover, studies identified direct interaction of KAI1 with endothelial cell-surface protein, DARC leading to induction of senescence and inhibition of tumor cell proliferation by regulating expression of T-box transcription factor, TBX2 and cyclin-dependent kinase inhibitor 1 (CDKN1A) *in vivo* [105]. Immunohistochemical and real time-PCR analysis in glioma tissues revealed that downregulation of KAI1 and an increase in PDGFRβ was associated with progressive tumor growth suggesting their potential interaction affecting tumor cell invasiveness [106]. Thus, a CT-VT-RT induced increase in KAI1 expression would further aid in our synergistic mechanism, by inhibiting intrinsic tumor proliferative capacity and hence an interesting subject matter for future research.

Similarly, we noticed a significant increase in axonal guidance factor, semaphorin-3D (SEMA3D) in our VT-containing regimens (Fig. 23). SEMA3D was shown to exhibit tumor suppressive properties in colorectal cancer and glioblastoma [107,108]. Sabag *et al* (2012) showed that U87MG cells expressing SEMA3D prolonged survival of mice by more than two-folds and suggested, inhibition of tumor angiogenesis as a potential mechanism for its tumor suppressive nature [108]. Furthermore, we observed an increase in tumor suppressive SAMD9L transcripts upon MeV infection. Previous studies have shown that deletion or haploinsufficiency of SAMD9L resulted in myeloid transformations [109] and thus validating our hypothesis that, synergistic CT-VT-RT regimen triggers the induction of anti-tumoral response pathways.
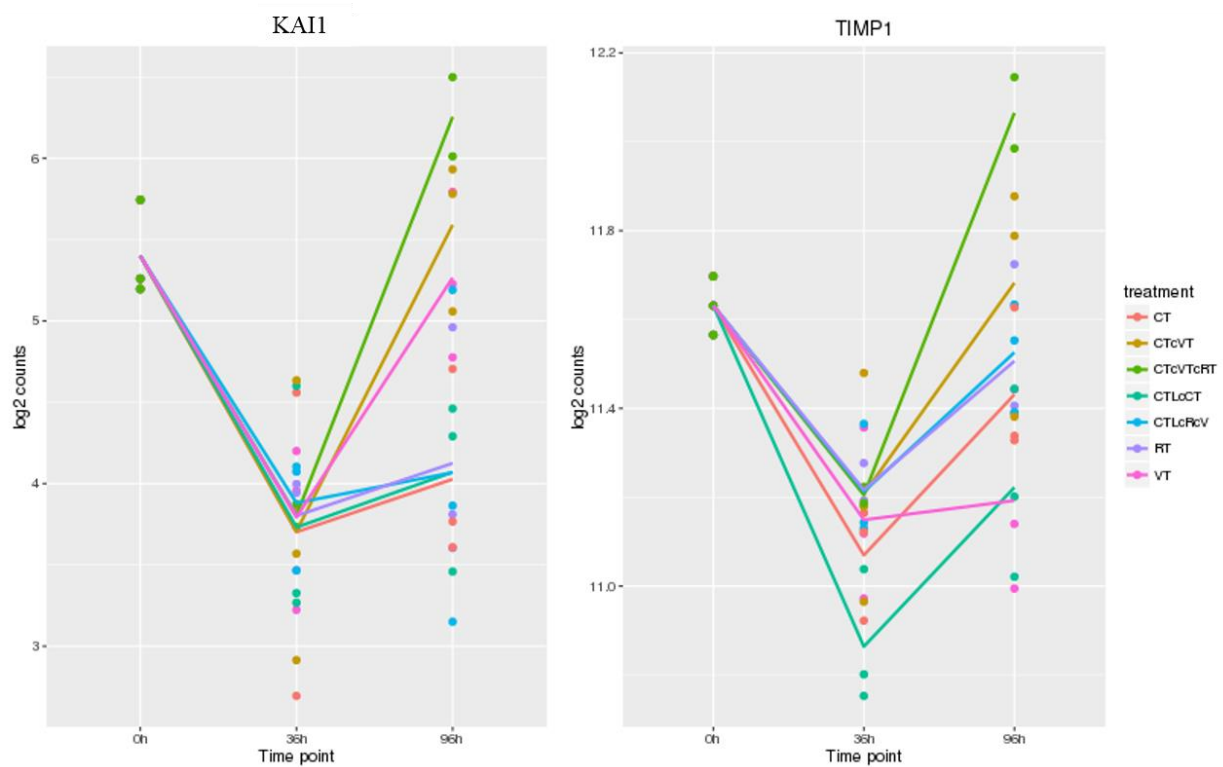
Figure 38. Coherent increase in KAI1 and TIMP1 transcripts in CT-VT-RT treated cells. *RNASeq revealed increased mRNA expression of KAI1 (left) and TIMP1 (right) in CT-VT-RT (green) treated LNZ308 cells at 96 hpt. The mRNA transcripts are expressed as log$_2$ counts (Y-axis) at different time points (X-axis).*

CT-VT-RT secreted chemokines involved in regulation of immune responses with 634 pg/ml of CXCL10 in comparison to 290 pg/ml in CT-VT and 263 pg/ml in VT (Fig. 28a). CXCL10 acts as chemoattractant for natural killer cells and activated T lymphocytes with anti-tumoral properties and was found to be synergistic when used in combination with TNF-α in murine glioblastoma [110,111]. The profound increase in immune chemokines were consistent with increased antigen processing machinery with elevated expression of TAP1 mRNA (Fig. 33a) in all VT-containing regimens. Furthermore, we observed a 10-fold increase in HLA-A (Fig.

33b) and 15-fold increase in HLA-B mRNA levels (Fig. 33c) in CT-VT-RT treated cells when compared to 5-fold increases in VT alone (Fig. 33b and 33c) suggesting increased antigen presentation. In concurrence with RNASeq, the upregulation of antigen presentation pathway correlated with increased antigenic peptides presented on HLA molecules with maximal presentation detected in CT-VT and CT-VT-RT with 1430 and 1222 peptides respectively (Figs. 34a and 34b), quantified through extrinsic ligandome enrichment. All VT-containing regimens presented the MeV polymerase (L) peptide (VYPRYSNFI) in HLA-A*24 while CT-VT alone presented a tumor associated antigenic peptide TGFBI (LYTDRTEKL). Based on our TCGA dataset interrogation, TGFBI was significantly overexpressed in glioblastoma compared to lower grade gliomas (Fig. 36) and other TGFBI-derived peptides from glioblastoma sample have been previously discovered and shown to be immunogenic [94]. Thus, the LYTDRTEKL peptide could be exploited to further enhance the efficacy of CT-VT-RT regimen by peptide vaccination using this sequence to augment a tumor-directed immune response.

However, our synergistic regimen, CT-VT-RT exhibited a 2.7 fold increase in presentation of this MeV-L peptide over virotherapy alone (Fig. 37a). The viral L peptide was shown to be immunogenic also in human patients (Fig. 37c) thereby suggesting that CT-VT-RT apart from triggering apoptosis increased presentation of immunogenic viral and tumor associated peptides along with upregulated chemokine expression potentially initiating antiviral as well as anti-tumoral immune responses. The observed increase in proinflammatory responses and immune regulatory networks in CT-VT-RT treated cells was accompanied with an increase in PD-1L transcription identified through RNASeq (Fig. 23) further consistent with evidence of synergy observed when combining oncolytic measles virus with immune checkpoint blockade inhibitors [31,34].

Studies show an upregulated expression of PD-L1 in IDH1/2 wildtype GBM and a strong association with the mesenchymal subgroup of tumors thereby, suggesting selection of patients that benefit from immunotherapeutic checkpoint antibodies in ongoing clinical trials [112]. Furthermore, decreased expression of PD-L1 was observed in recurrent GBM compared to de-novo GBM [113]. Combining proinflammatory virotherapeutic approaches would stimulate immune surveillance and hence, function synergistically with checkpoint inhibitors. Speranza *et al* (2018) combined chemo-virotherapeutic approach of non-replicating adenovirus encoding thymidine kinase along with anti-PD1 antibodies *in vitro* and *in vivo* [114]. The subsequent administration of prodrug, ganciclovir, which upon conversion by thymidine kinase functions as an in situ chemotherapeutic agent resulting in activation of proinflammatory type 1 interferon response with a consequent increase in PD-L1 expression [114]. Such smart combinations of proinflammatory chemo-virotherapeutic approach enhances immunogenic cell death

effectuated in combination with checkpoint blockade inhibitors due to upregulated PD-L1 expression, observed with increased percentage of long-term survivors when compared to either treatments alone in mice [114]. The failure in tumor growth upon rechallenge in such long-term survivors [114] implicate long lasting anti-tumoral memory T-cells and the synergy observed with such a combinatorial regimen.

Similarly, our CT-VT-RT regimen potency can be enhanced by combining with personalized vaccines containing immunogenic tumor associated and viral peptides along with checkpoint blockade antibodies against PD-1, CTLA-4, etc,. Glioma cells infected with the virus but not lysed as part of the oncolytic cascade would be targeted by the activated immune cells due to stimulation with MeV-L peptide. Moreover, certain tumor cells are considered resistant to MeV induced oncolysis due to upregulated expression of innate sensors or type-1 interferon production sustaining a distinctive antiviral state [115-117]. These cells nonetheless are permissive to viral infectivity and thus the combination of viral peptide vaccines along with checkpoint inhibitors would render them susceptible to host initiated immune response. Further knowledge that most patients undergo childhood vaccinations against MeV should allow for re-activation of memory T-cells upon challenge with viral peptide, designed from a highly conserved region of viral genome, RNA polymerase (L). Also, given the immunosuppressive nature of glioblastoma the strong co-stimulatory signal elicited by the viral peptide would aid in immune responses initiated by tumor peptides such as LYTDRTEKL (TGFBI). Thus, cells not infected by virus are susceptible through SOC radiotherapy and alkylating chemotherapy as part of the synergistic regimen along with anti-tumoral immune responses activated by tumor associated peptides and checkpoint blockade inhibitors while, MeV initiates an oncolytic cascade in neighbouring cells simultaneously.

The oncolytic approach of measles virus further exacerbated through cloning of cytotoxic genes in clinical use such as super cytosine deaminase (SCD) or human thyroidal sodium iodide symporter (NIS) and the latter also utilized for live imaging of viral dynamics through non-invasive radioiodine single-photon emission computed tomography (SPECT) — computed tomography (CT) [23,118]. Also, we assessed the feasibility of delivering measles virus through individualized patient-cell based therapy employing HPC's as our viral logistics partners. We showed successfully delivery of MeV to the glioma cells by the HPC's (Fig. 9) using co-culture assays and previous studies detail enhanced homing ability of HPC's due to intrinsic chemokine signalling events such as CXCL12-CXCR4, stem cell factor (SCF)-CD117, etc, [65-67]. The presence of stress factors including γ-irradiation and alkylating agents in CT-VT-RT and the consequently induced immune-stimulatory chemokine signalling events in our setting might further enhance the glioma tropism of these HPC's.

In conclusion, we have verified the synergistic combination of CT-VT-RT as a sequential regimen with proinflammatory characteristics capable of triggering apoptotic cascades in addition to host initiated antiviral, anti-tumoral immune response through increased presentation of immunogenic viral and tumor associated peptides. We hereby propose a novel synergistic approach for treatment of glioblastoma by combining CT-VT-RT with novel personalized vaccines consisting of tumor and viral peptides and probably with anti-PD1/anti-PD-L1 antibodies.

References

1.	Stupp, R.*, et al.* Effects of radiotherapy with concomitant and adjuvant temozolomide versus radiotherapy alone on survival in glioblastoma in a randomised phase III study: 5-year analysis of the EORTC-NCIC trial. *Lancet Oncol* **10**, 459-466 (2009).

2.	Gilbert, M.R.*, et al.* A randomized trial of bevacizumab for newly diagnosed glioblastoma. *N Engl J Med* **370**, 699-708 (2014).

3.	Gilbert, M.R.*, et al.* Dose-dense temozolomide for newly diagnosed glioblastoma: a randomized phase III clinical trial. *J Clin Oncol* **31**, 4085-4091 (2013).

4.	Chinot, O.L.*, et al.* Bevacizumab plus radiotherapy-temozolomide for newly diagnosed glioblastoma. *N Engl J Med* **370**, 709-722 (2014).

5.	James, C.D. & Olson, J.J. Molecular genetics and molecular biology advances in brain tumors. *Curr Opin Oncol* **8**, 188-195 (1996).

6.	Patil, C.G.*, et al.* Prognosis of patients with multifocal glioblastoma: a case-control study. *J Neurosurg* **117**, 705-711 (2012).

7.	Ishii, N.*, et al.* Cells with TP53 mutations in low grade astrocytic tumors evolve clonally to malignancy and are an unfavorable prognostic factor. *Oncogene* **18**, 5870-5878 (1999).

8.	Stummer, W.*, et al.* Fluorescence-guided surgery with 5-aminolevulinic acid for resection of malignant glioma: a randomised controlled multicentre phase III trial. *Lancet Oncol* **7**, 392-401 (2006).

9.	Stupp, R.*, et al.* Radiotherapy plus concomitant and adjuvant temozolomide for glioblastoma. *N Engl J Med* **352**, 987-996 (2005).

10.	Drablos, F.*, et al.* Alkylation damage in DNA and RNA--repair mechanisms and medical significance. *DNA Repair (Amst)* **3**, 1389-1407 (2004).

11.	Hegi, M.E.*, et al.* MGMT gene silencing and benefit from temozolomide in glioblastoma. *N Engl J Med* **352**, 997-1003 (2005).

12.	Wick, W.*, et al.* Phase III study of enzastaurin compared with lomustine in the treatment of recurrent intracranial glioblastoma. *J Clin Oncol* **28**, 1168-1174 (2010).

13.	Batchelor, T.T.*, et al.* Phase III Randomized Trial Comparing the Efficacy of Cediranib As Monotherapy, and in Combination With Lomustine, Versus Lomustine Alone in Patients With Recurrent Glioblastoma. *Journal of Clinical Oncology* **31**, 3212-3218 (2013).

14. Wick, W.*, et al.* Lomustine and Bevacizumab in Progressive Glioblastoma. *N Engl J Med* **377**, 1954-1963 (2017).

15. Taal, W.*, et al.* Single-agent bevacizumab or lomustine versus a combination of bevacizumab plus lomustine in patients with recurrent glioblastoma (BELOB trial): a randomised controlled phase 2 trial. *Lancet Oncol* **15**, 943-953 (2014).

16. Stupp, R.*, et al.* Effect of Tumor-Treating Fields Plus Maintenance Temozolomide vs Maintenance Temozolomide Alone on Survival in Patients With Glioblastoma: A Randomized Clinical Trial. *JAMA* **318**, 2306-2316 (2017).

17. Klatzmann, D.*, et al.* A phase I/II study of herpes simplex virus type 1 thymidine kinase "suicide" gene therapy for recurrent glioblastoma. Study Group on Gene Therapy for Glioblastoma. *Hum Gene Ther* **9**, 2595-2604 (1998).

18. Rainov, N.G.*, et al.* Temozolomide enhances herpes simplex virus thymidine kinase/ganciclovir therapy of malignant glioma. *Cancer Gene Ther* **8**, 662-668 (2001).

19. Chiocca, E.A.*, et al.* A phase I open-label, dose-escalation, multi-institutional trial of injection with an E1B-attenuated adenovirus, ONYX-015, into the peritumoral region of recurrent malignant gliomas, in the adjuvant setting. *Molecular Therapy* **10**, 958-966 (2004).

20. Rothmann, T., Hengstermann, A., Whitaker, N.J., Scheffner, M. & zur Hausen, H. Replication of ONYX-015, a potential anticancer adenovirus, is independent of p53 status in tumor cells. *Journal of Virology* **72**, 9470-9478 (1998).

21. O'Shea, C.C.*, et al.* Late viral RNA export, rather than p53 inactivation, determines ONYX-015 tumor selectivity. *Cancer Cell* **6**, 611-623 (2004).

22. Greig, S.L. Talimogene Laherparepvec: First Global Approval. *Drugs* **76**, 147-154 (2016).

23. Russell, S.J.*, et al.* Remission of disseminated cancer after systemic oncolytic virotherapy. *Mayo Clin Proc* **89**, 926-933 (2014).

24. Dispenzieri, A.*, et al.* Phase I trial of systemic administration of Edmonston strain of measles virus genetically engineered to express the sodium iodide symporter in patients with recurrent or refractory multiple myeloma. *Leukemia* **31**, 2791-2798 (2017).

25. Dingli, D.*, et al.* Image-guided radiovirotherapy for multiple myeloma using a recombinant measles virus expressing the thyroidal sodium iodide symporter. *Blood* **103**, 1641-1646 (2004).

26. Yurttas, C., Berchtold, S., Malek, N., Bitzer, M. & Lauer, U.M. "PULSED" versus "CONTINUOUS" application of the prodrug 5-FC for enhancing oncolytic effectiveness of a measles vaccine virus armed with a suicide gene. *Hum Gene Ther Clin Dev* (2014).

27. Fecci, P.E.*, et al.* Increased regulatory T-cell fraction amidst a diminished CD4 compartment explains cellular immune defects in patients with malignant glioma. *Cancer Res* **66**, 3294-3302 (2006).

28. Bloch, O.*, et al.* Gliomas Promote Immunosuppression through Induction of B7-H1 Expression in Tumor-Associated Macrophages. *Clinical Cancer Research* **19**, 3165-3175 (2013).

29. Okada, H.*, et al.* Induction of CD8+ T-cell responses against novel glioma-associated antigen peptides and clinical activity by vaccinations with {alpha}-type 1 polarized dendritic cells and polyinosinic-polycytidylic acid stabilized by lysine and carboxymethylcellulose in patients with recurrent malignant glioma. *J Clin Oncol* **29**, 330-336 (2011).

30. Donnelly, O.G.*, et al.* Measles virus causes immunogenic cell death in human melanoma. *Gene Ther* **20**, 7-15 (2013).

31. Hardcastle, J.*, et al.* Immunovirotherapy with measles virus strains in combination with anti-PD-1 antibody blockade enhances antitumor activity in glioblastoma treatment. *Neuro Oncol* **19**, 493-502 (2017).

32. Gauvrit, A.*, et al.* Measles virus induces oncolysis of mesothelioma cells and allows dendritic cells to cross-prime tumor-specific CD8 response. *Cancer Res* **68**, 4882-4892 (2008).

33. Wheeler, L.A.*, et al.* Phase II multicenter study of gene-mediated cytotoxic immunotherapy as adjuvant to surgical resection for newly diagnosed malignant glioma. *Neuro Oncol* **18**, 1137-1145 (2016).

34. Engeland, C.E.*, et al.* CTLA-4 and PD-L1 checkpoint blockade enhances oncolytic measles virus therapy. *Mol Ther* **22**, 1949-1959 (2014).

35. Ribas, A.*, et al.* Oncolytic Virotherapy Promotes Intratumoral T Cell Infiltration and Improves Anti-PD-1 Immunotherapy. *Cell* **170**, 1109-1119 e1110 (2017).

36. Chesney, J.*, et al.* Randomized, Open-Label Phase II Study Evaluating the Efficacy and Safety of Talimogene Laherparepvec in Combination With Ipilimumab Versus Ipilimumab Alone in Patients With Advanced, Unresectable Melanoma. *J Clin Oncol*, JCO2017737379 (2017).

37. Rosewell Shaw, A.*, et al.* Adenovirotherapy Delivering Cytokine and Checkpoint Inhibitor Augments CAR T Cells against Metastatic Head and Neck Cancer. *Mol Ther* **25**, 2440-2451 (2017).

38. Cockle, J.V.*, et al.* Combination viroimmunotherapy with checkpoint inhibition to treat glioma, based on location-specific tumor profiling. *Neuro Oncol* **18**, 518-527 (2016).

39. Radecke, F.*, et al.* Rescue of measles viruses from cloned DNA. *EMBO J* **14**, 5773-5784 (1995).

40. Gunther, H.S.*, et al.* Glioblastoma-derived stem cell-enriched cultures form distinct subgroups according to molecular and phenotypic criteria. *Oncogene* **27**, 2897-2909 (2008).

41. Barde, I., Salmon, P. & Trono, D. Production and titration of lentiviral vectors. *Curr Protoc Neurosci* **Chapter 4**, Unit 4 21 (2010).

42. Kärber, G. Beitrag zur kollektiven Behandlung pharmakologischer Reihenversuche. *Naunyn-Schmiedebergs Archiv für experimentelle Pathologie und Pharmakologie* **162**, 480-483 (1931).

43. Perazzoli, G.*, et al.* Temozolomide Resistance in Glioblastoma Cell Lines: Implication of MGMT, MMR, P-Glycoprotein and CD133 Expression. *PLoS One* **10**, e0140131 (2015).

44. Chatrchyan, S.*, et al.* Search for neutral minimal supersymmetric standard model Higgs bosons decaying to tau pairs in pp collisions at radicals=7 TeV. *Phys Rev Lett* **106**, 231801 (2011).

45. Martin, M. Cutadapt removes adapter sequences from high-throughput sequencing reads. *2011* **17**(2011).

46. Kim, D.*, et al.* TopHat2: accurate alignment of transcriptomes in the presence of insertions, deletions and gene fusions. *Genome Biol* **14**, R36 (2013).

47. Anders, S., Pyl, P.T. & Huber, W. HTSeq--a Python framework to work with high-throughput sequencing data. *Bioinformatics* **31**, 166-169 (2015).

48. Love, M.I., Huber, W. & Anders, S. Moderated estimation of fold change and dispersion for RNA-seq data with DESeq2. *Genome Biol* **15**, 550 (2014).

49. Clark, K., Plater, L., Peggie, M. & Cohen, P. Use of the Pharmacological Inhibitor BX795 to Study the Regulation and Physiological Roles of TBK1 and IκB Kinase ε: A DISTINCT UPSTREAM KINASE MEDIATES SER-172 PHOSPHORYLATION AND ACTIVATION. *The Journal of Biological Chemistry* **284**, 14136-14146 (2009).

50.   Hanafi, L.A*., et al.* Fludarabine downregulates indoleamine 2,3-dioxygenase in tumors via a proteasome-mediated degradation mechanism. *PLoS One* **9**, e99211 (2014).

51.   Kowalewski, D.J. & Stevanovic, S. Biochemical large-scale identification of MHC class I ligands. *Methods Mol Biol* **960**, 145-157 (2013).

52.   Falk, K., Rotzschke, O., Stevanovic, S., Jung, G. & Rammensee, H.G. Allele-specific motifs revealed by sequencing of self-peptides eluted from MHC molecules. *Nature* **351**, 290-296 (1991).

53.   Eng, J.K., McCormack, A.L. & Yates, J.R. An approach to correlate tandem mass spectral data of peptides with amino acid sequences in a protein database. *J Am Soc Mass Spectrom* **5**, 976-989 (1994).

54.   Kall, L., Canterbury, J.D., Weston, J., Noble, W.S. & MacCoss, M.J. Semi-supervised learning for peptide identification from shotgun proteomics datasets. *Nat Methods* **4**, 923-925 (2007).

55.   Nielsen, M. & Andreatta, M. NetMHCpan-3.0; improved prediction of binding to MHC class I molecules integrating information from multiple receptor and peptide length datasets. *Genome Med* **8**, 33 (2016).

56.   Zhang, J.G*., et al.* Antigenic profiling of glioma cells to generate allogeneic vaccines or dendritic cell-based therapeutics. *Clin Cancer Res* **13**, 566-575 (2007).

57.   Peper, J.K*., et al.* HLA ligandomics identifies histone deacetylase 1 as target for ovarian cancer immunotherapy. *Oncoimmunology* **5**, e1065369 (2016).

58.   Dorig, R.E., Marcil, A. & Richardson, C.D. CD46, a primate-specific receptor for measles virus. *Trends Microbiol* **2**, 312-318 (1994).

59.   Ulasov, I.V., Tyler, M.A., Zheng, S., Han, Y. & Lesniak, M.S. CD46 represents a target for adenoviral gene therapy of malignant glioma. *Hum Gene Ther* **17**, 556-564 (2006).

60.   Rushmere, N.K*., et al.* Analysis of the level of mRNA expression of the membrane regulators of complement, CD59, CD55 and CD46, in breast cancer. *Int J Cancer* **108**, 930-936 (2004).

61.   Derycke, M.S*., et al.* Nectin 4 overexpression in ovarian cancer tissues and serum: potential role as a serum biomarker. *Am J Clin Pathol* **134**, 835-845 (2010).

62.   Fabre-Lafay, S*., et al.* Nectin-4 is a new histological and serological tumor associated marker for breast cancer. *BMC Cancer* **7**, 73 (2007).

63.   Geekiyanage, H. & Galanis, E. MiR-31 and miR-128 regulates poliovirus receptor-related 4 mediated measles virus infectivity in tumors. *Mol Oncol* **10**, 1387-1403 (2016).

64. Vignard, J., Mirey, G. & Salles, B. Ionizing-radiation induced DNA double-strand breaks: a direct and indirect lighting up. *Radiother Oncol* **108**, 362-369 (2013).

65. Tabatabai, G., Frank, B., Mohle, R., Weller, M. & Wick, W. Irradiation and hypoxia promote homing of haematopoietic progenitor cells towards gliomas by TGF-beta-dependent HIF-1alpha-mediated induction of CXCL12. *Brain* **129**, 2426-2435 (2006).

66. Tabatabai, G*., et al.* VEGF-dependent induction of CD62E on endothelial cells mediates glioma tropism of adult haematopoietic progenitor cells. *Brain* **131**, 2579-2595 (2008).

67. Tabatabai, G*., et al.* Glioma tropism of lentivirally transduced hematopoietic progenitor cells. *Int J Oncol* **36**, 1409-1417 (2010).

68. Xia, M*., et al.* Mitophagy switches cell death from apoptosis to necrosis in NSCLC cells treated with oncolytic measles virus. *Oncotarget* **5**, 3907-3918 (2014).

69. Joubert, P.E*., et al.* Autophagy induction by the pathogen receptor CD46. *Cell Host Microbe* **6**, 354-366 (2009).

70. Richetta, C*., et al.* Sustained autophagy contributes to measles virus infectivity. *PLoS Pathog* **9**, e1003599 (2013).

71. Seki, H*., et al.* Ionizing-Radiation Induces Apoptotic Cell-Death in Human Tcr-Gamma/Delta(+) T-Cells and Natural-Killer-Cells without Detectable P53 Protein. *Eur J Immunol* **24**, 2914-2917 (1994).

72. Fulda, S*., et al.* Activation of the CD95 (APO-1/Fas) pathway in drug- and gamma-irradiation-induced apoptosis of brain tumor cells. *Cell Death and Differentiation* **5**, 884-893 (1998).

73. Liu, C*., et al.* Combination of measles virus virotherapy and radiation therapy has synergistic activity in the treatment of glioblastoma multiforme. *Clin Cancer Res* **13**, 7155-7165 (2007).

74. Chou, T.C. Drug combination studies and their synergy quantification using the Chou-Talalay method.

75. Hermisson, M*., et al.* O6-methylguanine DNA methyltransferase and p53 status predict temozolomide sensitivity in human malignant glioma cells. *J Neurochem* **96**, 766-776 (2006).

76. Van Meir, E.G*., et al.* Analysis of the p53 gene and its expression in human glioblastoma cells. *Cancer Res* **54**, 649-652 (1994).

77.   Chawla-Sarkar, M.*, et al.* Apoptosis and interferons: Role of interferon-stimulated genes as mediators of apoptosis. *Apoptosis* **8**, 237-249 (2003).

78.   Nounamo, B.*, et al.* An interaction domain in human SAMD9 is essential for myxoma virus host-range determinant M062 antagonism of host anti-viral function. *Virology* **503**, 94-102 (2017).

79.   Liu, J. & McFadden, G. SAMD9 is an innate antiviral host factor with stress response properties that can be antagonized by poxviruses. *J Virol* **89**, 1925-1931 (2015).

80.   Topaz, O.*, et al.* A deleterious mutation in SAMD9 causes normophosphatemic familial tumoral calcinosis. *Am J Hum Genet* **79**, 759-764 (2006).

81.   Ma, Q., Yu, T., Ren, Y.Y., Gong, T. & Zhong, D.S. Overexpression of SAMD9 suppresses tumorigenesis and progression during non small cell lung cancer. *Biochem Biophys Res Commun* **454**, 157-161 (2014).

82.   Dai, L.*, et al.* SARI inhibits angiogenesis and tumour growth of human colon cancer through directly targeting ceruloplasmin. *Nat Commun* **7**, 11996 (2016).

83.   Andrade, A.F.*, et al.* The DNA methyltransferase inhibitor zebularine exerts antitumor effects and reveals BATF2 as a poor prognostic marker for childhood medulloblastoma. *Invest New Drugs* **35**, 26-36 (2017).

84.   Berghall, H.*, et al.* The interferon-inducible RNA helicase, mda-5, is involved in measles virus-induced expression of antiviral cytokines. *Microbes Infect* **8**, 2138-2144 (2006).

85.   Pertl, U.*, et al.* IFN-gamma-inducible protein-10 is essential for the generation of a protective tumor-specific CD8 T cell response induced by single-chain IL-12 gene therapy. *J Immunol* **166**, 6944-6951 (2001).

86.   Schols, D., Proost, P., Van Damme, J. & De Clercq, E. RANTES and MCP-3 inhibit the replication of T-cell-tropic human immunodeficiency virus type 1 strains (SF-2, MN, and HE). *J Virol* **71**, 7300-7304 (1997).

87.   Coffey, M.J., Woffendin, C., Phare, S.M., Strieter, R.M. & Markovitz, D.M. RANTES inhibits HIV-1 replication in human peripheral blood monocytes and alveolar macrophages. *Am J Physiol* **272**, L1025-1029 (1997).

88.   Roy, S.*, et al.* Batf2/Irf1 induces inflammatory responses in classically activated macrophages, lipopolysaccharides, and mycobacterial infection. *J Immunol* **194**, 6035-6044 (2015).

89.   Leeuwenberg, J.F., van Damme, J., Jeunhomme, G.M. & Buurman, W.A. Interferon beta 1, an intermediate in the tumor necrosis factor alpha-induced increased MHC

class I expression and an autocrine regulator of the constitutive MHC class I expression. *J Exp Med* **166**, 1180-1185 (1987).

90.	Neidert, M.C.*, et al.* Natural HLA class I ligands from glioblastoma: extending the options for immunotherapy. *J Neurooncol* **111**, 285-294 (2013).

91.	Hatano, M.*, et al.* EphA2 as a glioma-associated antigen: A novel target for glioma vaccines. *Neoplasia* **7**, 717-722 (2005).

92.	Nummela, P.*, et al.* Transforming growth factor beta-induced (TGFBI) is an anti-adhesive protein regulating the invasive growth of melanoma cells. *Am J Pathol* **180**, 1663-1674 (2012).

93.	Chen, W.Y.*, et al.* Loss of SPDEF and gain of TGFBI activity after androgen deprivation therapy promote EMT and bone metastasis of prostate cancer. *Sci Signal* **10**(2017).

94.	Singh, H.*, et al.* Immunogenic epitopes for immunotherapy. (Google Patents, 2016).

95.	Tanaka, M., Shimbo, T., Kikuchi, Y., Matsuda, M. & Kaneda, Y. Sterile alpha motif containing domain 9 is involved in death signaling of malignant glioma treated with inactivated Sendai virus particle (HVJ-E) or type I interferon. *Int J Cancer* **126**, 1982-1991 (2010).

96.	Liu, J., Wennier, S., Zhang, L. & McFadden, G. M062 is a host range factor essential for myxoma virus pathogenesis and functions as an antagonist of host SAMD9 in human cells. *J Virol* **85**, 3270-3282 (2011).

97.	Sivan, G., Ormanoglu, P., Buehler, E.C., Martin, S.E. & Moss, B. Identification of Restriction Factors by Human Genome-Wide RNA Interference Screening of Viral Host Range Mutants Exemplified by Discovery of SAMD9 and WDR6 as Inhibitors of the Vaccinia Virus K1L-C7L- Mutant. *MBio* **6**, e01122 (2015).

98.	Fitzgerald, K.A.*, et al.* IKKepsilon and TBK1 are essential components of the IRF3 signaling pathway. *Nat Immunol* **4**, 491-496 (2003).

99.	Schroder, M., Baran, M. & Bowie, A.G. Viral targeting of DEAD box protein 3 reveals its role in TBK1/IKKepsilon-mediated IRF activation. *EMBO J* **27**, 2147-2157 (2008).

100.	Ma, H.*, et al.* Decreased expression of BATF2 is associated with a poor prognosis in hepatocellular carcinoma. *Int J Cancer* **128**, 771-777 (2011).

101.	Wen, H.*, et al.* Decreased expression of BATF2 is significantly associated with poor prognosis in oral tongue squamous cell carcinoma. *Oncol Rep* **31**, 169-174 (2014).

102.	Huang, W., Zhang, C., Cui, M., Niu, J. & Ding, W. Inhibition of Bevacizumab-induced Epithelial-Mesenchymal Transition by BATF2 Overexpression Involves the

Suppression of Wnt/beta-Catenin Signaling in Glioblastoma Cells. *Anticancer Res* **37**, 4285-4294 (2017).

103. Wang, C.*, et al.* The function of SARI in modulating epithelial-mesenchymal transition and lung adenocarcinoma metastasis. *PLoS One* **7**, e38046 (2012).

104. Jee, B.K.*, et al.* KAI1/CD82 suppresses tumor invasion by MMP9 inactivation via TIMP1 up-regulation in the H1299 human lung carcinoma cell line. *Biochem Biophys Res Commun* **342**, 655-661 (2006).

105. Bandyopadhyay, S.*, et al.* Interaction of KAI1 on tumor cells with DARC on vascular endothelium leads to metastasis suppression. *Nat Med* **12**, 933-938 (2006).

106. Paradowski, M., Bilinska, M. & Bar, J. Characteristics of the expression of KAI1/CD82 and PDGFR beta and their impact on glioma progression. *Folia Neuropathol* **54**, 241-248 (2016).

107. Wang, Z.*, et al.* Decreased expression of semaphorin 3D is associated with genesis and development in colorectal cancer. *World J Surg Oncol* **15**(2017).

108. Sabag, A.D.*, et al.* Semaphorin-3D and Semaphorin-3E Inhibit the Development of Tumors from Glioblastoma Cells Implanted in the Cortex of the Brain. *Plos One* **7**(2012).

109. Nagamachi, A.*, et al.* Haploinsufficiency of SAMD9L, an Endosome Fusion Facilitator, Causes Myeloid Malignancies in Mice Mimicking Human Diseases with Monosomy 7. *Cancer Cell* **24**, 305-317 (2013).

110. Taub, D.D.*, et al.* Recombinant human interferon-inducible protein 10 is a chemoattractant for human monocytes and T lymphocytes and promotes T cell adhesion to endothelial cells. *J Exp Med* **177**, 1809-1814 (1993).

111. Enderlin, M.*, et al.* TNF-alpha and the IFN-gamma-inducible protein 10 (IP-10/CXCL-10) delivered by parvoviral vectors act in synergy to induce antitumor effects in mouse glioblastoma. *Cancer Gene Ther* **16**, 149-160 (2009).

112. Heiland, D.H.*, et al.* Comprehensive analysis of PD-L1 expression in glioblastoma multiforme. *Oncotarget* **8**, 42214-42225 (2017).

113. Heynckes, S.*, et al.* Expression differences of programmed death ligand 1 in de-novo and recurrent glioblastoma multiforme. *Oncotarget* **8**, 74170-74177 (2017).

114. Speranza, M.C.*, et al.* Preclinical investigation of combined gene-mediated cytotoxic immunotherapy and immune checkpoint blockade in glioblastoma. *Neuro Oncol* **20**, 225-235 (2018).

115. Berchtold, S*., et al.* Innate Immune Defense Defines Susceptibility of Sarcoma Cells to Measles Vaccine Virus-Based Oncolysis. *Journal of Virology* **87**, 3484-3501 (2013).

116. Parrula, M.C.M*., et al.* Success of measles virotherapy in ATL depends on type I interferon secretion and responsiveness. *Virus Res* **189**, 206-213 (2014).

117. Allagui, F*., et al.* Modulation of the Type I Interferon Response Defines the Sensitivity of Human Melanoma Cells to Oncolytic Measles Virus. *Curr Gene Ther* **16**, 419-428 (2016).

118. Lange, S*., et al.* A novel armed oncolytic measles vaccine virus for the treatment of cholangiocarcinoma. *Hum Gene Ther* **24**, 554-564 (2013).